SLAC–R–931

PROPERTIES OF TRAPPED ELECTRON BUNCHES IN A PLASMA WAKEFIELD ACCELERATOR

A DISSERTATION
SUBMITTED TO THE DEPARTMENT OF PHYSICS
AND THE COMMITTEE ON GRADUATE STUDIES
OF STANFORD UNIVERSITY
IN PARTIAL FULFILLMENT OF THE REQUIREMENTS
FOR THE DEGREE OF
DOCTOR OF PHILOSOPHY

Neil Allen Kirby

September 2009

Work supported in part by US Department of Energy contract DE–AC02–76SF00515

I certify that I have read this dissertation and that, in my opinion, it is fully adequate in scope and quality as a dissertation for the degree of Doctor of Philosophy.

(Alexander Chao) Principal Adviser

I certify that I have read this dissertation and that, in my opinion, it is fully adequate in scope and quality as a dissertation for the degree of Doctor of Philosophy.

(Mark Hogan)

I certify that I have read this dissertation and that, in my opinion, it is fully adequate in scope and quality as a dissertation for the degree of Doctor of Philosophy.

(Stanley Wojcicki)

Approved for the University Committee on Graduate Studies.

To my wife Jasmine

Abstract

Plasma-based accelerators use the propagation of a drive bunch through plasma to create large electric fields. Recent plasma wakefield accelerator (PWFA) experiments, carried out at the Stanford Linear Accelerator Center (SLAC), successfully doubled the energy for some of the 42 GeV drive bunch electrons in less than a meter; this feat would have required 3 km in the SLAC linac. This dissertation covers one phenomenon associated with the PWFA, electron trapping. Recently it was shown that PWFAs, operated in the nonlinear bubble regime, can trap electrons that are released by ionization inside the plasma wake and accelerate them to high energies. These trapped electrons occupy and can degrade the accelerating portion of the plasma wake, so it is important to understand their origins and how to remove them. Here, the onset of electron trapping is connected to the drive bunch properties.

Additionally, the trapped electron bunches are observed with normalized transverse emittance divided by peak current, $\epsilon_{N,x}/I_t$, below the level of 0.2 μm/kA. A theoretical model of the trapped electron emittance, developed here, indicates that the emittance scales inversely with the square root of the plasma density in the nonlinear "bubble" regime of the PWFA. This model and simulations indicate that the observed values of $\epsilon_{N,x}/I_t$ result from multi-GeV trapped electron bunches with emittances of a few μm and multi-kA peak currents. These properties make the trapped electrons a possible particle source for next generation light sources.

This dissertation is organized as follows. The first chapter is an overview of the PWFA, which includes a review of the accelerating and focusing fields and a survey of the remaining issues for a plasma-based particle collider. Then, the second chapter examines the physics of electron trapping in the PWFA. The third chapter uses theory and simulations to analyze the properties of the trapped electron bunches. Chapters

four and five present the experimental diagnostics and measurements for the trapped electrons. Next, the sixth chapter introduces suggestions for future trapped electron experiments. Then, Chapter seven contains the conclusions. In addition, there is an appendix chapter that covers a topic which is extraneous to electron trapping, but relevant to the PWFA. This chapter explores the feasibility of one idea for the production of a hollow channel plasma, which if produced could solve some of the remaining issues for a plasma-based collider.

Acknowledgement

My family has always encouraged and nurtured my scientific curiosity, which was essential to my development as a scientist. They have been with me through all the ups and downs of graduate school and given me unwavering moral support. This work would not be possible without them. I would like to thank my parents Gene and Sharon, my grandparents John and Elaine, my siblings Dustin and Laura, and my wife Jasmine.

Taking part in the plasma wakefield accelerator experiment at SLAC has been an exciting and rewarding experience. For this I would like to thank my collaborators on the experiment: Melissa Berry, Ian Blumenfeld, Chris Clayton, Franz-Josef Decker, Mark Hogan, Chengkun Huang, Rasmus Ischebeck, Rick Iverson, Chan Joshi, Tom Katsouleas, Wei Lu, Ken Marsh, Warren Mori, Patric Muggli, Erdem Oz, Robert Siemann, Dieter Walz, and Miaomiao Zhou. I would like to also thank Samuel Martins, who personally ran many of the crucial simulations in this dissertation, and Frank Tsung for his development of the simulation codes.

I have also been helped extensively by people outside of my scientific collaboration. For helping me navigate the administrative obstacles at Stanford and SLAC, I would like to thank Maria Frank, Stephanie Santo, and Joan Valine.

The completion of this dissertation has been a valuable experience. For help on this I would like to thank the members of my dissertation reading committee: Alexander Chao, Mark Hogan, and Stanley Wojcicki. Also, I would like to thank the additional examiners on my oral defense committee: David Reis and Sami Tantawi.

Dieter Walz is unmatched in his ability to get things done at SLAC. I would like to thank him for his help in designing and building my experimental diagnostics. Also, he is a valuable resource for scientific writing advice. I have learned much from his

input.

I would like to thank Ian Blumenfeld for our discussions. One of the best things that Bob did was to put us in the same office. It has been wonderful to be in the same room with someone who is always ready to talk physics. Our conversations have been the highlights of my graduate school experience and have inspired me in my research.

Although Mark Hogan was never officially my advisor, he has supported like one through my graduate career. For this I am grateful. Also, he has a remarkable experimental intuition, which has been extremely helpful for data analysis. Beyond this, I would like to thank him for his humor, which has helped me through some of my more challenging moments.

Robert Siemann was a wonderful advisor. He was always willing to drop whatever he was doing to discuss physics and had an amazing knack for guidance. Bob knew how to let me struggle with a problem enough to learn from it, but would step in at the right moment to keep my forward progress. I have developed as a physicist from his guidance and have been influenced greatly by his love of physics.

Even before Alexander Chao became my dissertation advisor, I would frequently go to him for theoretical physics advice. He has an amazing intuition for physics. Now that he is my advisor, his valuable advice has extended well beyond just theory. Alex has always welcomed me at his door and has been very gracious with his time. He has motivated and supported me through the writing of this dissertation. Bob's passing was a difficult situation, but I could not have asked for a better person than Alex to guide me through it. Thank you.

Contents

List of Tables

List of Figures

Chapter 1

Plasma Wakefield Acceleration

1.1 Introduction

Particle accelerators are an essential tool for particle physicists [59], who use them to search for subatomic particles. The utility of accelerators to science, however, extends well beyond just as a means to assemble a catalog of particles; they create a means to study the underlying forces in nature. Moreover, they enable man to probe fundamental questions about the existence of the universe. For example, why is there more matter than antimatter? Beyond this, all of the known particles, including antimatter, only account for 4% of the universe; what is the rest? What happened in the first moments after the big bang? Why do particles have mass? Are there extra hidden dimensions? These are few of the questions to be explored by the recently constructed Large Hadron Collider (LHC) [24,18]. In addition to the questions listed above, there is also the exciting possibility of discovering the unexpected.

A key feature of any accelerator is the amount of energy available to create new particles. As the center of mass collisional energy of these machines rises, they allow for the production of increasingly massive particles and open the door to new areas of physics. Thus, it is critical to drive the particle accelerators to higher energies. However, the increasingly high particle energies needed to explore new areas of physics requires larger, and therefore also more expensive, particle accelerators. Through the years, particle accelerators have grown from the size of a table top to the LHC, which is 27 kilometers in circumference. Conventional accelerators use radio frequency

(RF) cavities to advance particle energy; this technology is ultimately limited to accelerating fields below which damage occurs to the RF cavity: on the order of 100 MV/m. Currently there is an advanced RF-based concept for a collider, the compact linear collider (CLIC), which utilizes an accelerating field of 150 MV/m [74]. The size and cost of accelerators could be reduced by inventing methods for the particles to reach their required energy in shorter distances. Shorter wavelength radiation can sustain a higher accelerating field [61]. Thus, there is a significant effort to scale down the size of accelerating structures so that they can be driven by an optical laser [33, 55, 32, 60].

Efforts presented here, however, concern an entirely different technology. The passage of a particle bunch through plasma creates a wake, which is capable of accelerating particles [68]. Plasma can not be damaged so it is not constrained to the same accelerating fields as conventional technology. For example, plasma-based accelerators have sustained an accelerating field of 100 GV/m [51], which is three orders of magnitude larger than those produced in conventional RF-based accelerating structures. For this reason plasma-based accelerators have gained a significant amount of interest [45, 9, 43].

The remainder of this chapter is organized as follows. First, there is a general description of the interaction between an ultrarelativistic electron bunch and plasma. This is followed by an examination of the accelerating and focusing properties of a plasma wakefield accelerator (PWFA). These basic properties have been demonstrated and show great promise for plasma-based accelerators; however, there are many remaining concerns. The next section of this chapter is devoted to a survey of these lingering issues. Finally, there is a summary of the codes used to simulate a PWFA.

1.2 Plasma-Based Accelerators

Plasma-based accelerators use a particle bunch to drive a wake through plasma. As the drive bunch traverses the plasma, its electromagnetic fields couple to the charge density, and therefore also the accelerating and focusing fields, of the plasma. Conventional acceleration techniques fail when the electric fields become large enough to

break down material; however, plasma-based accelerators require such fields to produce their accelerating medium. Experiments described here utilize intense electron drive bunches, which possess large enough electric fields to tunnel ionize the atoms in their vicinity [57]. Thus, these experiments do not require an external means to produce plasma; the drive bunch creates plasma as it passes through a neutral vapor. First, the front part of the bunch field ionizes the vapor, producing plasma. The electron density of the drive bunch exceeds that of the plasma, so the bunch then expels all the plasma electrons from the region around it. Next, the ions pull the plasma electrons back to the axis of bunch propagation with a time scale set by the inverse of the plasma frequency ($1/\omega_p$).

$$\omega_p^2 = \frac{n_p e^2}{m\epsilon_0}, \tag{1.1}$$

where n_p is the plasma density, e is magnitude of the charge of an electron, m is the mass of an electron, and ϵ_0 is the permittivity of free space. This produces a bubble containing a region of uniformly charged ions behind the drive bunch (see Fig. 1.1), which is characteristic of the bubble regime. The drive bunch travels at nearly the speed of light, c, so this bubble has an intrinsic length scale of $c/\omega_p = 1/k_p$. Figure 1.1 shows a simulation of a PWFA.

1.3 Accelerating Field

A relationship between time and the longitudinal position coordinate simplifies calculations of the focusing and accelerating fields, so a presentation of this relationship is now required. For simplicity, calculations use cylindrical coordinates, (r, ϕ, z), with cylindrical symmetry, $\partial_\phi = 0$, and $J_\phi = 0$, where z denotes the direction of drive bunch propagation, and t denotes time. The time scale at which the plasma electrons respond to the focusing forces of the ions in the bubble is $1/\omega_p$. Due to the high energy of the ultrarelativistic drive bunch electrons, the time it takes them to respond to the focusing forces is longer by a factor of $\sqrt{\gamma}$, where γ is their relativistic Lorentz factor. As an example, $\sqrt{\gamma}$ was almost 300 in recent experiments. Thus, the drive bunch electrons respond to the focusing forces of the ions at a much slower

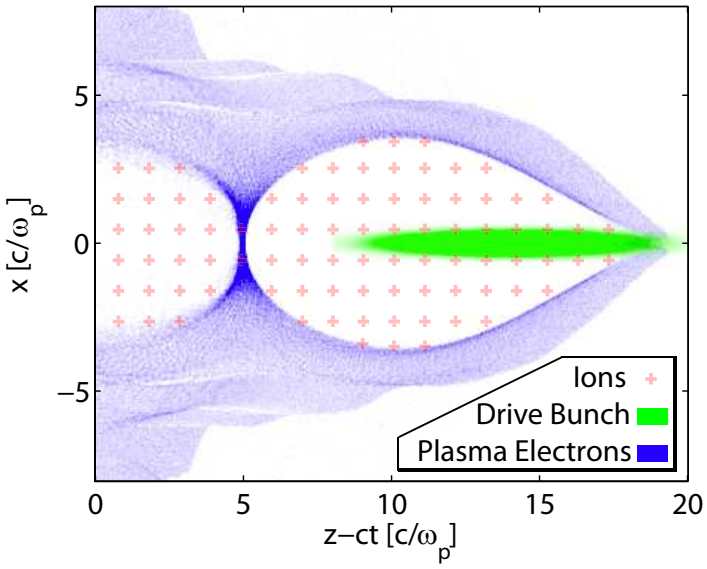

Figure 1.1: The drive bunch (green) and plasma electron density (blue) in the x and $z - ct$ plane for a PWFA, from an OSIRIS simulation [22]. A sheath of plasma electrons surrounds a region of ions with uniform charge density. The drive bunch had $1.8 \cdot 10^{10}$ electrons, $\sigma_x = \sigma_y = 1.74$ μm, $\sigma_z = 20$ μm, and drove a wake in a plasma of density, $n_p = 2.7 \cdot 10^{23}$ m^{-3} ($c/\omega_p = 10$ μm).

rate. Relative to the plasma electrons, the drive bunch electrons remain approximately frozen relative to each other and travel at roughly the speed of light in the z direction, which makes the drive bunch fields a function of $(z - ct)$ instead of z and t separately. The resulting plasma wake then has fields and potentials that are also dependent on $(z - ct)$ instead of z and t separately. Any field or potential, F, in a PWFA driven by an ultrarelativistic bunch has the following relationship between its z and t partial derivatives.

$$-c\frac{\partial F}{\partial z} = \frac{\partial F}{\partial t}. \tag{1.2}$$

This simple relationship between z and t is now combined with Maxwell's equations to derive the source term for the accelerating field, E_z [12]. The ϕ component of Faraday's law and the r component of Ampere's law are required for this derivation. Equation 1.3 is Ampere's law with t derivatives replaced by z derivatives.

$$\frac{\partial B_\phi}{\partial z} = -\mu_0 J_r + \frac{1}{c}\frac{\partial E_r}{\partial z}. \tag{1.3}$$

A substitution of Eq. 1.3 into the ϕ component of Faraday's law yields Eq. 1.4.

$$\begin{aligned} \frac{\partial E_z}{\partial r} &= \frac{\partial E_r}{\partial z} - c\frac{\partial B_\phi}{\partial z}. \\ &= \frac{\partial E_r}{\partial z} - c(-\mu_0 J_r + \frac{1}{c}\frac{\partial E_r}{\partial z}). \\ &= \mu_0 c J_r. \end{aligned} \tag{1.4}$$

As r approaches infinity E_z goes to zero, so the integral over r of $\partial_r E_z$ yields E_z:

$$E_z(r, z-ct) = -\mu_0 c \int_r^\infty dr' J_r(r', z-ct). \tag{1.5}$$

Thus, the radial current is the source term for E_z. As the drive bunch expels the plasma electrons, there is a negative radial current, which results in a positive E_z. Likewise, a negative E_z occurs as the ions in the bubble pull the plasma electrons back to the axis. When the plasma sheath reaches its maximum radius, R_m, the integrated radial current goes to zero, as does E_z.

A simple model for a PWFA is now developed, which connects the accelerating field to features of the plasma wake. Let R denote the radial extent of the ion bubble. Assume all the plasma electrons initially inside R occupy a plasma sheath with the radial range of R to $R+w$. Let v_r denote the average radial velocity of the electrons in this region. Under the assumption that $w \ll R$, the electron density in the sheath is $n_p R/(2w)$. Note, there is no radial current inside the bubble, so $E_z(r, z-ct)$ is independent of r inside the plasma sheath. Equation 1.6 displays E_z for $r < R$.

$$E_z = \mu_0 c n_p e R v_r/2 = (mc\omega_p/e)(v_r/c)(k_p R/2). \tag{1.6}$$

This equation shows that the accelerating field has a scale of $mc\omega_p/e$ when R is significant compared to the plasma length scale ($1/k_p$) and plasma electrons have radial velocities near c. While this is a simplistic model, it still shows the basic scale and nature of the accelerating field in a PWFA. Figure 1.2 displays the on-axis E_z from the simulation corresponding to Fig. 1.1.

An exact analytic solution to the interaction of the drive bunch and the plasma does not exist, so particle-in-cell (PIC) codes are used to calculate fields and wake

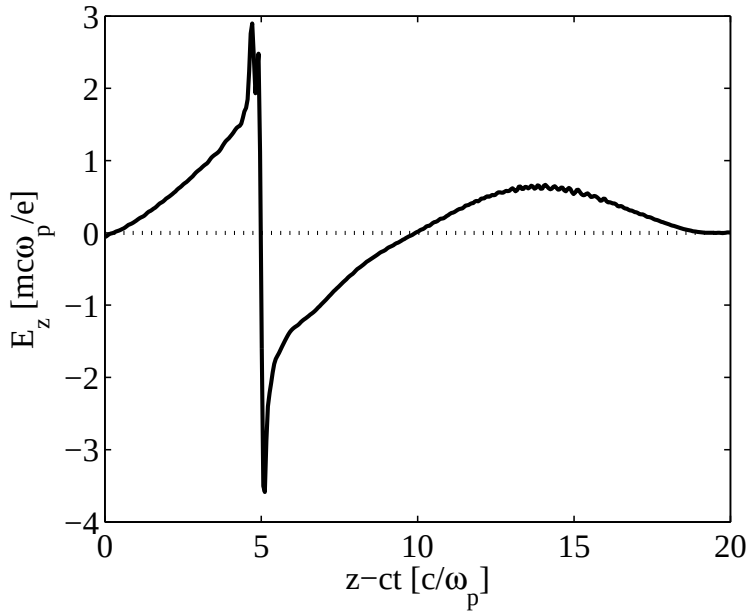

Figure 1.2: Longitudinal electric field in a PWFA, from an OSIRIS simulation. The drive bunch had $1.8 \cdot 10^{10}$ electrons, $\sigma_x = \sigma_y = 1.74$ μm, $\sigma_z = 20$ μm, and drove a wake in a plasma of density $n_p = 2.7 \cdot 10^{23}$ m^{-3} ($mc\omega_p/e = 50$ GV/m, and $c/\omega_p = 10$ μm).

properties. There is, however, a simple nonlinear theory that describes the basic physics of the interaction between the drive bunch and the plasma in the nonlinear bubble regime [48, 47]. In this regime, the plasma electrons reside in a sheath outside of the ion bubble. The simple nonlinear theory models the $\rho - J_z/c$ source term from these plasma electrons as constant in the radial range of the plasma sheath. Simulations show that the plasma electrons remain confined in the sheath as they follow a trajectory around the ion bubble. The simple theory calculates the trajectory of an electron on the innermost part of the plasma sheath, at $r = R$, and assumes that the plasma sheath follows the trajectory of this electron. Thus, the innermost electron path determines the trajectory of R. Then, R and its derivatives with respect to z specifies the charge and current distribution, which governs the fields in the system. The simple theory requires an assumption for the width of the plasma sheath. However, for R large compared to $1/k_p$, the simple theory becomes independent of

the width assumption, resulting in the following differential equation for R [48, 47].

$$R\frac{d^2R}{d\tau^2} + 2(\frac{dR}{d\tau})^2 + 1 = \frac{8\lambda r_e}{k_p^2 R^2}, \tag{1.7}$$

where $\tau = z - ct$, λ is the number of drive bunch electrons per unit longitudinal length as a function of τ, and r_e is the classical electron radius. Inside the bubble,

$$E_z = -\frac{n_p e R}{2\epsilon_0}\frac{dR}{d\tau}. \tag{1.8}$$

Equation 1.7 is useful for finding the scale of how E_z changes as a function of τ. Consider a position in the bubble behind the drive bunch. In this region Eq. 1.7 becomes

$$R\frac{d^2R}{d\tau^2} + 2(\frac{dR}{d\tau})^2 + 1 = 0, \tag{1.9}$$

which is equivalent to

$$\frac{d}{d\tau}(R\frac{dR}{d\tau}) + (\frac{dR}{d\tau})^2 + 1 = 0. \tag{1.10}$$

Near R_m, where $dR/d\tau \approx 0$, this equation is simplified to

$$\frac{d}{d\tau}(R\frac{dR}{d\tau}) = -1. \tag{1.11}$$

This implies the following relationship for the partial derivative of E_z with respect to τ inside the wake, which is used in Ch. 3 to investigate the focusing fields experienced by the trapped electrons.

$$\frac{\partial E_z}{\partial \tau} = -\frac{n_p e}{2\epsilon_0}\frac{d}{d\tau}(R\frac{dR}{d\tau}) = \frac{n_p e}{2\epsilon_0}. \tag{1.12}$$

At the front and back of the ion bubble, where there is significant radial motion of the sheath, the assumption of $dR/d\tau \approx 0$ is no longer appropriate. Thus, Eq. 1.12 is not valid for these locations.

1.4 Focusing Fields

Transverse focusing forces are an important property of the PWFA. The use of Maxwell's equations in conjunction with the relationship shown in Eq. 1.2 produces the source term for the focusing forces. A substitution of Gauss' law, Eq. 1.13, into the z component of Ampere's law, Eq. 1.14, yields a formula for $E_r - cB_\phi$ inside the bubble [12, 64].

$$\frac{\partial E_z}{\partial z} = \frac{\rho}{\epsilon_0} - \frac{\partial}{r\partial r}(rE_r). \tag{1.13}$$

$$\begin{aligned} \frac{1}{r}\frac{\partial}{\partial r}(rB_\phi) &= \mu_0 J_z - \frac{1}{c}\frac{\partial E_z}{\partial z}. \\ &= \mu_0 J_z - \frac{1}{c}(\frac{\rho}{\epsilon_0} - \frac{\partial}{r\partial r}(rE_r)). \end{aligned} \tag{1.14}$$

$$\frac{\partial}{\partial r}(r(E_r - cB_\phi)) = \frac{r}{\epsilon_0}(\rho - \frac{J_z}{c}). \tag{1.15}$$

Thus, $E_r - cB_\phi$ is determined entirely by the charge density and the longitudinal component of the current density.

Since the electron density of the drive bunch is much greater than that of the plasma, it clears the plasma electrons from its volume. However, consider an electron on the axis of bunch propagation. This electron would not experience a transverse electric field so it would remain on axis as the drive bunch passed. Before proceeding into an interpretation of the source terms for the focusing fields, it is worth presenting a quantitative description of the electrons close to the axis. Consider the effects of a Gaussian electron drive bunch with N_d electrons, $\sigma_x = \sigma_y$, longitudinal length of σ_z, and peak electron density of n_b on one of these electrons. Near the peak density of the drive bunch, E_r is linear in r. Let $t = 0$ denote the time when the middle of the bunch is aligned with the plasma electron. The plasma electron experiences a time dependent electric field of

$$E_r(t) = -\frac{n_b e r(t)}{2\epsilon_0}\exp(-\frac{c^2t^2}{2\sigma_z^2}). \tag{1.16}$$

Equation 1.17 is then appropriate for describing the radial position of the plasma

electron as a function of time (assuming nonrelativistic motion).

$$\frac{d^2r(t)}{dt^2} - r(t)\frac{n_b e^2}{2m\epsilon_0}\exp(-\frac{c^2t^2}{2\sigma_z^2}) = 0. \tag{1.17}$$

A combination of a change in variable to $u = ct/\sigma_z$ and the use of a dimensionless constant, A_p, yields the following differential equation for the evolution of r.

$$\frac{d^2r(u)}{du^2} - r(u)A_p\exp(-\frac{u^2}{2}) = 0. \tag{1.18}$$

$$A_p = \frac{n_b(k_p\sigma_z)^2}{2n_p}. \tag{1.19}$$

The initial conditions for Eq. 1.18 are $r = r_0$ and $dr/du = 0$ at $t = -\infty$. A point of interest is the radial position of the plasma electron after the core of the bunch has just passed at $t = \sigma_z/c$ ($u = 1$). Since this is a linear differential equation, it does not depend on the absolute value of r_0, it only depends on the value of A_p. Figure 1.3 shows the position of the plasma electron after the bunch has passed for various values of A_p. The quantity $r(t = \sigma_z/c)/r_0$ is extremely large even for small

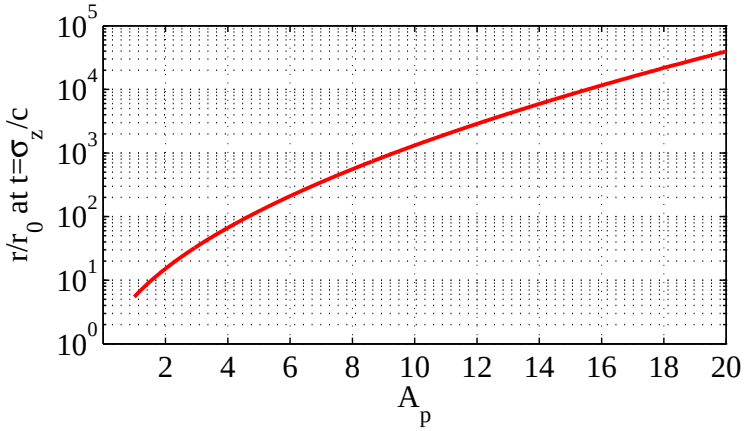

Figure 1.3: The position of a plasma electron after the passing of an electron bunch, plotted as a function of A_p, a dimensionless variable.

values of A_p. Typical drive bunch parameters have σ_z on the order of $1/k_p$. Also, $n_b \gg n_p$ in the nonlinear bubble regime. For $k_p\sigma_z = 1$ and $n_b = 10n_p$, $A_p = 5$. The corresponding value of $r(t = \sigma_z/c)/r_0$ is 122. This means that plasma electrons from outside a radius of $\sigma_x/122$ would be expelled to σ_x or greater as the bunch passes.

Thus, the drive bunch electrons are effectively the only free electrons inside the bubble; however, they do not produce a net contribution to the source term for focusing in Eq. 1.15. Therefore, the source term in the bubble results entirely from the static ions ($\rho = n_p e$). By symmetry E_r and $B_\phi = 0$ at $r = 0$, so the integral over r of Eq. 1.15 yields $E_r - cB_\phi$ inside the plasma bubble:

$$E_r - cB_\phi = \frac{n_p e r}{2\epsilon_0}. \tag{1.20}$$

The remaining fields that contribute to the transverse focusing forces are: E_ϕ, B_r, and B_z. An important term for examining these fields is A_ϕ. In the Lorentz gauge, the current density is the source term for the vector potential:

$$\mathbf{A}(\mathbf{x},t) = \frac{\mu_0}{4\pi}\int d^3x' \frac{\mathbf{J}(\mathbf{x'}, t - |\mathbf{x}-\mathbf{x'}|/c)}{|\mathbf{x}-\mathbf{x'}|}. \tag{1.21}$$

The ϕ component of the vector potential is determined by the azimuthal and radial current density:

$$\begin{aligned} A_\phi(r,\phi,z,t) &= \frac{\mu_0}{4\pi}\int_0^\infty dr' r' \int_{-\infty}^{\infty} dz' \int_{-\pi}^{\pi} d(\phi'-\phi) \times \\ &\quad \frac{J_\phi(r',\phi'-\phi,z',t')\cos(\phi'-\phi) + J_r(r',\phi'-\phi,z',t')\sin(\phi'-\phi)}{\sqrt{r^2 + r'^2 - 2rr'\cos(\phi'-\phi) + (z-z')^2}}. \end{aligned} \tag{1.22}$$

$$t' = t - \frac{1}{c}\sqrt{r^2 + r'^2 - 2rr'\cos(\phi'-\phi) + (z-z')^2}. \tag{1.23}$$

Recall, J_ϕ is assumed to be zero. Since there is azimuthal symmetry, J_r is even in $\phi' - \phi$. The denominator of the above equation is also even in $\phi' - \phi$, but $\sin(\phi' - \phi)$ is odd in $\phi' - \phi$. Thus, the argument of the integral is odd in $\phi' - \phi$, making $A_\phi = 0$. Since $A_\phi = 0$ and $\partial_\phi = 0$, E_ϕ, B_r, and B_z are all zero:

$$E_\phi = -\frac{1}{r}\frac{\partial \Phi}{\partial \phi} - \frac{\partial A_\phi}{\partial t} = 0. \tag{1.24}$$

$$B_r = \frac{1}{r}\frac{\partial A_z}{\partial \phi} - \frac{\partial A_\phi}{\partial z} = 0. \tag{1.25}$$

$$B_z = \frac{1}{r}\frac{\partial (rA_\phi)}{\partial r} - \frac{1}{r}\frac{\partial A_r}{\partial \phi} = 0. \tag{1.26}$$

Therefore, the only fields that contribute to the transverse focusing forces are E_r and B_ϕ.

It is now important to introduce the transverse emittance, which is the area of a particle bunch in the $x - p_x$ (or $y - p_y$) phase space. This is a crucial property for the application of any particle bunch. For example, the transverse emittance controls the minimum wavelength that can be produced coherently from a particle bunch in a free electron laser. Also, the transverse emittance limits the minimum transverse spot size achievable in a collider, which in turn controls the colliders luminosity. For this reason, the effect of propagation on the transverse emittance in a PWFA is particularly important.

The linear focusing forces created by the fields shown in Eq. 1.20 are ideal; they conserve the transverse normalized emittances, $\epsilon_{N,x}$ and $\epsilon_{N,y}$, of a particle bunch. This property is apparent from an investigation of the Lorentz force equation. An ultrarelativistic electron bunch has $v_z \approx c$, so the Lorentz force equation renders the following differential equation for the propagation of the transverse coordinates.

$$\begin{aligned} \frac{dp_x}{dt} &= -e(E_x - cB_y). \\ &= -e(E_r - cB_\phi)\cos(\phi). \\ &= -\frac{n_p e^2 x}{2\epsilon_0}. \end{aligned} \tag{1.27}$$

Since v_z is not exactly c, it is worth investigating the size of the corrections to this formula. First, the terms E_r and $-cB_\phi$ are of the same order, so all errors come from the difference between v_z and c. Let $\dot{x} = dx/dz$, and v denote the velocity of the particle. Consider an ultrarelativistic particle traveling in the $x - z$ plane; its longitudinal velocity is

$$v_z = v\cos(\dot{x}) = c\sqrt{1 - \frac{1}{\gamma^2}}\cos(\dot{x}). \tag{1.28}$$

Both $1/\gamma$ and $\dot{x}$ are much smaller than one, so this equation can be simplified as

$$v_z \approx c(1 - \frac{1}{2\gamma^2})(1 - \frac{\dot{x}^2}{2}). \tag{1.29}$$

The angular size of a matched bunch is given by the following equation.

$$\langle \dot{x}^2 \rangle = \frac{k_p \epsilon_{N,x}}{\sqrt{2\gamma^3}}. \tag{1.30}$$

As an example, in recent experiments $k_p \epsilon_{N,x} = 6$. Thus, $\dot{x}^2$ is of order $\gamma^{-3/2}$, which makes the difference between v_z and c of order $c\gamma^{-3/2}$. Recent experiments utilized a drive bunch with $\gamma > 80{,}000$, making this a very small correction.

Since $v_z \approx c$, the time derivatives of Eq. 1.27 can be converted to z derivatives, resulting in the following equation for the transverse propagation of an electron.

$$\ddot{x} + \frac{\dot{\gamma}}{\gamma}\dot{x} + Kx = 0. \tag{1.31}$$

$$K = \frac{k_p^2}{2\gamma}, \tag{1.32}$$

where K denotes the focusing strength. Equation 1.33 shows the definition of the geometric emittance for the x coordinate.

$$\epsilon_x^2 = \langle x^2 \rangle \langle \dot{x}^2 \rangle - \langle x\dot{x} \rangle^2. \tag{1.33}$$

The geometric emittance is related to the normalized emittance by a factor of γ: $\epsilon_{N,x} = \gamma \epsilon_x$. A z derivative of the geometric emittance reveals that $\epsilon_{N,x}$ is conserved:

$$\begin{aligned} \dot{\epsilon_x^2} &= 2\langle x^2 \rangle \langle \dot{x}\ddot{x} \rangle - 2\langle x\dot{x} \rangle \langle x\ddot{x} \rangle. \qquad (1.34) \\ &= -\frac{2\dot{\gamma}}{\gamma}\epsilon_x^2. \\ (\dot{\gamma\epsilon_x}) &= \dot{\epsilon_{N,x}} = 0. \qquad (1.35) \end{aligned}$$

Note, the transportation properties of y are the same as x.

1.4.1 Emittance Growth from Multiple Coulomb Scattering

Emittance growth is an important issue for the PWFA. The previous section shows that the normalized emittance is conserved for linear focusing forces. These linear focusing fields result from the assumption of a uniform charge distribution in the

ion bubble. The actual charge is not uniformly distributed; it is allocated in delta functions (ions), which are uniformly distributed. This type of charge distribution leads to multiple Coulomb scattering (MCS) and causes emittance growth [35]. Here, the MCS emittance growth of an electron bunch traveling through a PWFA in the nonlinear bubble regime is calculated. The calculation uses well-established formulas for angular scatter in a neutral vapor and then extends the range of the Coulomb interaction to include the effects of traveling through an ion bubble. Emittance growth is negligible for materials with a low atomic number; however, it becomes large for high atomic numbers.

The emittance growth of a bunch traveling through a neutral vapor can be found from the angular scatter through the vapor, which is related to the radiation length. Equation 1.36 is a formula for this length, L_r [75].

$$L_r = \frac{716.4\text{cm}^{-2} N_A}{nZ(Z+1)\log(287/\sqrt{Z})}, \tag{1.36}$$

where Z is the atomic number of traversed material, N_A is Avogadro's number in units of mole^{-1}, and n is the density of the neutral vapor. The rate of angular scatter for an ultrarelativistic electron through a neutral vapor is related to L_r through the following equation [73].

$$\frac{d\langle\theta^2\rangle_{vapor}}{dz} = \frac{1}{2\gamma^2 L_r}\left(\frac{20\text{MeV}}{mc^2}\right), \tag{1.37}$$

where θ is angle in the $x-z$ plane relative to the z axis.

In recent PWFA experiments, the electric field from the drive bunch was strong enough to completely expel electrons from its volume, which created an ion bubble in the plasma. Scattering through an ion bubble extends the range of the Coulomb interaction. In a neutral vapor, if the incident particle does not come within the atomic dimensions of an atom, the nucleus of the atom is shielded by its electrons. The same is not true when the incident particle travels through a uniform region of atoms. To account for the fact that there are charged ions, another Coulomb scattering term is added with a range from the atomic radius, R_a, to the radius of the ion bubble, R.

The radial kick in momentum that an incident electron receives from a charged ion is found from a time integration of the ion's radial electric field. This radial kick is then projected onto the x plane and is converted into an angle after dividing by the electron's momentum.

$$\theta = \frac{\Delta p_x}{p} = \frac{e^2 Q \cos(\phi)}{2\pi p v \epsilon_0 b}, \tag{1.38}$$

where p is the electrons momentum, b is the ion's impact parameter, v is the electron velocity, Qe is the ion charge, and ϕ is the azimuthal angle of the ion. Next, Eq. 1.38 is converted to a squared angle expectation value by integrating over an ion that is randomly placed with $R_a < b < R$. Since the incident particle is ultrarelativistic, $pv = \gamma mc^2$.

$$\langle \theta^2 \rangle = (\frac{Qe^2}{2\pi\gamma mc^2\epsilon_0})^2 \frac{\log(R/R_a)}{(R^2 - R_a^2)}. \tag{1.39}$$

Angular scatters from individual ions add in quadrature. The reason for this is seen from an investigation of the expectation value for the addition of two angles.

$$\langle \theta_f^2 \rangle = \langle (\theta_1 + \theta_2)^2 \rangle = \langle \theta_1^2 \rangle + \langle \theta_2^2 \rangle. \tag{1.40}$$

Angular scatter from individual ions are just as likely to be positive as negative, so $\langle \theta_1 \theta_2 \rangle$ is zero. A total rate of change in the mean square scatter from the ions is found by multiplying the number of ions that the incident particle will intercept per unit length by the expected mean square scatter from one:

$$\begin{aligned} \frac{d\langle \theta^2 \rangle_{ion}}{dz} &= \langle \theta^2 \rangle n\pi(R^2 - R_a^2). \\ &= \frac{nQ^2e^4}{4\pi\gamma^2 m^2 c^4 \epsilon_0^2} \log(R/R_a). \end{aligned} \tag{1.41}$$

The total rate of angular scatter growth, $d\langle \theta_T^2 \rangle / dz$, is the addition of the vapor (Eq.

1.37) and the ion (Eq. 1.41) scattering terms:

$$\begin{aligned} \frac{d\langle\theta_T^2\rangle}{dz} &= \frac{d\langle\theta^2\rangle_{ion}}{dz} + \frac{d\langle\theta^2\rangle_{vapor}}{dz}, \\ &= \frac{k_p^2 r_e}{\gamma^2} S, \\ S &= Q[\log(R/R_a) + \frac{1.78Z(Z+1)}{Q^2}\log(287/\sqrt{Z})], \end{aligned} \tag{1.42}$$

where $n_p = Qn$. As the impact parameter increases from below the atomic radius to above it, the scatter transitions from nuclear to ionic. Here, the analysis evaluates the ion scattering as though it abruptly turns on at an impact parameter of R_a. A choice of R_a that is too large or too small would under- or overestimate the scattering, respectively. However, Eq. 1.42 is only logarithmically dependent on R_a. For the experiments presented in this dissertation, R exceeds R_a by roughly five orders of magnitude, so even an order of magnitude error in the choice of R_a would not produce an appreciable difference to the calculated scattering. Thus, the exact value chosen for R_a is not critical. For $Z = 1$, the terms from the ion bubble and neutral vapor are roughly the same size; however, for higher Z the term from the neutral vapor dominates.

The transverse size of the bunch in the plasma relates the rate of angular scatter to the emittance growth. This size is found from an investigation of the focusing forces. Equation 1.31 is appropriate for describing an ultrarelativistic electron oscillating through the bunch axis of the ion bubble. For a bunch of constant energy, there are conditions in which its transverse size does not change along the accelerator. A matched bunch is one that satisfies these conditions. The conditions for matching are found from z derivatives of the transverse bunch size.

$$\frac{d\langle x^2\rangle}{dz} = 2\langle x\dot{x}\rangle. \tag{1.43}$$

$$\frac{d^2\langle x^2\rangle}{dz^2} = 2(\langle\dot{x}^2\rangle + \langle x\ddot{x}\rangle). \tag{1.44}$$

The second derivative of x with respect to z is substituted from Eq. 1.31, assuming $\dot{\gamma} = 0$, into these equations. By setting the first two z derivates equal to zero, it insures that all higher order derivatives are also zero. This makes $\langle x^2\rangle$ a constant,

with the following criteria for a matched bunch [50].

$$\langle x\dot{x}\rangle = 0. \tag{1.45}$$
$$\langle \dot{x}^2\rangle = \frac{k_p^2}{2\gamma}\langle x^2\rangle.$$

A substitution of these criteria into Eq. 1.33 yields the following relationship between the emittance and the bunch transverse size.

$$\epsilon_x = \frac{k_p}{\sqrt{2\gamma}}\langle x^2\rangle. \tag{1.46}$$

Note, an accelerating bunch that starts matched retains the conditions expressed in Eq. 1.45 [50].

The rate of emittance growth is found from a z derivative of Eq. 1.33.

$$\epsilon_x\dot{\epsilon_x} = \langle x^2\rangle\langle \dot{x}\ddot{x}\rangle - \langle x\dot{x}\rangle\langle x\ddot{x}\rangle. \tag{1.47}$$

A substitution for $\ddot{x}$ is now required. The quantity $\ddot{x}$ must include not only the contributions from Eq. 1.31, but also the rate of angular growth from scattering (as shown in the following equation).

$$\ddot{x} = -\frac{\dot{\gamma}}{\gamma}\dot{x} - \frac{k_p^2}{2\gamma}x + \dot{\theta_T}. \tag{1.48}$$

Next, this equation is substituted into Eq. 1.47, yielding

$$\epsilon_x\dot{\epsilon_x} = -\frac{\dot{\gamma}}{\gamma}\epsilon_x^2 + \langle x^2\rangle\langle \dot{x}\dot{\theta_T}\rangle + \langle x\dot{x}\rangle\langle x\dot{\theta_T}\rangle. \tag{1.49}$$

As long as the relative angular growth for one oscillation in the $x - \dot{x}$ plane is small, a bunch that starts matched will remain closely matched. Thus, the $\langle x\dot{x}\rangle$ term is dropped. Recall, the other scattering term for Eq. 1.49 was calculated for Eq. 1.42.

$$\langle \dot{x}\dot{\theta_T}\rangle = \frac{1}{2}\frac{d\langle\theta_T^2\rangle}{dz}. \tag{1.50}$$

The rate of the normalized emittance growth is found by substituting Eq. 1.42 and

Eq. 1.50 into Eq. 1.49, multiplying by γ, and dividing by ϵ_x.

$$\gamma\dot{\epsilon_x} + \dot{\gamma}\epsilon_x = \dot{\epsilon_{N,x}} = \frac{k_p^2 r_e S}{2\epsilon_x \gamma}\langle x^2 \rangle. \tag{1.51}$$

This equation is further simplified by a substitution of the relationship between the emittance and the transverse size (see Eq. 1.46):

$$\dot{\epsilon_{N,x}} = \frac{k_p r_e S}{\sqrt{2\gamma}}. \tag{1.52}$$

The derivative in z can be converted to a derivative in γ [52].

$$\frac{d\epsilon_{N,x}}{d\gamma} = \frac{k_p r_e S}{\dot{\gamma}\sqrt{2\gamma}}. \tag{1.53}$$

An integral of this equation from the initial Lorentz factor, γ_i, to the final Lorentz factor, γ_f, yields the following formula for the change in the normalized emittance, $\Delta\epsilon_{N,x}$.

$$\Delta\epsilon_{N,x} = \frac{\sqrt{2}k_p r_e S}{\dot{\gamma}}(\sqrt{\gamma_f} - \sqrt{\gamma_i}). \tag{1.54}$$

This equation is simplified a step further by assuming that the bunch is accelerated with an electric field of $mc^2 k_p/e$, which yields that $\dot{\gamma} = k_p$.

$$\Delta\epsilon_{N,x} = \sqrt{2} r_e S(\sqrt{\gamma_f} - \sqrt{\gamma_i}). \tag{1.55}$$

One current scheme for the PWFA is to use it at the end of a conventional linear collider to double the energy of a witness electron bunch [42]. As an example, Eq. 1.55 was used to calculate the emittance growth from doubling the energy of an electron bunch initially at 500 GeV through various materials that have been singly ionized (see Fig. 1.4). The ion bubble radius was set to $2.5{\cdot}10^{-5}$ m, and the atomic radius was set to 10^{-10} m. Projected emittances for the International Linear Collider are $\epsilon_{N,y} = 4{\cdot}10^{-8}$ m and $\epsilon_{N,x} = 9.6{\cdot}10^{-6}$ m [62]. At $Z \approx 60$ the y normalized emittance is doubled. This example shows that emittance growth is negligible for low Z materials; however, becomes important for high Z materials.

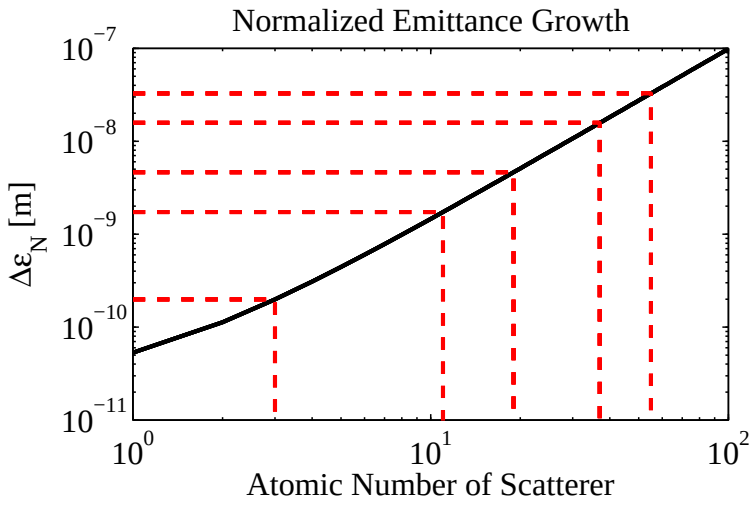

Figure 1.4: Normalized emittance growth from MCS during the energy doubling of a 500 GeV electron bunch, shown for various singly-ionized materials. The red dotted lines represent the normalized emittance growth of the following elements: Li $= 2.0 \cdot 10^{-10}$ m, Na $= 1.7 \cdot 10^{-9}$ m, K $= 4.6 \cdot 10^{-9}$ m, Rb $= 1.6 \cdot 10^{-8}$ m, and Cs $= 3.3 \cdot 10^{-8}$ m.

1.5 Remaining Issues

Recent experiments demonstrated the extraordinary focusing and accelerating properties of electron bunches in a PWFA [56, 26, 9] (see Ch. 5). In addition, there has also been preliminary experimental tests of positron acceleration in a PWFA [7], but more work is needed. There are several issues for both electron and positron bunches that develop during long propagation, which are not yet fully understood. Future experiments will test the remaining obstacles in the path to creating a plasma-based collider. This section is an outline of these remaining issues.

1.5.1 Plasma Electron Trapping

Recent experiments exhibited the trapping of plasma electrons in the wake of the drive bunch [58]. A plasma-based collider would use one particle bunch to drive the wake and a witness bunch to capture the energy of the wake. The trapped electrons reside at positions near an optimal place for the witness bunch and are capable of draining energy from the wake. Figures 1.5 and 1.6 illustrate how trapping affects the

wake. Chapter 2 presents the physics of electron trapping in a PWFA and methods of relieving the effects of the trapped electrons. These electrons can be detrimental to plasma-based colliders; however, their properties establish them as interesting all on their own. Chapter 3 covers the physics of the trapped electron properties.

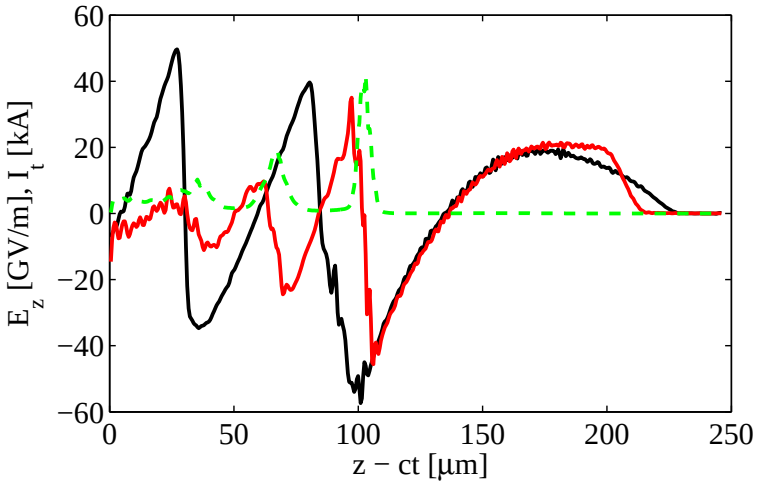

Figure 1.5: Electric field loading by the trapped electrons, from an OSIRIS simulation. The black line represents the on-axis E_z before a significant amount of trapped electrons accumulate, the red line denotes the on-axis E_z after the trapped electrons have loaded the electric field, and the green dotted line shows the current profile of the trapped electrons, I_t. The drive bunch had $1.8 \cdot 10^{10}$ electrons, $\sigma_x = \sigma_y = 1.74$ μm, $\sigma_z = 30$ μm, and drove a wake in a vapor with a lithium density of $2.7 \cdot 10^{23}$ m^{-3} and a helium density of $8.1 \cdot 10^{21}$ m^{-3}.

1.5.2 Positron Acceleration and Propagation

It is not enough to accelerate electrons to high energies in a PWFA. To build high energy electron-positron linear colliders, positron bunches must also be accelerated. Experiments have shown that positron acceleration in a PWFA is possible [7]. However, they also indicate that the transverse focusing forces are nonlinear [54]. The focusing forces of the ion bubble are only ideal for electron witness bunches; propagation of positrons requires a zero or negative on-axis charge density. Since the plasma electrons are not static or uniform in density, the regions of positron focusing change rapidly with $z - ct$ and are nonlinear. Figures 1.7 and 1.8 contrast the

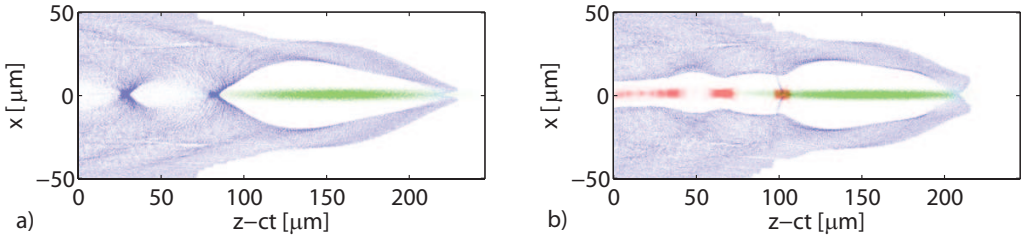

Figure 1.6: Wake loading by the trapped electrons, from an OSIRIS simulation. a) The wake before a significant amount of trapped electrons accumulate. b) The wake after being loaded by the trapped electrons. The colors red, green, and blue represent the electron density of the trapped electrons, the drive bunch, and the plasma electrons (from lithium). The drive bunch had $1.8 \cdot 10^{10}$ electrons, $\sigma_x = \sigma_y = 1.74$ μm, $\sigma_z = 30$ μm, and drove a wake in a vapor with a lithium density of $2.7 \cdot 10^{23}$ m^{-3} and helium density of $8.1 \cdot 10^{21}$ m^{-3}.

focusing and accelerating properties of an electron and positron driven plasma wake, respectively. One method to avoid the focusing problems for positrons is to propagate them through a hollow channel plasma, which has a density depression on the bunch axis. However, there is not yet a proven method for generating one.

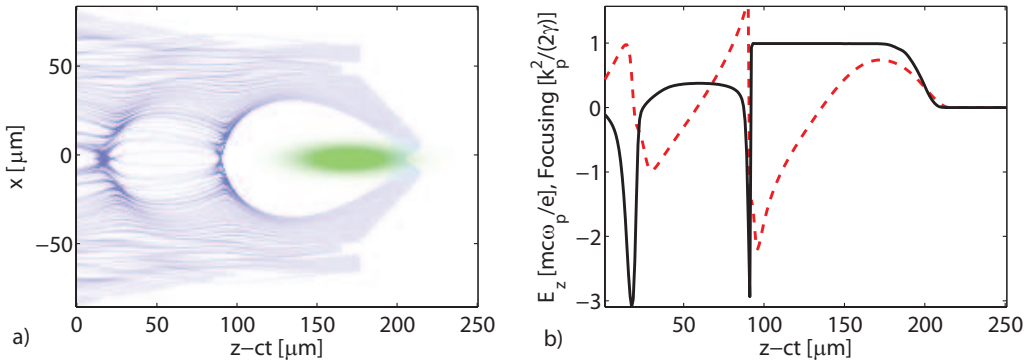

Figure 1.7: The focusing and accelerating properties of a plasma wake driven by an electron bunch, from a QuickPIC simulation [27]. The red dotted line represents E_z and the black line denotes the focusing strength of the wake, where positive is focusing for electrons. Note, the region of uniformly charged ions has a uniform focusing strength. The drive bunch had $1.8 \cdot 10^{10}$ electrons, $\sigma_x = \sigma_y = 5$ μm, $\sigma_z = 20$ μm, and drove a wake in a lithium vapor of density $2.7 \cdot 10^{23}$ m^{-3}.

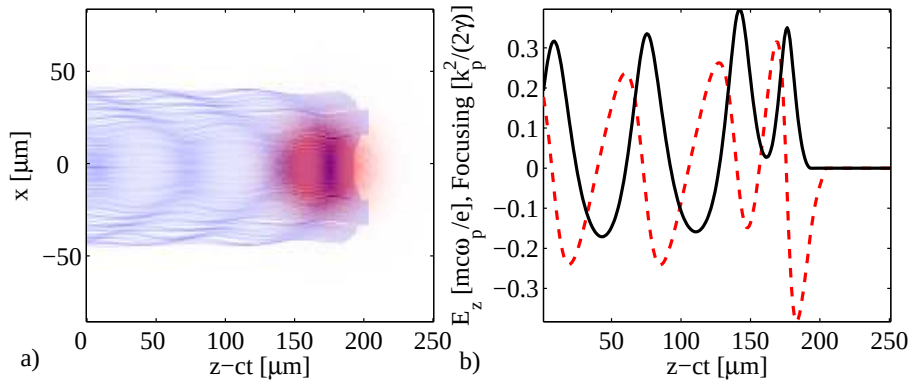

Figure 1.8: The focusing and accelerating properties of a plasma wake driven by a positron bunch, from a QuickPIC simulation. The red dotted line represents E_z and the black line denotes the focusing strength of the wake, where positive is focusing for positrons. Note, the varying on-axis charge density results in a varying focusing strength. The drive bunch had $1.8 \cdot 10^{10}$ positrons, $\sigma_x = \sigma_y = 15$ μm, $\sigma_z = 20$ μm, and drove a wake in a lithium vapor of density $2.7 \cdot 10^{23}$ m^{-3}.

1.5.3 Ion Motion

The linear focusing forces, shown in Eq. 1.20, rely on the ions remaining static and uniform. However, current bunch parameters for plasma-based colliders indicate that the drive bunches will have transverse fields large enough to substantially affect the ion positions as they pass [65]. Consider the effect of a Gaussian electron drive bunch with N_d electrons, $\sigma_x = \sigma_y$, longitudinal length of σ_z, and peak density of n_b on an ion of mass M and charge Qe. Near the peak density of the drive bunch, E_r is linear in r. Let t=0 denote the time when the middle of the bunch is aligned with the ion. The ion experiences the time dependent electric field of Eq. 1.16. Equation 1.56 is then appropriate for describing the radial position of the ion as a function of time.

$$\frac{d^2r(t)}{dt^2} + r(t)\frac{Qn_be^2}{2M\epsilon_0}\exp(-\frac{c^2t^2}{2\sigma_z^2}) = 0. \tag{1.56}$$

A combination of a change of variable to $u = ct/\sigma_z$ and the use of a dimensionless constant, A_{ion}, yields the differential equation for the evolution of r as

$$\frac{d^2r(u)}{du^2} + r(u)A_{ion}\exp(-\frac{u^2}{2}) = 0. \tag{1.57}$$

$$A_{ion} = \frac{Qn_b e^2\sigma_z^2}{2M\epsilon_0 c^2}. \tag{1.58}$$

A manipulation of the constant A_{ion} yields

$$A_{ion} = \frac{Q\sigma_z r_e k_p N_d}{\epsilon_N}\frac{m}{M}\sqrt{\frac{\gamma}{4\pi}}. \tag{1.59}$$

Since A_{ion} is the only constant in Eq. 1.57, the amount of ion motion is entirely determined by it.

The initial conditions for Eq. 1.57 are $r = r_0$ and $dr/du = 0$ at $t = -\infty$. A point of interest is the radial position of the ion after the core of the bunch has just passed at $t = \sigma_z/c$ ($u = 1$). Since this is a linear differential equation, it does not depend on the absolute value of r_0, it only depends on the value of A_{ion}. Figure 1.9 shows the position of the ion after the bunch has passed. There is a catastrophic collapse

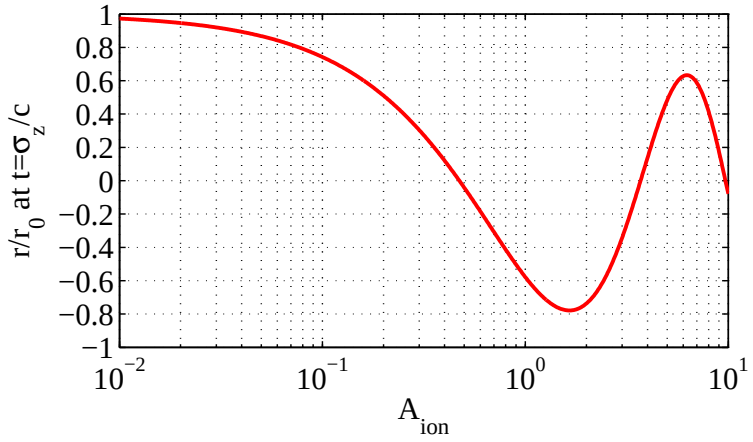

Figure 1.9: The position of an ion after the passing of an electron bunch, plotted as a function of A_{ion}, a dimensionless variable.

of the ion when $r = 0$ at $t = \sigma_z/c$; this occurs for $A_{ion} = 0.473$. A less severe collapse occurs for $A_{ion} = 10^{-1}$, and a negligible collapse occurs for $A_{ion} = 10^{-2}$.

Current parameters for the witness bunch in a PWFA-based collider are 10^{10} electrons, $\sigma_z = 10$ μm, $n_p = 10^{23}$ m^{-3} ($1/k_p = 16.8$ μm), $\epsilon_{N,x} = 2$ μm, $\epsilon_{N,y} = 0.05$ μm, and an energy of 500 GeV ($\gamma = 978{,}475$). Since $\epsilon_{N,x}$ is much larger than $\epsilon_{N,y}$, σ_x is also much larger than σ_y. Thus, this bunch would not be cylindrically symmetric. In this case, a substitution of $\epsilon_N = \sqrt{\epsilon_{N,x}\epsilon_{N,y}}/2$ is appropriate for A_{ion}. Consider the effect the drive bunch has on a singly-ionized lithium atom. The quantity $A_{ion} = 2.34$, which corresponds to a catastrophic amount of ion motion. In this case, the ion density would not be uniform, so the wake would not posses the linear radial focusing forces shown in Eq. 1.20. This would create transverse emittance growth for the bunch traveling in this wake. The effect of ion motion can be reduced with higher mass ions, but multiple ionizations are problematic for these ions. Also, as shown in Sec. 1.4.1, emittance growth from multiple coulomb scattering becomes a significant issue for high Z materials [35].

1.5.4 Electron-Hosing Instability

As a drive bunch traverses plasma it expels the plasma electrons from the bunch axis, which creates a sheath of plasma electrons surrounding a region of ions. If the back of the drive bunch is displaced transversely from the front of the drive bunch, the electrons in the back would pass closer to one side of the plasma sheath than the other. This would result in a displacement to the center of the plasma sheath, which would then act back on the drive bunch. A transverse instability occurs from this interaction. The basic physics of this instability is described by the following set of coupled differential equations [72, 41]:

$$\frac{\partial^2 x_b}{\partial z^2} + \frac{k_p^2}{2\gamma}(x_b - x_s) = 0, \tag{1.60}$$

$$\frac{\partial^2 x_s}{\partial \tau^2} + \frac{k_p^2}{2}(x_s - x_b) = 0, \tag{1.61}$$

where x_b and x_s are the x position of the center of the bunch and of the plasma sheath, respectively, at a given longitudinal position. These equations are useful for quantifying the growth of the transverse instability as the drive bunch travels along z. As an example, consider a drive bunch that has a discontinuity in its transverse

position at $\tau = 0$. At positions in front of this discontinuity both x_b and x_s are zero, but for $\tau < 0$ the initial discontinuity leads to the transverse hosing instability. The initial conditions for this example are

$$\begin{aligned} x_b(z=0,\tau) &= x_{b0}\Theta(-\tau), \\ x_s(z=0,\tau\geq 0) &= 0, \\ \frac{\partial x_b(z=0,\tau)}{\partial z} &= 0, \\ \frac{\partial x_s(z=0,\tau\geq 0)}{\partial \tau} &= 0, \end{aligned} \tag{1.62}$$

where Θ is a step function. The asymptotic solution of these initial conditions for $\tau < 0$ and $1 \ll -k_p\tau/\sqrt{2} \ll k_p z/\sqrt{2\gamma}$ is [41]

$$\begin{aligned} x_b(z,\tau) &= x_{b0}(6\pi)^{-1/2}(\frac{k_p z}{\sqrt{2\gamma}})^{-1/6}(\frac{-k_p\tau}{\sqrt{2}})^{-1/3} \\ &\times \exp(\frac{3\sqrt{3}}{4}(\frac{k_p z}{\sqrt{2\gamma}})^{1/3}(\frac{-k_p\tau}{\sqrt{2}})^{2/3}) \\ &\times \cos(\frac{k_p z}{\sqrt{2\gamma}} - \frac{3}{4}(\frac{k_p z}{\sqrt{2\gamma}})^{1/3}(\frac{-k_p\tau}{\sqrt{2}})^{2/3} + \frac{\pi}{12}). \end{aligned} \tag{1.63}$$

These equations show an exponential growth in x_b, which is characteristic for an instability. This instability should appear when $k_p z/\sqrt{2\gamma}$ and $-k_p\tau/\sqrt{2}$ are large. Recent experiments utilized drive bunches that were comparable or larger in length than $\sqrt{2}/k_p$ and propagated these drive bunches until $(k_p z/\sqrt{2\gamma})^{1/3} = 5.89$. However, this transverse instability has not yet appeared to be a showstopper for the PWFA. More detailed analyses suggest the hosing growth occurs at a slower rate than that given by Eq. 1.60 [28]. Future experiments will further probe this transverse instability.

1.5.5 Head Erosion

Section 1.4 showed that a PWFA has ideal focusing properties for electrons; however, this is only true inside the ion bubble. Since the drive bunch creates the bubble by field ionizing neutral vapor and expelling the plasma electrons, there exist electrons at the front of the bunch which do not experience this focusing. In the absence of the focusing from the ion bubble, the electrons in this region expand transversely,

which causes the front of ionization to move further into the head of the bunch. This process is termed as head erosion. In recent experiments this effect kept the drive bunch from reaching energy depletion [9]. Figure 1.10 shows an illustration of head erosion from a QuickPIC simulation.

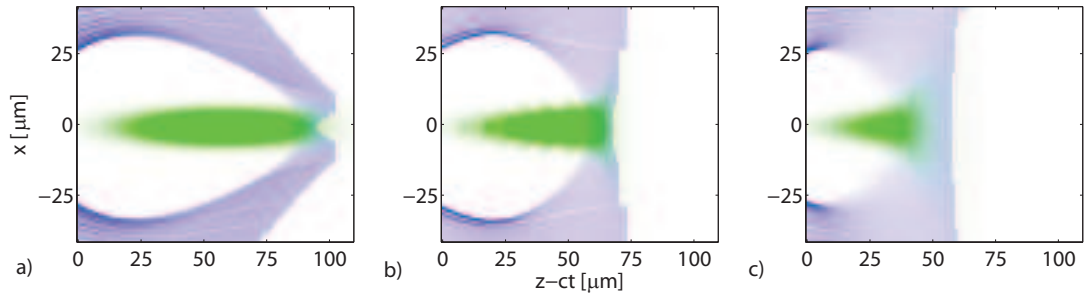

Figure 1.10: The erosion of the drive bunch, from a QuickPIC simulation; a), b), and c) show the wake at propagation distances of 0.5, 15, and 30 cm, respectively. The color green denotes the drive bunch electron density and blue represents the plasma electron density. The drive bunch had $1.77 \cdot 10^{10}$ electrons, $\sigma_x = \sigma_y = 2.9$ μm ($\epsilon_{N,x} = \epsilon_{N,y} = 100$ μm), $\sigma_z = 20$ μm, $\gamma = 41,000$, and drove a wake in a lithium vapor with $c/\omega_p = 10$ μm.

The rate of head erosion, v_e, is expressed as a dimensionless ratio of the distance of erosion into the bunch over the distance of bunch propagation. Figure 1.10's corresponding simulation suggests that the first half of the bunch is eroded after a propagation distance of 30 cm. Thus, $v_e \approx \sigma_z/30$ cm $\approx 6.7 \cdot 10^{-5}$. The scale for this erosion rate can be understood through simple arguments. Recall Eq. 1.17, which describes the expulsion of plasma electrons from the bunch. The time scale in this differential equation is $\omega_p^{-1}(2n_p/n_b)^{1/2}$. Thus, $k_p^{-1}(2n_p/n_b)^{1/2}$ is the scale for the distance in the bunch between no focusing and the perfect focusing of the ion bubble.

Now consider the transverse propagation of an electron at the front of the bunch, where there is no focusing. Let x_0 and $\dot{x}_0$ represent this electron's initial transverse coordinates. The transverse coordinate as a function of propagation distance, z, is

$$x(z) = x_0 + \dot{x}_0 z. \tag{1.64}$$

A collection of these freely propagating electrons has a transverse size of

$$\langle x^2 \rangle = \langle x_0^2 \rangle + 2z\langle x_0 \dot{x}_0 \rangle + z^2 \langle \dot{x}_0^2 \rangle. \tag{1.65}$$

The simulation used a matched bunch, so the above equation (using $\langle x_0 \dot{x}_0 \rangle = 0$ and Eq. 1.30) is simplified as

$$\langle x^2 \rangle = \langle x_0^2 \rangle + z^2 (\frac{k_p \epsilon_{N,x}}{\sqrt{2\gamma^3}}). \tag{1.66}$$

Above a certain transverse size, σ_{ionize}, the electric field of the bunch is no longer large enough to ionize the surrounding gas. The front of ionization passes a position in the bunch once its transverse size increases above σ_{ionize}. Note, the peak electric field required to ionize lithium for a Gaussian bunch with $\sigma_z = 20$ μm is 5.5 GV/m (see Sec. 2.5). For the peak current of the simulated bunch this field corresponds to $\sigma_{ionize} = 84$ μm. This is much greater than the initial transverse bunch size, so the propagation distance for the transverse size to become equal to σ_{ionize}, z_{ionize}, is

$$z_{ionize} = \sigma_{ionize} \frac{(2\gamma^3)^{1/4}}{\sqrt{k_p \epsilon_{N,x}}}. \tag{1.67}$$

The quantity v_e is then expressed as

$$v_e = \frac{1}{k_p z_{ionize}} \sqrt{\frac{2n_p}{n_b}}. \tag{1.68}$$

A substitution of the quantities in this equation yields $v_e \approx 3.1 \cdot 10^{-5}$. Note, this rate is roughly a factor of two below that shown in the simulation. This should be expected since this calculation only describes the erosion rate at the bunch's peak current position. The simulated bunch was Gaussian, so the erosion rate was higher away from the peak current position. A more detailed derivation and discussion of head erosion is shown in Ian Blumenfeld's dissertation [8].

1.5.6 Plasma Wake Loading

Recent PWFA experiments used one bunch to both create the wake and sample the accelerating field. This type of interaction inherently produces a large energy

spread and is naturally not a way to build a collider. Instead, a plasma-based collider would use a drive bunch to create a plasma wake and a witness bunch to sample it. Multiple drive bunches would then be used to successively increase the energy of a single witness bunch.

Particle colliders rely on being able to accurately control the center of mass energy at the interaction point. Thus, a plasma-based particle accelerator must be able to deliver its witness bunch with a small energy spread. Another quantity of interest is the transformer ratio. This is the ratio of the accelerating field experienced by the witness bunch over the maximum decelerating field experienced by the drive bunch. The transformer ratio governs the number of drive bunches required to get a witness bunch to a given energy: as this ratio increases the number of drive bunches required decreases. Also, the power consumption of a particle accelerator is of concern. For this reason, the efficiency of the energy transfer from the drive to the witness bunch is also important. Figure 1.11 displays the energy spread, transformer ratio, and efficiency from a set of QuickPIC simulations, which varied the separation between a drive and a witness bunch. In addition, Fig. 1.12 shows the loaded wake from the simulation which minimized the energy spread of the witness bunch.

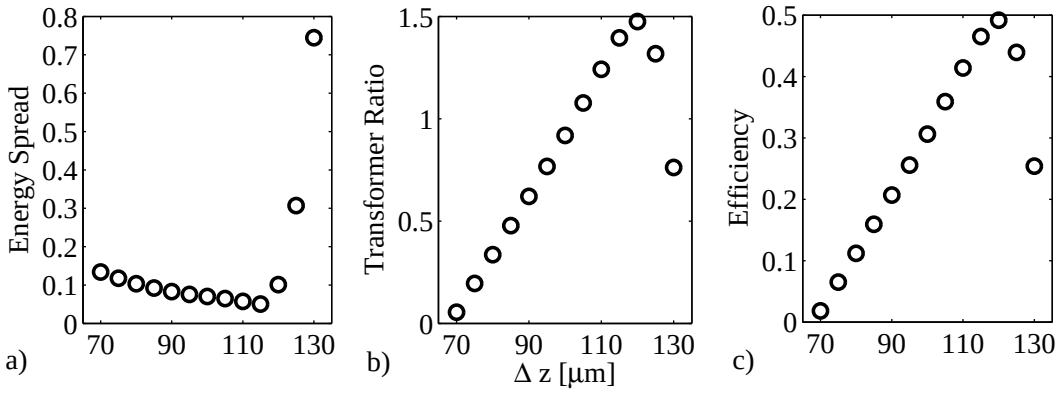

Figure 1.11: The relative rms energy spread (a), transformer ratio (b), and efficiency (c) calculated in a set of QuickPIC simulations, which varied the distance between the drive and the witness bunch, Δz. The drive bunch had $3 \cdot 10^{10}$ electrons with $\sigma_z = 30$ μm, and the witness bunch had 10^{10} electrons with $\sigma_z = 10$ μm; both bunches had $\sigma_x = \sigma_y = 3$ μm ($\epsilon_{N,x} = \epsilon_{N,y} = 84$ μm) and $\gamma = 48,924$. The wake was driven in a lithium vapor of density 10^{23} m^{-3}.

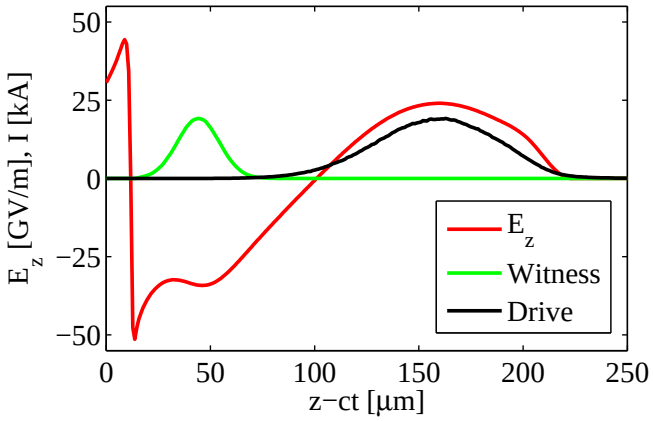

Figure 1.12: A properly loaded accelerating field along with the corresponding current profiles of the drive and witness bunches, from a QuickPIC simulation. The drive bunch had $3 \cdot 10^{10}$ electrons with $\sigma_z = 30$ μm, and the witness bunch had 10^{10} electrons with $\sigma_z = 10$ μm; both bunches had $\sigma_x = \sigma_y = 3$ μm ($\epsilon_{N,x} = \epsilon_{N,y} = 84$ μm) and $\gamma = 48,924$. These bunches were separated by 115 μm, and the wake was driven in a lithium vapor of density 10^{23} m^{-3}.

The QuickPIC simulations show that Gaussian drive and witness bunches achieve reasonable accelerating properties. Furthermore, a combination of theory and simulation work shows that a proper shaping of the drive and witness bunch current profile is capable of yielding smaller energy spreads, higher transformer ratios, and better efficiencies [70]. Future experiments will test the energy spread, transformer ratio, and efficiency of a drive and witness bunch in a PWFA.

1.6 Simulations

Exact analytic solutions for the electric and magnetic fields of a PWFA in the nonlinear bubble regime do not exist. A considerable amount of work was devoted to developing approximate solutions [48, 47]. Simulations are useful for deriving more detailed information about the dynamics in a PWFA. Additionally, simulations can provide a benchmark for the approximate solutions and yield insight into the physical processes. For these reasons, simulations are particularly important to PWFA research.

The specific simulation codes used in this dissertation are OSIRIS [22] and QuickPIC [27]. These codes both use a particle-mesh method of simulating the interactions of particle bunches with plasma. In this method, plasma electrons and drive bunch particles are represented by simulation particles. At present, computers do not have the capability to simulate each individual drive bunch and plasma particle. Instead, a macro-particle represents a group of particles. These macro-particles have the same charge to mass ratio as the individual particles so they follow the same trajectory in response to the fields of the system. The macro-particles have continuous coordinates; however, their charge and current are deposited on a grid. Both codes, as used in this dissertation, model the ions in the plasma as static. These codes solve Maxwell's equations on the simulation grid, subject to the boundary conditions. The electric and magnetic fields from this solution are used in conjunction with the Lorentz force equation to iterate the macro-particle coordinates to the next time step. This leads to a new distribution of the macro-particles, which become re-deposited on the grid, and so forth.

The natural unit for distance in the system is $1/k_p$, so the spatial grid size is typically a small fraction of this. Similarly, the simulation time steps are a small fraction of $1/\omega_p$. These simulation codes have been run for lengths of time which exceed $10^5/\omega_p$. The drive bunch moves at the speed of light so it interacts with plasma over a distance that is greater than $10^5/k_p$. A simulation of this entire region would require millions of grid points in z, which is computationally intractable. For this reason, both OSIRIS and QuickPIC implement a moving window algorithm. The window moves at the same speed as the drive bunch, so the bunch remains fixed relative to it. For the simulations in this dissertation, the moving window algorithm allows for a reduction of the window size in z to on the order of $10/k_p$.

OSIRIS and QuickPIC allow for the initialization of multiple drive bunches, plasmas, and neutral vapors, with numerous types of distributions. Both of these codes include the physics of field ionization for the neutral vapor, modeled according to the Ammosov, Delone, and Krainov (ADK) ionization formula (more detail shown in Ch. 2). The second chapter demonstrates that the inclusion of field ionization is crucial for the simulation of plasma electron trapping.

1.6.1 OSIRIS

The preceding paragraphs give a basic description of OSIRIS [22]. This code was benchmarked to PWFA experimental results and shows good agreement [7]. In contrast to QuickPIC, this code is available in both two- and three-dimensional versions. Also, for reasons discussed in the next section, OSIRIS generated all of the plasma electron trapping simulations in this dissertation.

1.6.2 QuickPIC

Three-dimensional simulations can be computationally cumbersome, but are at times necessary. The code QuickPIC [27] was developed to decrease the computational time required for these simulations. As is discussed earlier in this chapter, the time scale for the drive bunch transverse oscillation is much larger than that for the plasma electrons. While OSIRIS advances all particle coordinates with a time step that is a small fraction of $1/\omega_p$, QuickPIC only iterates the drive bunch coordinates with a time step that is a small fraction of $\sqrt{\gamma}/\omega_p$. The quantity γ can be quite large, so this allows QuickPIC to be orders of magnitude faster than the three-dimensional version of OSIRIS.

One of the key assumptions utilized by QuickPIC is the relationship shown in Eq. 1.2. Consider the effect of this relationship on the wave equation for the scalar and vector potential, Φ and $\overrightarrow{A}$, respectively.

$$\nabla^2\Phi - \frac{1}{c^2}\frac{\partial^2}{\partial t^2}\Phi = -\frac{\rho}{\epsilon_0} \quad \Rightarrow \quad \nabla_\perp^2\Phi = -\frac{\rho}{\epsilon_0}. \tag{1.69}$$

$$\nabla^2\overrightarrow{A} - \frac{1}{c^2}\frac{\partial^2}{\partial t^2}\overrightarrow{A} = -\mu_0\overrightarrow{J} \quad \Rightarrow \quad \nabla_\perp^2\overrightarrow{A} = -\mu_0\overrightarrow{J}. \tag{1.70}$$

These equations show that the potentials are only coupled to the sources at the same $z-ct$ position. QuickPIC finds a solution for the fields in three dimensions by solving the two-dimensional Poisson's equations at each $z-ct$ position.

The following is a simplified description of the iteration routine used in QuickPIC. First, the simulation box is split into grids in x, y, and $z-ct$. The iteration starts with an initialization of the plasma electrons at the front of the box in $z-ct$. Plasma electrons at this location have yet to react to the incoming drive bunch, so the plasma

is neutral and produces no contribution to the source terms in the wave equation. Thus, at the front of the box, the only fields come from the drive bunch. The plasma electrons then move in response to these fields, leading to plasma charge separation and current. These sources then become the initialization for the plasma at the next $z - ct$ grid, making the grid size in $z - ct$ determine the iteration time step for the plasma electrons. The plasma interaction to the fields in this new grid is again calculated, now including the fields from the plasma. This creates a new plasma distribution that is passed to the next grid, and so forth. Once this iteration process gets to the back of the box, the code has simulated how the plasma responds to the drive bunch and the resultant wakefield. The plasma electron simulation particles are discarded at this point.

Next, the code calculates the response of the drive bunch to the fields of the plasma. A grid size in $z - ct$ is usually some small fraction of $1/k_p$, so the simulation time step for the plasma electrons is a small fraction of $1/\omega_p$; however, the drive bunch particles do not require this small of a time step. QuickPIC assumes that the fields from the plasma in the moving simulation box remain fixed and utilizes the Lorentz force equation to iterate the coordinates of the drive bunch electrons. Instead of moving the bunch forward in time by a small fraction of $1/\omega_p$, it is advanced by a small fraction of $\sqrt{\gamma}/\omega_p$. The drive bunches in recent PWFA experiments had a value of γ that exceeded 80,000, so the required simulation time step for its electrons is more than two orders of magnitude larger than that of the plasma electrons. Once the drive bunch particles are iterated, the response of the plasma electrons to the new drive bunch distribution is calculated. This simulation method saves orders of magnitude in computation time by not re-simulating the response of the plasma electrons to the drive bunch before the bunch has had time to evolve. The QuickPIC code has been benchmarked to OSIRIS [27] and is found to be in good agreement with recent experiments [9].

This decrease in computation time comes at an extreme price, at least for the trapped electron. By discarding the plasma electrons at the end of each drive bunch time step, QuickPIC makes a clear distinction between plasma and drive bunch electrons. Once a plasma electron starts to become trapped it acquires a v_z close to c and remains in the simulation box longer than a drive bunch time step, so QuickPIC

can no longer delete it. However, at least initially, the drive bunch time steps are too large for these trapped electrons. For QuickPIC to properly simulate the evolution of these trapped electrons, it would have to decrease its drive bunch time step to a small fraction of $1/\omega_p$. This defeats the purpose of QuickPIC's assumptions. For this reason, this code is not used to model plasma electron trapping.

Chapter 2

Plasma Electron Trapping

2.1 Introduction

It was found experimentally that a drive bunch with a peak current on the order of 10 kA or greater could trap and accelerate plasma electrons in the wake of a PWFA. The trapping of plasma electrons was apparent from the comparison of charge measuring toroids upstream and downstream of the plasma source: there was as much as four times as many electrons coming out of the plasma than went into it. In addition, some of these trapped electrons were accelerated to tens of GeV in energy and emitted partially coherent optical Cherenkov radiation.

This chapter examines the physics of electron trapping in a PWFA. First, a constant of motion yields a theoretical framework to study trapping. Next, the limitations of this framework are discussed. A connection is then made between the onset of trapping and the drive bunch properties. The ionization of neutral atoms is an important part of the trapping process, so the next section presents the formalism for field ionization. Then, there is an investigation of the effect of the plasma density and species on electron trapping. As was briefly discussed in Ch. 1, trapped electrons can be a hindrance to a PWFA, so this chapter concludes with a discussion of methods to terminate plasma electron trapping.

2.2 Constant of Motion

An Investigation of a constant of motion yields a basic understanding of electron trapping in a PWFA. The Hamiltonian is only a function of position, x_i, the momentum conjugate to the position, P_i, and of time, t. Since the only dependence the electromagnetic Hamiltonian, H, has to the position and time coordinates is through the potentials, H is only dependent on $(z-ct)$ instead of z and t separately. Thus, H also has the property displayed by Eq. 1.2. This is apparent from a partial derivative of H with respect to z.

$$H(x_i, P_i, t) = \sqrt{\sum_i (P_i - qA_i)^2 c^2 + m^2 c^4} + q\Phi. \tag{2.1}$$

$$\begin{aligned} \frac{\partial H}{\partial z} &= \sum_i \frac{\partial H}{\partial A_i}\frac{\partial A_i}{\partial z} + \frac{\partial H}{\partial \Phi}\frac{\partial \Phi}{\partial z}, \\ &= \sum_i \frac{\partial H}{\partial A_i}\frac{-1}{c}\frac{\partial A_i}{\partial t} + \frac{\partial H}{\partial \Phi}\frac{-1}{c}\frac{\partial \Phi}{\partial t}, \\ &= \frac{-1}{c}\frac{\partial H}{\partial t}, \end{aligned} \tag{2.2}$$

where A_i represents the components of the vector potential and Φ represents the scalar potential. Particles in a system with this property have a constant of motion, $H - cP_z$.

$$H - cP_z = \gamma mc^2 - cp_z + q\Psi, \tag{2.3}$$

$$\Psi = \Phi - cA_z, \tag{2.4}$$

where p_z is the z component of the momentum, q is the charge of the particle, and P_z is the canonical momentum conjugate to the z position $(p_z + qA_z)$. A substitution of Hamilton's equations of motion,

$$-\frac{dP_i}{dt} = \frac{\partial H}{\partial x_i}, \tag{2.5}$$

$$\frac{dx_i}{dt} = \frac{\partial H}{\partial P_i}, \tag{2.6}$$

into a derivative of $H - cP_z$ with respect to time yields zero, proving the quantity is a constant of motion.

$$\begin{aligned}
\frac{d}{dt}(H - cP_z) &= \frac{dH}{dt} + c\frac{\partial H}{\partial z}, \\
&= \sum_i (\frac{\partial H}{\partial x_i} \cdot \frac{dx_i}{dt} + \frac{\partial H}{\partial P_i} \cdot \frac{dP_i}{dt}) + \frac{\partial H}{\partial t} + c\frac{\partial H}{\partial z}, \\
&= \sum_i (-\frac{dP_i}{dt} \cdot \frac{dx_i}{dt} + \frac{dx_i}{dt} \cdot \frac{dP_i}{dt}) + \frac{\partial H}{\partial t} + c\frac{\partial H}{\partial z}, \\
&= (\frac{\partial}{\partial t} + c\frac{\partial}{\partial z})H = 0.
\end{aligned} \tag{2.7}$$

The drive bunch is ultrarelativistic, so the plasma wake that follows has a phase velocity that is extremely close to the speed of light. To become trapped in this wake, an electron's speed must approach the speed of light and do so fast enough that it does not fall out the back of the plasma bubble. The electrons start at rest, so initially $\gamma mc^2 - cp_z = mc^2$. Field ionization creates the plasma [57], so electrons escape atoms with different initial values of Ψ, Ψ_i. The constant of motion enforces a condition between Ψ and Ψ_i:

$$\gamma mc^2 - cp_z - e\Psi = mc^2 - e\Psi_i. \tag{2.8}$$

Note, the quantity $\gamma mc^2 - cp_z > 0$, so an inequality between Ψ and Ψ_i must be satisfied:

$$\Psi_i - \Psi < \frac{mc^2}{e}. \tag{2.9}$$

An electron can not go to a location where the difference between its initial Ψ and that of its position is greater than mc^2/e.

Trapping of electrons is governed by Ψ, so it is important to now present the basic

behavior of Ψ. Partial derivatives of Ψ yield how it changes with r and z:

$$\begin{aligned} \frac{\partial \Psi}{\partial r} &= \frac{\partial \phi}{\partial r} - c\frac{\partial A_z}{\partial r}, \\ &= \frac{\partial \phi}{\partial r} + \frac{\partial A_r}{\partial t} - \frac{\partial A_r}{\partial t} - c\frac{\partial A_z}{\partial r}, \\ &= -E_r + c(\frac{\partial A_r}{\partial z} - \frac{\partial A_z}{\partial r}), \\ &= -(E_r - cB_\phi). \end{aligned} \tag{2.10}$$

$$\begin{aligned} \frac{\partial \Psi}{\partial z} &= \frac{\partial \phi}{\partial z} - c\frac{\partial A_z}{\partial z}, \\ &= \frac{\partial \phi}{\partial z} + \frac{\partial A_z}{\partial t}, \\ &= -E_z. \end{aligned} \tag{2.11}$$

Equation 1.20 demonstrates that $E_r - cB_\phi$ is a positive quantity inside the plasma bubble. Section 1.3 showed that at the center of the plasma bubble $E_z = 0$ (because $J_r \approx 0$), at positions in front of the center E_z is positive, and behind the center E_z is negative. Thus, the quantity Ψ reaches a maximum, Ψ_m, on axis at the center of the bubble, where its partial derivatives are zero and the radius of the bubble, R, reaches a maximum, R_m. Figure 2.1 displays the Ψ contours from an OSIRIS simulation. Although the drive bunch has large transverse fields, it makes no direct contribution to E_z or $E_r - cB_\phi$. Thus, it does not contribute directly to the shape of Ψ.

At the back of the bubble, where the plasma sheath reaches the bunch axis, the fields switch from accelerating and focusing. Since E_z is connected to the radial current and $E_r - cB_\phi$ is related to the on-axis charge density, the position where the wake changes to decelerating can differ slightly from where it turns to defocusing. Let Ψ_f denote Ψ on axis at the back of the bubble, where fields change from accelerating and focusing to either decelerating or defocusing (whichever occurs first). An electron that satisfies $\Psi_i > mc^2/e + \Psi_f$ can not slip out of the back of the bubble; thus, it becomes trapped in the wake. Figure 2.2 illustrates this trapping mechanism. The value of Ψ_f can extend below zero, but will not be below $-mc^2/e$. Otherwise, the electrons that support the wake, which have $\Psi_i \approx 0$, would become trapped and quickly load E_z at this position and increase Ψ_f.

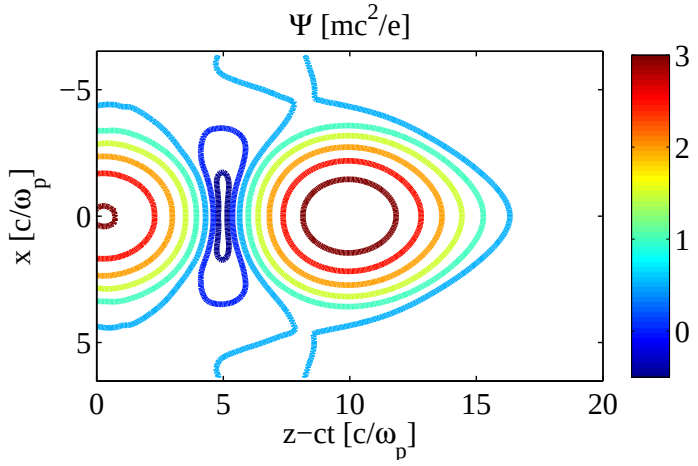

Figure 2.1: Ψ contours in a plasma wake, from an OSIRIS simulation. The drive bunch had $1.8 \cdot 10^{10}$ electrons, $\sigma_x = \sigma_y = 1.74$ μm, $\sigma_z = 20$ μm, and drove a wake in a plasma of density, $n_p = 2.7 \cdot 10^{23}$ m^{-3} ($c/\omega_p = 10$ μm).

For the experiments described in this dissertation, trapping occurs due to the presence of two gas species in the vapor: helium and lithium, with ionization energies of 24.6 and 5.4 eV, respectively. A heat-pipe oven is the source for the neutral vapor [53]. Over the central heated region of this oven there is pure lithium vapor with a density of $2.7 \cdot 10^{23}$ m^{-3} and a full width at half maximum (FWHM) length of 85 cm, but in the cool regions on either side of the heated region there is pure helium. In between, there is a transition region where both species are present (see Sec. 4.3). Ionization of lithium atoms occurs first from the drive bunch electric field, releasing the electrons that support the plasma wake. As the fields of the bunch and the wake increase, the helium atoms become ionized inside the wake. This allows the electrons from helium to satisfy the trapping criterion, making them the source of the observed trapped electrons.

2.3 Wake Loading by Trapped Electrons

The formalism for electron trapping, just developed, relies on the fields and potentials being functions of $(z - ct)$ instead of z and t separately. However, as the wake collects trapped electrons, they begin to load the accelerating field. Thus, as the wake propagates further in z, its shape in $(z - ct)$ can vary. Once enough trapped

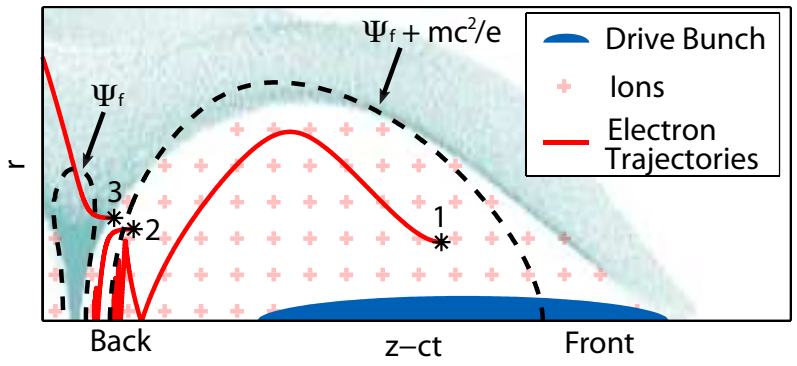

Figure 2.2: An illustration of electron trapping, calculated with OSIRIS [22]. A few example helium electron trajectories overlay an image of lithium electron density (teal), where the asterisks display the ionization location, and the dotted lines represent Ψ contours. The electrons that escape their atoms within the $\Psi_f + mc^2/e$ contour (1 and 2) become trapped, while electron 3 slips out of the wake. Reprinted with permission from [39]. Copyright 2009, American Physical Society.

electrons accumulate at the back of the wake, they can load the wake enough to push some of them into a decelerating field. These decelerating electrons would then no longer be trapped.

A two-dimensional OSIRIS simulation of a drive bunch creating a plasma wake in a mixed lithium-helium plasma serves as an illustration of this loading process. The drive bunch is a Gaussian with $1.8 \cdot 10^{10}$ electrons, matched transverse sizes of $\sigma_{x,y} = 1.74$ μm, and $\sigma_z = 20$ μm. The lithium density is $2.7 \cdot 10^{23}$ m^{-3} and there is a relative background helium density of 10%. In r and z the simulation grid size is 0.5 μm with 9 particles per cell. For this simulation, only electrons from helium atoms become trapped. Figure 2.3a shows the loading of E_z by the trapped electrons at several different propagation distances, and Fig. 2.3b displays the corresponding p_z versus $z - ct$ phase space of the trapped electrons. At a propagation distance of 84 c/ω_p (denoted by red in Fig. 2.3), the trapped electrons begin to load the wake. By $z = 146$ c/ω_p (blue), the loading is enough to push some of the formerly trapped electrons into a decelerating phase of the wake. This causes some of them to be picked up and trapped again by the next accelerating wake at $z - ct$ near 6 c/ω_p, which leads to the production of multiple trapped electron bunches (3 shown for $z = 270$ c/ω_p).

The wake loading by the trapped electrons creates problems defining whether an

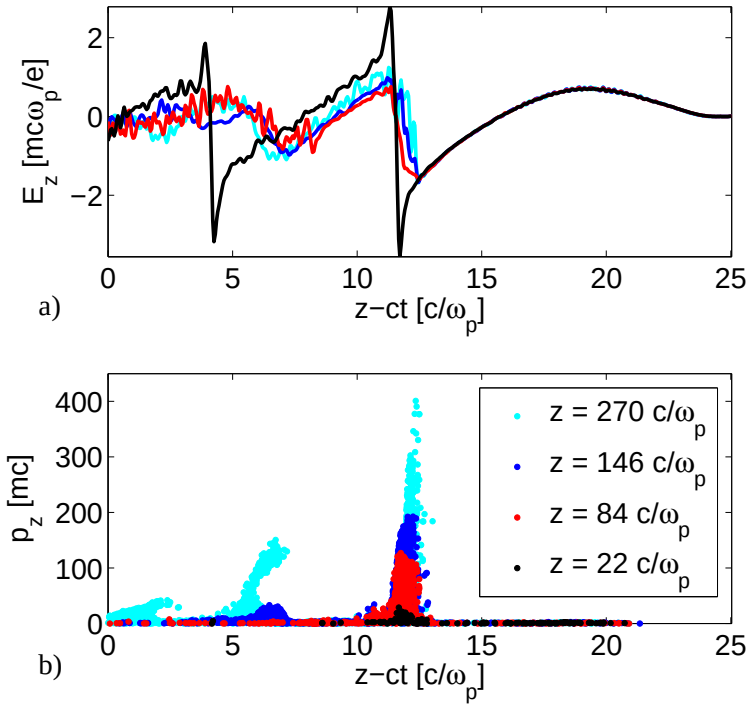

Figure 2.3: a) E_z versus $z - ct$ at several different propagation distances. b) The p_z versus $z - ct$ phase space of the trapped electrons at several different propagation distances.

electron in a simulation is indeed trapped. If the fields of the wake remained only functions of $(z - ct)$, the comparison of a simulation particle's constant of motion with Ψ_f would yield whether it would remain trapped. As Fig. 2.3 illustrates, the trapped electrons load the wake, which changes E_z and the value for Ψ_f. If there is a continuous source for trapped electrons, an electron that is classified as trapped on one time step could be pushed into a decelerating wake on the next time step. The black line of Fig. 2.4 shows the amount of trapped electrons in the first bubble for the simulation described in the previous paragraph. At very low values of z the amount of trapped charge increases very rapidly; however, this quickly loads the wake and pushes most of this charge into the decelerating phase of the wake, which quickly reduces the amount of charge classified as trapped. Then, the wake begins to slowly acquire additional trapped electrons. These newly trapped electrons begin to load the wake and eventually push themselves into the decelerating phase of the wake. This

process then repeats itself, causing a fluctuation in the number of trapped electrons (see Fig. 2.4). Note, the fluctuation in Fig. 2.4 is amplified by the noise on E_z in the simulation. The trapped electrons reside at the very back of the bubble, so small variations in E_z at this location cause large changes in the amount of trapped electrons.

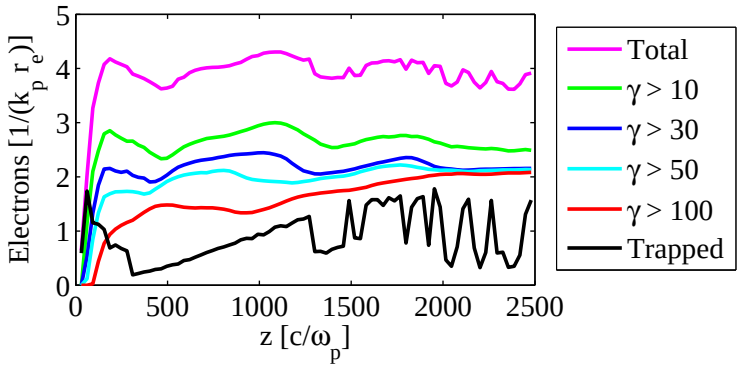

Figure 2.4: The number of electrons in the first bubble versus propagation distance. The black line denotes the number of trapped electrons, determined by the constant of motion, and the magenta line represents the total number of electrons. The rest of the line colors represent the number of electrons above a γ cutoff. Note, r_e is the classical electron radius.

As Fig. 2.4 displays, the amount of trapped charge changes rapidly throughout the course of the simulation. This does not represent something fundamental to the system, but is an artifact of how the simulation was run. In the simulation there was a constant source of helium electrons, so the wake continually collected trapped electrons. If instead the helium atoms were removed from the system at the first spike in the black line, the amount of trapped charge would stay fixed at the value of the spike. For more detail refer to Sec. 3.7, which discusses a method to avoid the fluctuation of the trapped charge and how to use the trapped electrons as a particle source.

The use of the constant of motion to determine the number of trapped electrons is problematic, so a different method is used to quantify the amount of trapped charge. This method only includes the electrons with γ greater than a cutoff. Figure 2.4 shows the number of electrons classified as trapped by this method for several different values of the cutoff. For z higher than 2000 c/ω_p the number of electrons

for cutoffs greater than and including $\gamma = 30$ converge to roughly the same value, $\approx 2/(k_p r_e)$. In addition, the value at which they converge is not entirely inconsistent with the peak values shown for the black line. For this reason a γ cutoff of 80 is used for quoting the number of trapped electrons. Also, unless stated otherwise, the number of trapped electrons quoted in simulations only includes those in the first bubble.

2.4 Drive Bunch Requirements for Trapping

This section derives the critical properties of the drive bunch that are needed to cause the onset of electron trapping. First, the simplistic model for E_z, shown in Eq. 1.6, connects the trapping requirements between Ψ_i and Ψ_f to requirements on the plasma wake. Then, the wake requirements are connected to the properties of the drive bunch. Since the scale of the distance from the center of the ion bubble to the back is set by $c/\omega_p = 1/k_p$, to reach $\Psi_i - \Psi_f = mc^2/e$ the value of $\partial_z \Psi = -E_z$ must be on the scale of $mc\omega_p/e$. The quantity $v_r < c$, so R must exceed $2/k_p$ to reach $E_z = mc\omega_p/e$ (in Eq. 1.6). Also, the time scale of the plasma electron oscillation is $1/\omega_p$ and $R = \int v_r \cdot dt$, so v_r must be comparable to c to reach $R > 2/k_p$. Thus, to trap electrons, the drive bunch must expel plasma electrons to $R > 2/k_p$ with $v_r \approx c$.

This requirement on the bubble radius is also apparent without the simplified E_z model. An integration of $\partial_r \Psi$ gives

$$\Psi(r = 0) = \int_0^\infty dr(E_r - cB_\phi). \tag{2.12}$$

The difference between Ψ_m and Ψ_f is dominated by the difference in their corresponding integrals over the interior of the bubble. Considering only this part of the integral results in $\Psi(r = 0) = \int_0^R dr(E_r - cB_\phi)$, which implies $\Psi_f = 0$ and $\Psi_m = n_p e R_m^2/(4\epsilon_0)$. For trapping to be possible $\Psi_m - \Psi_f > mc^2/e$, so R_m must be greater than $2/k_p$.

The R and v_r requirements for plasma electron trapping are now connected to drive bunch parameters. A calculation of the bunch field requirements to transfer a radial momentum of mc to the plasma electrons in the sheath partially addresses the v_r constraints. Assuming $v_\phi = 0$ and that all drive bunch electrons have $r < R$, the

t derivative of the radial momentum transferred from the drive bunch to the sheath electrons is

$$\frac{dp_r}{dt} = -e(E_r - v_z B_\phi), \tag{2.13}$$

$$= \frac{\lambda e^2}{2\pi r \epsilon_0}(1 - \frac{v_z}{c}), \tag{2.14}$$

where λ is the number of drive bunch electrons per unit longitudinal length. Let τ denote $z - ct$. A change of variables from t to τ yields a simpler differential equation:

$$\frac{dp_r}{d\tau} = -\frac{\lambda e^2}{2\pi r \epsilon_0 c}. \tag{2.15}$$

The quantity $p_r(\tau = \infty)$ is the initial radial momentum of the sheath electron, and $p_r(\tau = -\infty)$ is the radial momentum of the sheath electron after the interaction with the drive bunch. Thus, the integral of Eq. 2.15 from $\tau = \infty$ to $-\infty$ represents the radial momentum transferred as the drive bunch passes the sheath electron. A plasma sheath with $R = 2/k_p$ contains electrons initially at $r < 2/k_p$. Since the number of plasma electrons in the sheath per unit initial r is proportional to r, a higher percentage of the total number of electrons originate from larger radii. Recall, v_r represents the average radial velocity of the electrons in the sheath. Therefore, to reach $v_r \approx c$, the plasma electrons initially at $r = 2/k_p$ must have radial velocities comparable to c. The quantity r increases as the drive bunch transfers radial momentum to the electrons, making r a variable. However, the movement of r only becomes an issue once the radial velocity becomes comparable to c. Thus, to find the condition that causes the sheath electrons to move relativistically, r can be treated as a constant, $2/k_p$. The radial momentum transferred from the drive bunch to the sheath electrons initially at $r = 2/k_p$ is

$$\Delta p_r = N_d r_e k_p mc, \tag{2.16}$$

where N_d is the total number of drive bunch electrons and r_e is the classical electron radius. For v_r to approach c, Δp_r must at least be mc. This results in a critical number of drive bunch electrons, $N_{crit} = 1/(k_p r_e)$, to initiate trapping.

As the drive bunch expels plasma electrons, an ion bubble forms that screens the bunch's electric field. To create a wake with $R > 2/k_p$, the drive bunch must have a

large enough peak current to overcome this screening. A rough method of satisfying this constraint is for λ to exceed the number of ions per unit length in a cylinder of radius $2/k_p$:

$$\lambda > \pi(\frac{2}{k_p})^2 n_p = \frac{1}{r_e}. \tag{2.17}$$

The corresponding drive bunch peak current required for trapping is then $ec/r_e \approx 17$ kA, which is the Alfvén current (I_A). This is a basic way to connect R_m to the drive bunch peak current. Wei Lu et al [47] use a combination of theory and simulations to derive a more accurate relationship between R_m and the drive bunch peak current, I_d:

$$R_m k_p/2 \approx \sqrt{2I_d/I_A}. \tag{2.18}$$

Although it is not how this relation is found, Eq. 2.18 can also be obtained as the steady state solution ($d/d\tau = 0$ and $d^2/d\tau^2 = 0$) to Eq. 1.7. To achieve $R_m = 2/k_p$ requires a critical peak current, $I_{crit} = I_A/2$. Note, accounting for the part of the integration of $\partial_r \Psi$ in Eq. 2.12 that is outside the bubble allows electron trapping to occur with I_d slightly below $I_A/2$. Thus, $I_A/2$ only sets the approximate scale for the peak current required to induce electron trapping [39].

Three-dimensional particle-in-cell simulations of the experiment, using the code OSIRIS [22], provide support to the requirements on the drive bunch peak current to initiate electron trapping. These simulations have a lithium density of $2.7 \cdot 10^{23}$ m^{-3} and a relative helium density of 3%. As in the experiment, the helium only serves as the source for the trapped electrons. The simulations are of Gaussian drive bunches with $1.8 \cdot 10^{10}$ electrons, matched transverse sizes of $\sigma_{x,y} = 1.74$ μm, and $I_d = 34.5$, 17.2, 11.5, 8.62, and 6.90 kA; the quantity of trapped electrons dramatically reduces for $I_d < 6.90$ kA. In x, y, and z, the simulation grid size is 0.5 μm with either 2 or 4 particles per cell (second order interpolation [20]). The simulations run until the trapped electrons load the wake and turn off further trapping. Figure 2.5 shows how the amount of trapped electrons (γ >80) in the first bubble, N_t, increases with increasing drive bunch peak current, showing a clear onset in electron trapping near a peak current of $I_A/2$ and a saturation of trapped charge near a peak current of I_A.

For the simulations with $I_d = 17.2$, 11.5, 8.62, and 6.90 kA, all of the trapped

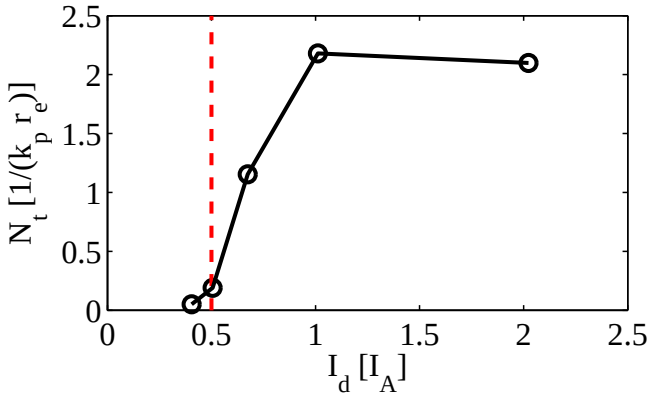

Figure 2.5: The number of trapped electrons, N_t, versus the drive bunch peak current, I_d, calculated with OSIRIS [22]. The red dotted line represents the critical current of $I_A/2$ (8.5 kA). For these simulations $1/(k_p r_e) = 3.6 \cdot 10^9$.

electrons originate from helium atoms. However, at the highest peak current, 34.5 kA, the electric field in the plasma is large enough to cause the ionization and subsequent trapping of the electrons from the second ionization lithium. Thus, the corresponding trapped electron bunch consists partially of electrons from lithium. Note, however, a peak current of 34.5 kA is outside of the experimental range.

An additional set of three-dimensional simulations provides support to the requirements on the drive bunch charge to initiate electron trapping. These simulations have the same plasma and grid size setup as the previous set, but a different variation of the drive bunch. This set of simulations uses Gaussian drive bunches with $I_d = I_A$, matched transverse sizes of $\sigma_{x,y} = 1.74$ μm, and $N_d = 1/(k_p r_e)$, $2/(k_p r_e)$, $3/(k_p r_e)$, $4/(k_p r_e)$, and $5/(k_p r_e)$. Similarly, these simulations run until the trapped electrons load the wake and turn off further trapping. Figure 2.6 shows how the amount of trapped electrons in the first bubble depends on the drive bunch charge. At a drive bunch charge of N_{crit} there is not a significant amount of trapped electrons, but the trapped charge rapidly increases for N_d above N_{crit}.

2.5 Field Ionization

Plasma electron trapping requires that $\Psi_m > mc^2/e + \Psi_f$. This, however, is not enough to create trapping; a trapped electron must escape its atom with $\Psi_i >$

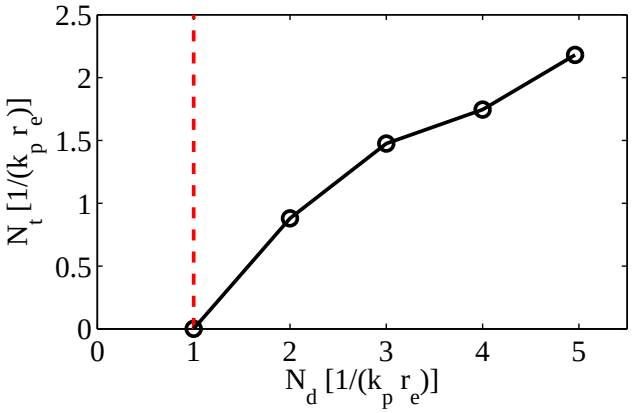

Figure 2.6: The number of trapped electrons, N_t, versus the number of drive bunch electrons, N_d, calculated with OSIRIS [22]. The red dotted line represents the critical number of drive bunch electrons ($1/(k_p r_e)$), which is $3.6 \cdot 10^9$ for these simulations.

$mc^2/e + \Psi_f$. Thus, an overview of ionization is required to further understand electron trapping. The electric field of the drive bunch is large enough to cause an electron to tunnel out from the potential well of its atom. Ammosov, Delone, and Krainov (ADK) developed an ionization rate formula for tunnel ionization [1]. An adaptation of their formula [14] is appropriate for this experiment [57]:

$$\Gamma = A \cdot E^{-B} \cdot \exp(\frac{-D}{E}), \tag{2.19}$$

$$B = 2n^* - 1, \tag{2.20}$$

$$n^* \approx \frac{3.69Z}{\sqrt{I}}, \tag{2.21}$$

$$A[\frac{(GV/m)^B}{s}] = 1.52 \cdot 10^{15} \frac{4^{n^*} I}{n^* G(2n^*)} (20.5 I^{3/2})^B, \tag{2.22}$$

$$D[GV/m] = 6.83 I^{3/2}, \tag{2.23}$$

where Γ is the ionization rate, I is the atomic ionization energy in units of eV, E is the magnitude of the applied electric field, Z is the charge residue of the atom (1 for single ionization, 2 for double, ...), and G is the Gamma function.

Equation 2.19 properly represents the ionization rate due to tunnel ionization. Above a critical electric field, E_{crit}, barrier suppression becomes the dominant term for the ionization rate [14,6]; thus, Eq. 2.19 is not appropriate for electric fields above

E_{crit}:

$$E_{crit}[GV/m] = 1.5I^{3/2}. \tag{2.24}$$

The critical field for the ionizations that are of interest to this experiment are 18.8 GV/m for Li, 987 GV/m for Li^+, 2.03 TV/m for Li^{++}, 183 GV/m for He, and 602 GV/m for He^+ [14].

The critical field for the first ionization of lithium, 18.8 GV/m, is less than the maximum electric field achieved in the experiment. However, this does not mean that the ionization formula is invalid for the experiment. If the electric field rises slowly, then atoms ionize before they reach the critical field. The ADK formula is only invalid when the electric field rises fast enough that atoms are not ionized before reaching E_{crit}. Let $\dot{E}_{crit}$ denote the rate of field increase which corresponds to ionization at a field equal to E_{crit}.

A quantification of $\dot{E}_{crit}$ is now necessary to understand the range of applicability for the ADK ionization formula. Let the applied electric field increase linearly in time: $E(t) = \dot{E}t$. The probability of an atom becoming ionized, P, is

$$P = 1 - \exp(-\int \Gamma dt). \tag{2.25}$$

Under a linearly increasing electric field, the ionization probability becomes

$$P(t) = 1 - \exp(-\int_0^t A \cdot (\dot{E}t')^{-B} \cdot \exp(\frac{-D}{\dot{E}t'})dt'). \tag{2.26}$$

As this probability never fully reaches 1, a more natural choice to denote ionization is $P = 0.5$. Let $P(t_i) = 0.5$, then the electric field that the atom becomes ionized at is $E_i = \dot{E}t_i$. The constants in the ADK formula, A, B, and D, are entirely determined by I and Z. Thus, E_i is a function of I, Z, and $\dot{E}$. Figure 2.7 shows the solution of E_i over a range of $\dot{E}$ for the first ionization level of helium. The value of $\dot{E}_{crit}$ for the ionizations of interest to this experiment are $3.82 \cdot 10^{26}$, $7.96 \cdot 10^{27}$, $5.85 \cdot 10^{28}$, $2.72 \cdot 10^{26}$, and $7.71 \cdot 10^{27}$ V/(m·s) for Li, Li^+, Li^{++}, He, and He^+, respectively.

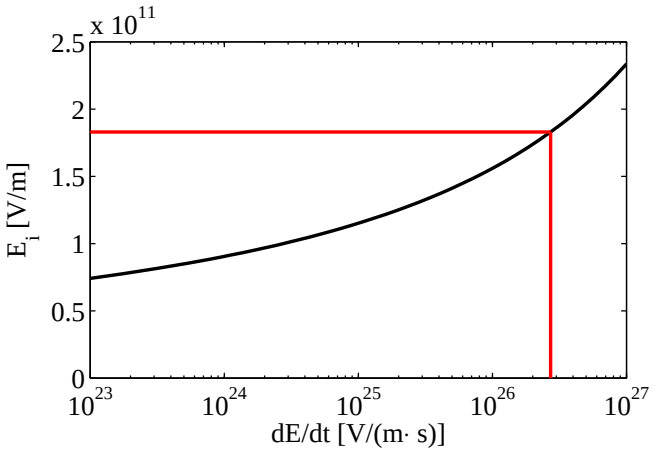

Figure 2.7: The electric field corresponding to ionization, E_i, versus $\dot{E}$ for the first ionization level of helium. The red lines denote the location of E_{crit} and the corresponding value $\dot{E}_{crit}$.

2.5.1 Densities Applicable for the ADK Formula

There is now an investigation of the plasma densities that are applicable for the ADK formula. The scale for the electric field from the plasma is $mc\omega_p/e$. This field multiplied by the plasma frequency, $mc\omega_p^2/e$, is a basic scale for the rate of field increase. The density at which the plasma field reaches E_{crit}, $n_{p,Ecrit}$, is

$$n_{p,Ecrit} = \frac{\epsilon_0 E_{crit}^2}{mc^2}. \tag{2.27}$$

These densities are $3.82 \cdot 10^{22}$, $1.05 \cdot 10^{26}$, $4.47 \cdot 10^{26}$, $3.62 \cdot 10^{24}$, and $3.92 \cdot 10^{25}$ m^{-3} for Li, Li$^+$, Li^{++}, He, and He$^+$, respectively. The density at which the rate of electric field increase reaches $\dot{E}_{crit}$, $n_{p,\dot{E}crit}$, is

$$n_{p,\dot{E}crit} = \frac{\epsilon_0 \dot{E}_{crit}}{ec}. \tag{2.28}$$

These densities are $7.04 \cdot 10^{25}$, $1.47 \cdot 10^{27}$, $1.08 \cdot 10^{28}$, $5.01 \cdot 10^{25}$, and $1.42 \cdot 10^{27}$ m^{-3} for Li, Li$^+$, Li^{++}, He, and He$^+$, respectively. The ADK formula is valid for $E < E_{crit}$ or $\dot{E} < \dot{E}_{crit}$; this is satisfied for densities below $n_{p,\dot{E}crit}$. Above these densities, the ADK formula underestimates the ionization rate.

2.5.2 Drive Bunches Applicable for the ADK Formula

The electric field of the system also includes that from the drive bunch. Thus, there is also a range of applicability for the ADK formula based on the drive bunch. Let a Gaussian charge density represent the drive bunch:

$$\rho_{bunch} = \frac{-Ne}{(2\pi)^{3/2}\sigma_x^2\sigma_z}\exp(\frac{-r^2}{2\sigma_x^2})\exp(\frac{-z^2}{2\sigma_z^2}). \tag{2.29}$$

The radial electric field from this bunch is maximized radially at $r = \alpha\sigma_x \approx 1.59\sigma_x$, where the field is

$$E_r = \frac{-Ne}{(2\pi)^{3/2}\alpha\sigma_x\sigma_z\epsilon_0}\exp(\frac{-z^2}{2\sigma_z^2})[1-\exp(\frac{-\alpha^2}{2})]. \tag{2.30}$$

Also, the radial electric field is maximized longitudinally at $z = 0$, yielding a maximum electric field of

$$E_{r,max} = \frac{-Ne}{(2\pi)^{3/2}\alpha\sigma_x\sigma_z\epsilon_0}[1-\exp(\frac{-\alpha^2}{2})]. \tag{2.31}$$

The quantity $E_{r,max}$ reaches E_{crit} for $N/(\sigma_x\sigma_z) = 3.62\cdot10^{19}$, $1.90\cdot10^{21}$, $3.92\cdot10^{21}$, $3.53\cdot10^{20}$, and $1.16\cdot10^{21}$ m^{-2}, for Li, Li$^+$, Li^{++}, He, and He$^+$, respectively. A z derivative of Eq. 2.30 multiplied by c is the rate of change in E_r at $r = \alpha\sigma_x$. This rate is maximized at $z = \sigma_z$, where the rate is

$$\dot{E}_{r,max} = \frac{Nec}{(2\pi)^{3/2}\alpha\sigma_x\sigma_z^2\epsilon_0}\exp(\frac{-1}{2})[1-\exp(\frac{-\alpha^2}{2})]. \tag{2.32}$$

The quantity $\dot{E}_{r,max}$ reaches $\dot{E}_{crit}$ at $N/(\sigma_x\sigma_z^2) = 4.05\cdot10^{27}$, $8.44\cdot10^{28}$, $6.21\cdot10^{29}$, $2.88\cdot10^{27}$, and $8.17\cdot10^{28}$ m^{-3}, for Li, Li$^+$, Li^{++}, He, and He$^+$, respectively. For the ADK ionization formalism to be invalid, it must have both $N/(\sigma_x\sigma_z)$ and $N/(\sigma_x\sigma_z^2)$ above these critical values.

2.6 Ionization Induced Electron Trapping

As was discussed earlier in this chapter, electron trapping occurs due to the simultaneous presence of both helium and lithium vapor in the heat-pipe oven. Lithium electrons support the plasma wake, while the higher ionization potential of helium allows its electrons to become trapped. The ADK ionization formalism, presented in the previous sections, is now used for a quantitative examination of ionization induced electron trapping.

Recall the simulation shown in Figs. 2.2, 2.1, and 1.1. The parameters of this simulation are typical for the experiment. In reference to the previous sections, the plasma density of $2.7 \cdot 10^{23}$ m^{-3} and the simulation bunch value of $N/(\sigma_x \sigma_z^2) = 2.59 \cdot 10^{25}$ m^{-3} are both well within the range of applicability for the ADK formula. Thus, this formula can be applied to electron trapping in the experiment.

Figure 2.8 shows the magnitude of the electric field for the simulation displayed in Figs. 2.2, 2.1, and 1.1, along with a few radial positions of interest for the simulation. These radial positions correspond to $r = 0$, $1.59\sigma_x$, and $4\sigma_x$. From the magnitude of the electric field, P for the first ionization level of helium can be calculated along $z - ct$. The negative of a $(z - ct)$ derivative of P yields the range in $z - ct$ over which helium is ionized. Figure 2.9 displays the distribution of the ionization locations for the three radial positions.

In the simulation, Ψ_f = -0.33 mc^2/e. The absolute value of a Ψ derivative of P yields the probability distribution of Ψ_i for the atoms at the three radial positions, which is shown in Fig. 2.10. An integration of this distribution for Ψ_i greater than $\Psi_f + mc^2/e$ yields the total probability that an electron from that radial position would be trapped. For this specific simulation, the helium electrons at $r = 0$, $1.59\sigma_x$, and $4\sigma_x$ have a probability of 0.09, 0.00, and 0.78 of becoming trapped. The atoms at $r = 1.59\sigma_x$ experience the maximum radial electric field from the drive bunch and are ionized very quickly, before they reach $\Psi > \Psi_f + mc^2/e$. In contrast, lithium atoms at all of these radial positions become ionized too quickly to create trapping: the Ψ_i distribution for lithium is effectively a delta function centered about $\Psi_i = 0$.

This type of analysis is useful for finding the location and probability of electron trapping. However, there is no analytic solution to the electric fields in a PWFA, so

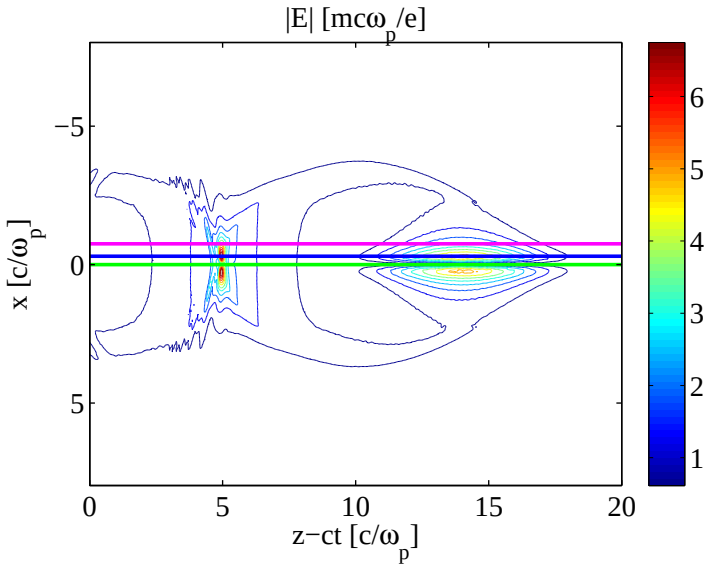

Figure 2.8: A contour plot for the magnitude of the electric field in a plasma wake, calculated with OSIRIS. In this simulation, the drive bunch had $1.8 \cdot 10^{10}$ electrons, $\sigma_x = \sigma_y = 1.74$ μm, $\sigma_z = 20$ μm, and drove a wake in a plasma of density $n_p = 2.7{\cdot}10^{23}$ m^{-3} ($mc\omega_p/e = 50$ GV/m, and $c/\omega_p = 10$ μm). The green, blue, and magenta lines correspond to $x = 0$, $1.59\sigma_x$, and $4\sigma_x$, respectively.

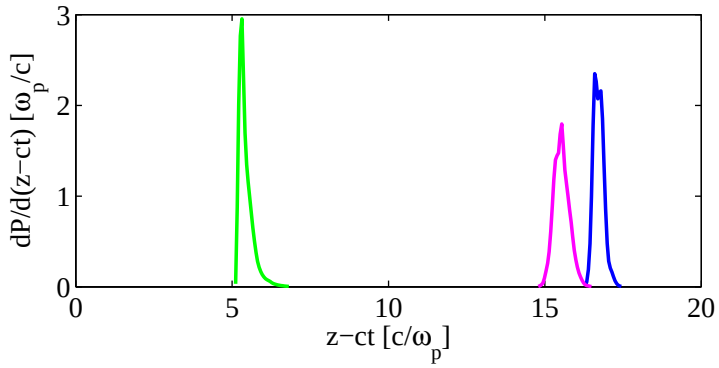

Figure 2.9: The position of ionization in a plasma wake, calculated from the output of an OSIRIS simulation. In this simulation, the drive bunch had $1.8 \cdot 10^{10}$ electrons, $\sigma_x = \sigma_y = 1.74$ μm, $\sigma_z = 20$ μm, and drove a wake in a plasma of density $n_p = 2.7{\cdot}10^{23}$ m^{-3} ($c/\omega_p = 10$ μm). The green, blue, and magenta lines correspond to $x = 0$, $1.59\sigma_x$, and $4\sigma_x$, respectively. For all of these positions the total probability of ionization is 100%, so the integrals under the curves are 1.

this approach must be combined with simulation results. When detailed information is not required, simpler methods can be used to explore the onset of trapping for

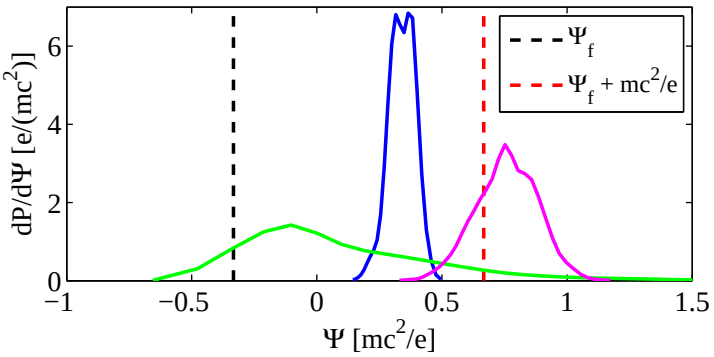

Figure 2.10: The probability distribution of Ψ_i for helium in a plasma wake, calculated from the output of an OSIRIS simulation. In this simulation, the drive bunch had $1.8 \cdot 10^{10}$ electrons, $\sigma_x = \sigma_y = 1.74$ μm, $\sigma_z = 20$ μm, and drove a wake in a plasma of density $n_p = 2.7 \cdot 10^{23}$ m^{-3} ($c/\omega_p = 10$ μm). The green, blue, and magenta lines correspond to $x = 0$, $1.59\sigma_x$, and $4\sigma_x$, respectively. For all of these positions the total probability of ionization is 100%, so the integrals under the curves are 1.

different gas species and ionization levels. For example, simulations show that the electrons from the first ionization of lithium can not become trapped. This conclusion can be reached without the use of a simulation. Consider the atoms on the bunch axis. Since E_z is independent of r inside the bubble, the minimum $|E|$, and therefore also ionization rate, occurs on axis (where $E_r = 0$). If the on-axis atoms become ionized before reaching $\Psi = \Psi_f + mc^2/e$, the atoms with a finite r will also be ionized before $\Psi_f + mc^2/e$. Thus, the electrons from these atoms will not become trapped. The formalism for E_i, shown in Sec. 2.5, can be applied to the on-axis atoms to test whether they are ionized too quickly for electron trapping to occur.

Under the approximation of a linear increasing electric field in time, a solution of Ψ_i for the on-axis electrons can be found. The quantity $\Psi = 0$ in front of the wake. Let the position of $z - ct = 0$ correspond to $\Psi = 0$. The linearly increasing field in time then has the following dependence on $z - ct$ for $z < ct$.

$$E = (t - z/c)\dot{E}. \tag{2.33}$$

Recall, $\partial_z \Psi = -E_z$. The only electric field on the axis is E_z, so $E_i = E_z$ when the

atom is ionized. Thus,

$$\Psi_i = \frac{cE_i t_i}{2}. \tag{2.34}$$

The quantity $E_i/\dot{E}$ can replace the time for ionization, t_i, which yields

$$\Psi_i = \frac{cE_i^2}{2\dot{E}}. \tag{2.35}$$

Since E_i is only a function of I, Z, and $\dot{E}$, then Ψ_i is also only a function of I, Z, and $\dot{E}$. The quantity Ψ_f can extend below zero, but for simplicity it can be assumed as zero. Under this assumption, the trapping condition becomes

$$\Psi_i = \frac{cE_i^2}{2\dot{E}} > \frac{mc^2}{e}. \tag{2.36}$$

Recall from Fig. 2.7 that E_i is only very weakly dependent on $\dot{E}$. In this figure, E_i only increases by a factor of three as $\dot{E}$ varies over four orders of magnitude. Thus, the dependency of Ψ_i on $\dot{E}$ is dominated by the direct relationship shown in the above equation, rather than through E_i. For each species of ionization (I and Z) there is a critical value of $\dot{E}$, $\dot{E}_{trap}$, where $\Psi_i = mc^2/e$. As $\dot{E}$ increases Ψ_i decreases. Therefore, for $\dot{E}$ above $\dot{E}_{trap}$ ionization induced trapping of the species turns off. Figure 2.11 displays Ψ_i for the first ionization level of lithium as a function of $\dot{E}$ and the corresponding value for $\dot{E}_{trap}$. The values of $\dot{E}_{trap}$ for the ionizations that are of interest to this experiment are $9.04 \cdot 10^{21}$, $8.39 \cdot 10^{25}$, $2.96 \cdot 10^{26}$, $2.97 \cdot 10^{24}$, and $2.35 \cdot 10^{25}$ V/(m·s) for Li, Li^+, Li^{++}, He, and He^+, respectively.

An assumption of $mc\omega_p^2/e$ for the scale of $\dot{E}$ turns the values of $\dot{E}_{trap}$ into plasma densities, above which ionization induced trapping does not occur. For Li, Li^+, Li^{++}, He, and He^+ the plasma densities that correspond to $\dot{E}_{trap}$ are $1.67{\cdot}10^{21}$ m^{-3}, $1.55{\cdot}10^{25}$ m^{-3}, $5.45{\cdot}10^{25}$ m^{-3}, $5.48{\cdot}10^{23}$ m^{-3}, and $4.34{\cdot}10^{24}$ m^{-3}, respectively. However, $mc\omega_p^2/e$ only represents the scale for $\dot{E}$, so these densities are only rough estimates of where trapping of these species would cease. For example, consider E_z as displayed by Fig. 1.2. At the front of the wake, E_z increases by $(1/2)mc\omega_p/e$ in a time of $3/\omega_p$. Thus, $\dot{E} = (1/6)mc\omega_p^2/e$. Since $\omega_p^2 \propto n_p$, trapping for this wake would cease at a plasma density that is six times higher than that suggested by setting $\dot{E} = mc\omega_p^2/e$.

Most of the experiments occurred at $n_p = 2.7 \cdot 10^{23}$ m^{-3}. This density is more

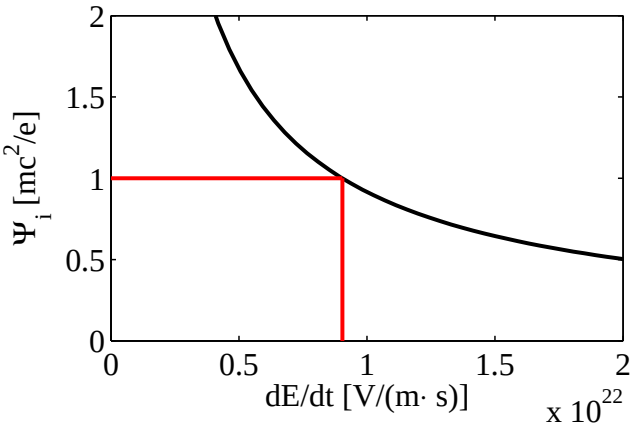

Figure 2.11: The Ψ of ionization, Ψ_i, versus $\dot{E}$ for the first ionization level of lithium. The red lines denote the location of $\Psi_i = mc^2/e$ and the corresponding value of $\dot{E}$ ($\dot{E}_{trap}$).

than two orders of magnitude above the scale at which trapping ceases for the first ionization level of lithium, $1.67 \cdot 10^{21}$ m^{-3}. Thus, the electrons from the first ionization of lithium were not trapped in the experiments presented in this dissertation.

2.7 Termination of Trapped Electrons

As discussed in Sec. 1.5.1, plasma electron trapping can degrade the strength of the accelerating field, which would hinder the ability to accelerate a witness bunch in the plasma wake. Consider, for example, the effect of electron trapping on the loading simulation displayed in Fig. 1.12. This simulation was repeated in two-dimensional OSIRIS to test the effect of electron trapping on the loaded wake. Figure 2.12 displays the effect that trapping has on the accelerating field. The trapped electrons severely load the wake near the core of the witness bunch, which would result in a large energy spread for the witness bunch. Such an energy spread would be unacceptable for a high energy collider.

The preceding sections covered the requirements to induce plasma electron trapping. This information is now used for a discussion of methods to terminate trapping. Electron trapping is caused by a combination of driving a strong wakefield ($R > 2/k_p$ with $v_r \approx c$) and having atoms ionized inside the plasma bubble. Therefore, trapping

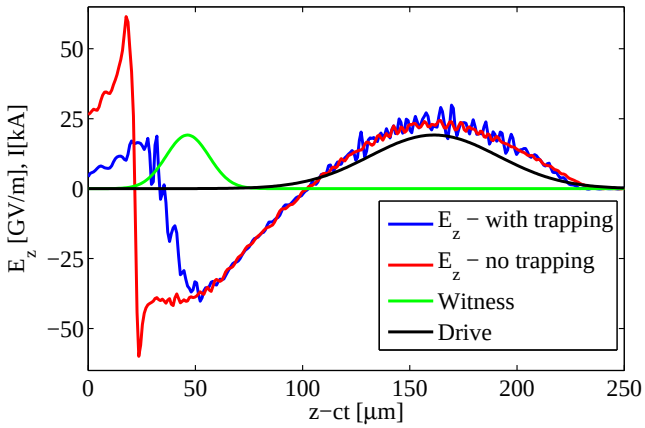

Figure 2.12: The effect of trapped electrons on the accelerating field of a plasma wake, calculated with OSIRIS. The drive bunch had $3 \cdot 10^{10}$ electrons with $\sigma_z = 30$ μm, and the witness bunch had 10^{10} electrons with $\sigma_z = 10$ μm; both bunches had $\sigma_x = \sigma_y = 3$ μm ($\epsilon_{N,x} = \epsilon_{N,y} = 84$ μm) and $\gamma = 48,924$. These bunches were separated by 115 μm. The simulation "with trapping" had a lithium density of 10^{23} m^{-3} and a helium density of 10^{22} m^{-3}. The simulation with "no trapping" only included lithium at a density of 10^{23} m^{-3}.

can be controlled by either producing weak wakefields or restricting the position of atom ionization.

2.7.1 Weak Plasma Wakes

The theory and simulations in this chapter show that when either $I_d < I_A/2$ or $N_d < 1/(k_p r_e)$ electron trapping no longer occurs. Thus, reducing either of these bunch parameters below the critical values is a trivial physics fix for the trapping of plasma electrons. However, the question is not just whether trapping can be terminated. There is an additional constraint that the wake must retain reasonable accelerating properties. Recall the simulations discussed in Sec. 1.5.6. This set of simulations was repeated with the peak current in both the drive and witness bunch at $I_A/2$ and then again at $I_A/4$. Figure 2.13 displays the achieved transformer ratios, energy spreads, and efficiencies from the simulations of Sec. 1.5.6 and those with a reduced peak current. The low current simulations achieved similar values to that of the original set of simulations. However, the witness bunch experiences a decreased

accelerating field for the low current simulations. At the minimum energy spread, the accelerating field for the witness bunch was 33, 18, and 8.8 GV/m for the peak currents of 1.12, 0.5, and 0.25 I_A, respectively. Even at the lowest current, the accelerating field is still orders of magnitude larger than it is for conventional technologies. Thus, this is a viable method to terminate trapping.

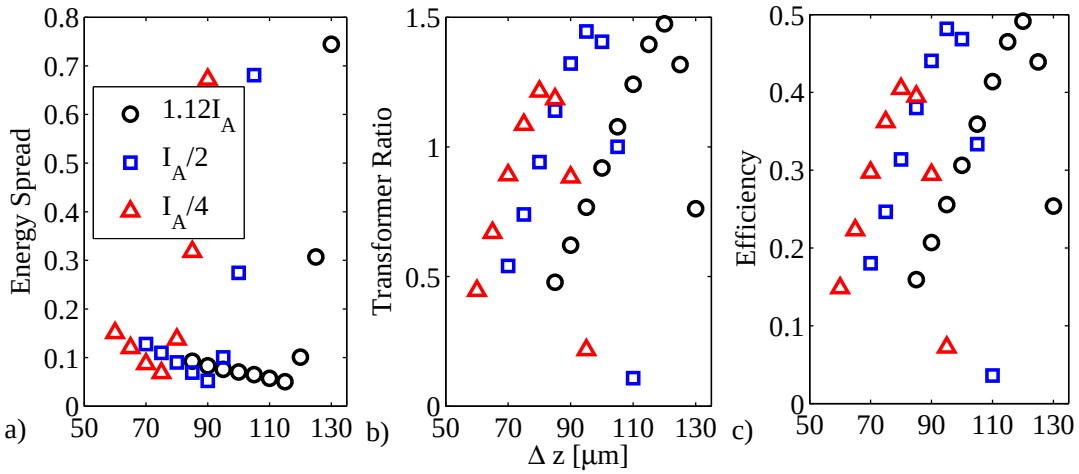

Figure 2.13: The a) relative rms energy spread, b) transformer ratio, and c) efficiency calculated in a set of QuickPIC simulations, which varied the distance between the drive and the witness bunch, Δz. The drive bunch had $\sigma_z = 30$ μm, and the witness bunch had $\sigma_z = 10$ μm; both bunches had $\sigma_x = \sigma_y = 3$ μm ($\epsilon_{N,x} = \epsilon_{N,y} = 84$ μm) and $\gamma = 48,924$. These bunches drove a wake in a pure lithium vapor of density 10^{23} m^{-3}. The black circles, blue squares, and red triangles correspond to drive and witness bunch peak currents of $1.12{\cdot}I_A$, $I_A/2$, and $I_A/4$, respectively.

2.7.2 Control of Ionization Location

As shown earlier in this chapter, electrons can become trapped by being released from their atoms inside the plasma bubble. To cease the trapping of plasma electrons in strong wakes, all atomic species and levels must be ionized very quickly, before reaching $\Psi = mc^2/e$, or not at all. A trivial physics fix to this problem would be to completely pre-ionize the vapor. This is, however, a nontrivial engineering feat, so the remainder of this section is devoted to the termination of electron trapping in a self-ionized PWFA.

In the experiment, electron trapping occurred due to the presence of both helium and lithium. The lithium electrons supported the wake in which the helium electrons became trapped. If the helium atoms were removed from the plasma, electron trapping would have stopped. However, this would not also be true for a plasma-based collider. Future linear colliders require incredibly small transverse emittances for the electron bunches. For example, current concepts of a PWFA-based linear collider indicate required emittances of $\epsilon_{N,x} = 2$ μm and $\epsilon_{N,y} = 50$ nm [63]. These emittances yield small transverse bunch sizes and large transverse electric fields. This can result in trapping from a single gas species: a lower ionization level supports the wake, while a higher level becomes trapped. As an example, the matched transverse sizes for the suggested emittances at $n_p = 10^{23}$ m^{-3} for a 500 GeV electron bunch are $\sigma_x = 219$ nm and $\sigma_y = 34.7$ nm. The peak transverse electric field of an electron bunch with these transverse sizes and a peak current of I_A is 4.40 TV/m, which is more than enough to multiply ionize any element. Near the peak field position of the bunch, atoms would become ionized very quickly, before reaching a significant Ψ. However, the ionization probability decreases to zero at larger radii. Between these two regions is a radial range where trapping can occur. For this reason, gases with multiple ionization levels create trapping problems for PWFA-based colliders.

The use of hydrogen vapor in a PWFA would not produce multiple ionizations, but does have its own complications. Its 13.6 eV ionization potential causes ionization problems at large radii. This constrains the peak current of the drive bunch and the plasma density. To illustrate this problem, Fig. 2.14 displays the ionization probability from the electric field of an electron drive bunch with $I_d = I_A$ and $\sigma_z = 30$ μm as a function of radius from the bunch axis. The ionization probability begins to roll off between $r = 30$ and 40 μm. Ideally, the radial range of ionization should be much greater than the maximum radius of the ion bubble, R_m. Otherwise, electrons in the sheath are expelled past the radial range of the ions in the bubble. As they pass outside of the ions, the ion restoring force changes from being proportional to being inversely proportional with radius. When the restoring force is proportional to r, the oscillation times for all of the sheath electrons are roughly the same, so they act as a coherent sheath. This is no longer true when the electron's restoring force is inversely proportional to r. The electrons return to the bunch axis at different times.

Since E_z is related to the radial current, this destroys the strength of the accelerating field in the back of the wake. Thus, it is important for the radial range of ionization to far exceed R_m.

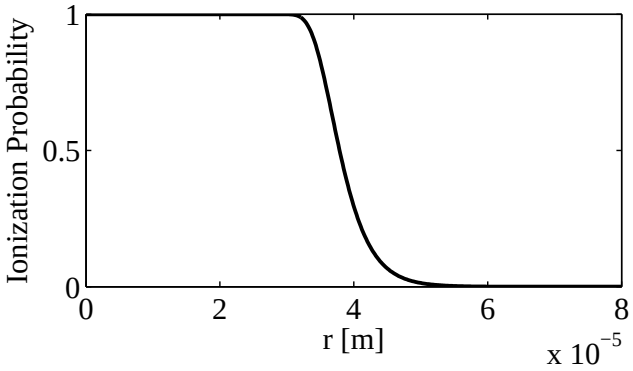

Figure 2.14: The ionization probability of hydrogen from the electric field of an electron drive bunch with $I_d = I_A$ and $\sigma_z = 30$ μm as a function of radius from the bunch axis (assuming $\sigma_x = \sigma_y = 0$).

Most current concepts for a PWFA-based collider have a plasma density of 10^{23} m^{-3}, where $1/k_p = 16.8$ μm. From Eq. 2.18, a drive bunch with $I_d = I_A$ at this density creates a wake with $R_m = 48$ μm, which is larger than the radial range of hydrogen ionization. Thus, these parameters can not be used in a self-ionized hydrogen PWFA. To make a viable PWFA, the parameters can be changed in one of two ways: the use of higher density plasma or higher peak current drive bunches. At higher plasma densities R_m decreases (see Eq. 2.18), while the radial range of ionization remains roughly the same. Also, the radial range of ionization is proportional to I_d, but R_m is only proportional to square root of I_d. As the peak current increases, the radial ionization range eventually exceeds R_m.

A set of two-dimensional OSIRIS simulations tested the accelerating wake for several values of drive bunch peak current in a hydrogen plasma. The drive bunches had $\sigma_z = 30$ μm, $\sigma_x = \sigma_y = 3$ μm ($\epsilon_{N,x} = \epsilon_{N,y} = 84$ μm), $\gamma = 48,924$, and $I_d =$ 1.12, 2, 4, and 8 I_A. These bunches drove a plasma wake in a pure hydrogen vapor of density 10^{23} m^{-3}. In r and z the simulation grid size was 0.5 μm with 9 particles per cell. Figure 2.15 shows the resulting accelerating field for the different drive bunch peak currents. There is not a significant accelerating phase of the wake for $I_d = 1.12$

I_A, but at $I_d = 4\ I_A$ one is completely formed.

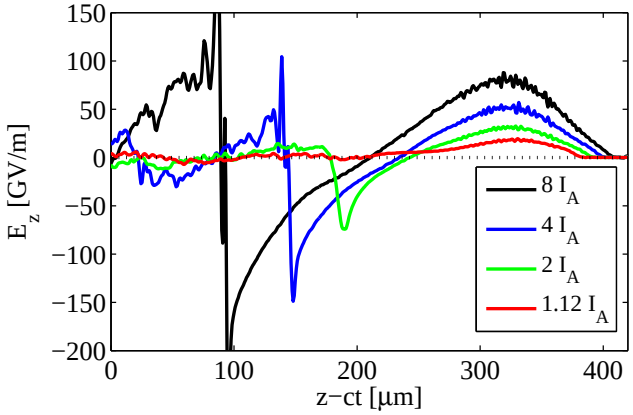

Figure 2.15: The on-axis E_z versus $z-ct$ in a field-ionized hydrogen plasma for several values of drive bunch peak current ($I_A \approx 17$ kA).

An additional set of two-dimensional OSIRIS simulations explored the accelerating wake produced by scaling the drive bunch to higher plasma density. The drive bunches had $\sigma_z = 1.79/k_p$, $\sigma_x = \sigma_y = 0.179/k_p$, $\gamma = 48,924$, and $I_d = 1.12\ I_A$. These drive bunches drove a plasma wake in pure hydrogen vapor with the densities of 10^{23} m^{-3}, $2 \cdot 10^{23}$ m^{-3}, $4 \cdot 10^{23}$ m^{-3}, and $8 \cdot 10^{23}$ m^{-3}. In r and z the simulation grid size was $0.05/k_p$ with 9 particles per cell. Figure 2.16 displays the resulting accelerating field for the different plasma densities. There is not a significant accelerating phase of the wake for $n_p = 10^{23}$ m^{-3}, but at $n_p = 4 \cdot 10^{23}$ m^{-3} one is almost completely formed.

2.7.3 Termination Conclusions

In conclusion, plasma electron trapping can be terminated by one of three methods. First, complete pre-ionization of the plasma, is a trivial physics fix, but a nontrivial engineering feat. Next, a self-ionized hydrogen PWFA, under the right drive bunch and plasma density configuration, is also able to terminate trapping. Lastly, the plasma wake could be created with a drive bunch that has a peak current below $I_A/2$ (or $N_d < 1/(k_p r_e)$). This method results in a lower accelerating field, but is still able to create energy spreads, transformer ratios, and efficiencies similar to the wakes generated at higher peak currents.

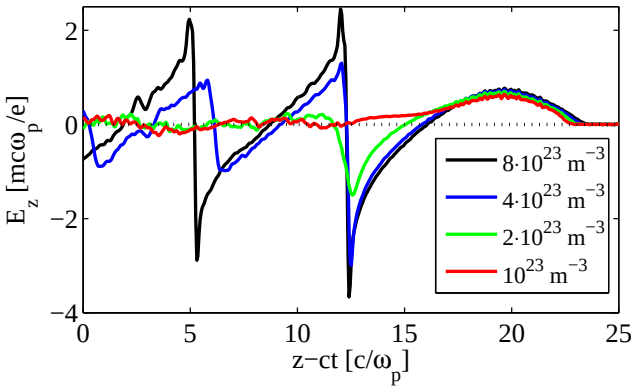

Figure 2.16: The on-axis E_z versus $z-ct$ in a field-ionized hydrogen plasma for several values of plasma density.

Chapter 3

Trapped Electron Bunch Properties

3.1 Introduction

Low emittance electron bunches have applications that include next generation light sources and particle accelerators [71]. At present, thermionic and photoemission based electron sources are widely used [25]; however, plasma based electron sources are an active topic of research due to their potential to produce high current and low emittance electron bunches [67, 23, 17, 3, 40, 44, 49, 16]. Recently it was shown that PWFAs, operated in the nonlinear bubble regime, can trap electrons that are released by ionization inside the plasma wake [58] and accelerate them to high energies. However, more than just high energy is required for an electron source. This chapter uses simple theoretical models and simulations to investigate the necessary properties of the trapped electrons as a particle source.

This chapter is organized as follows. First, there is a detailed investigation of the trapped electron transverse emittance. Next, there is a discussion of the other trapped electron bunch properties: peak current, total charge, longitudinal bunch length, and energy spread. This is then followed by a comparison of the properties for the electron bunches trapped behind the first bubble. Finally, this chapter ends with a discussion of how to develop the trapped electrons into a particle source.

3.2 Transverse Emittance

Each plasma electron has a radial position and zero momentum when it escapes its atom. The focusing fields then rotate the electrons in the $x - p_x$ (or $y - p_y$) phase space, where $x = r\cos\phi$, and θ denotes the angle in the $x - p_x$ plane. As the drive bunch propagates through the plasma and the trapped electrons rotate in this plane, the wake collects additional electrons at $\theta = 0$, resulting in a uniform distribution in θ and a finite emittance. Figure 3.1 illustrates this process. The focusing forces are linear in x, so after the phase space is filled there is no additional emittance growth. Thus, the first phase space rotation determines the transverse normalized emittance, expressed in Eq. 3.1.

$$\epsilon_{N,x} = \frac{1}{mc}\sqrt{\langle x^2\rangle\langle p_x^2\rangle - \langle xp_x\rangle^2}, \tag{3.1}$$

where $\langle x\rangle = 0$ and $\langle p_x\rangle = 0$. The strength of the focusing force determines the area in phase space filled by the trapped electrons. As the trapped electrons accelerate in the wake, the focusing force applied to them changes from E_r to $E_r - cB_\phi$. The exact trajectory of the electrons in the $x - p_x$ plane depends on the specifics of this transition. An appropriate assumption for E_z in the back of the bubble, behind the drive bunch, is $\partial_z E_z = ne/(2\epsilon_0)$ [48] (see Eq. 1.12). Gauss' law combined with this assumption implies that

$$E_r = n_p e r/(4\epsilon_0), \tag{3.2}$$

which is only a factor of 2 smaller than $E_r - cB_\phi$. Therefore, either E_r or $E_r - cB_\phi$ can be used as the focusing field to set the scale for the emittance. The electrons are accelerated by an electric field of scale $mc\omega_p/e$, and the time for the first phase space rotation is of order $1/\omega_p$. Therefore, the trapped electrons can acquire momentum that is of order mc within the first rotation. However, they do not become very relativistic, so a nonrelativistic harmonic oscillator approximates their motion. A justification for this approximation is made later in this section. The quantity $E_r\cos(\phi)$ is then the x focusing field, so the following differential equation describes the motion in the $x - p_x$ plane.

$$\frac{d^2x}{dt^2} + \frac{\omega_p^2}{4}x = 0. \tag{3.3}$$

Let the trapped electrons have an initial mean square size in x of $\langle x_0^2 \rangle$ and zero initial transverse momentum. Since $x = x_0 \cos\theta$,

$$\langle x^2 \rangle = \langle x_0^2 \rangle / 2. \tag{3.4}$$

The uniform distribution of θ yields a relationship between the sizes in x and p_x,

$$\langle p_x^2 \rangle = m^2 c^2 k_p^2 \langle x^2 \rangle / 4, \tag{3.5}$$

and that $\langle x p_x \rangle = 0$. Thus,

$$\epsilon_{N,x} = k_p \langle x_0^2 \rangle / 4. \tag{3.6}$$

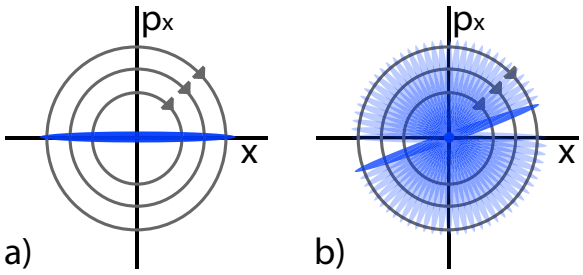

Figure 3.1: a) The initial distribution of trapped electrons in the $x - p_x$ phase space immediately following ionization. b) The distribution of trapped electrons as they rotate in the $x - p_x$ phase space and the wake collects additional trapped electrons.

Equation 3.6 represents the connection between the initial transverse size and the transverse emittance for a nonrelativistic harmonic oscillator. Since the trapped electrons can become moderately relativistic in their first oscillation, it is important to compare the nonrelativistic results to fully-relativistic simulations. As the electrons become relativistic, they are affected by the magnetic fields. A combination of Eq. 3.2 and Eq. 1.20 yields B_ϕ as

$$cB_\phi = -n_p e r / (4\epsilon_0). \tag{3.7}$$

Consider the evolution of an electron in the $x - z$ plane subject to E_r (from Eq. 3.2), B_ϕ (from Eq. 3.7), and $E_z = -\eta m c \omega_p / e$, where η is a dimensionless constant. The

following equations describe the evolution of this electron.

$$\frac{dp_x}{dt} = \frac{mc\omega_p^2 x}{4c}(1+\frac{v_z}{c}). \tag{3.8}$$

$$\frac{dp_z}{dt} = \eta mc\omega_p. \tag{3.9}$$

These equations have the following initial conditions.

$$x(0) = x_0, \quad y(0) = z(0) = 0, \quad p_x(0) = p_y(0) = p_z(0) = 0. \tag{3.10}$$

Figure 3.2 shows the integration of this differential equation for $\eta = 1$ and $x_0 = c/\omega_p$, using the fourth order Runge-Kutta method of integration. The electron's trajectory creates ellipses in phase space. As the electron accelerates, the ellipse size in x decreases and its size in p_x increases, keeping its area constant.

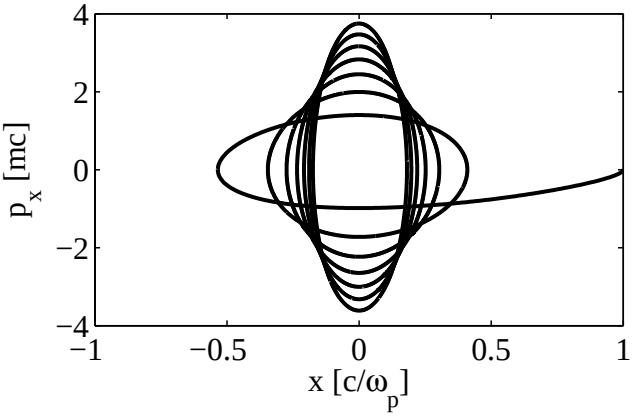

Figure 3.2: The x-p_x trajectory taken by a particle subject to Eqs. 3.8 - 3.10 with $\eta = 1$ and $x_0 = c/\omega_p$, plotted for $t = 0$ to $1000/\omega_p$.

The trajectory from the fully-relativistic simulation is now compared to the emittance predictions of Eq. 3.6. As the electron accelerates, the relative amount of change in γ during one oscillation becomes small. Thus, during a given oscillation Eq. 3.8 is simplified as

$$\frac{d^2x}{dt^2} = \frac{\omega_p^2 x}{2\gamma}. \tag{3.11}$$

This differential equation has the following solution.

$$x(t) = x_i \cos(\frac{\omega_p t}{\sqrt{2\gamma}} + \theta_i), \tag{3.12}$$

$$p_x(t) = -m\omega_p x_i \sqrt{\frac{\gamma}{2}} \sin(\frac{\omega_p t}{\sqrt{2\gamma}} + \theta_i), \tag{3.13}$$

where x_i is the amplitude of the oscillation when $p_x = 0$, and θ_i is a phase constant. The expectation values required for the determination of the emittance are

$$\langle x^2 \rangle = \frac{x_i^2}{2}, \tag{3.14}$$

$$\langle p_x^2 \rangle = \frac{\gamma m^2 \omega_p^2 x_i^2}{4}, \tag{3.15}$$

$$\langle x p_x \rangle = 0. \tag{3.16}$$

A substitution of these expectation values into Eq. 3.1 yields the emittance of this particle as

$$\epsilon_{N,x} = k_p x_i^2 \sqrt{\frac{\gamma}{8}}. \tag{3.17}$$

Each rotation yields two values of x_i. Figure 3.3 shows the evaluation of Eq. 3.17 with $x_0 = 1/k_p$ for several values of η. The corresponding value for $\epsilon_{N,x}$ from Eq. 3.6 is $1/(4k_p)$. Initially, the determined value for $\epsilon_{N,x}$ varies, but it converges as the electron becomes relativistic. For large values of η the final emittance becomes very large. At a value of $\eta = 1$, $\epsilon_{N,x} = 0.32/k_p$, but at smaller values of η, $\epsilon_{N,x}$ converges near to $1/(4k_p)$. Despite being built from a nonrelativistic formalism, Eq. 3.6 describes well the connection between initial size and emittance for values of η less than or equal to one. However, it is an underestimate for larger values of η.

The location of ionization within the wake determines $\langle x_0^2 \rangle$, with ionization occurring in regions of high electric field. Recall Fig. 2.8, which is a contour plot for the magnitude of the electric field, $|E|$, in the ion bubble (from an OSIRIS simulation). The magnitude of E_z peaks at the front and back of the bubble, and E_r peaks at the front, near the drive bunch. This causes atoms to be ionized either in the front or the back of the bubble, as displayed in Fig. 2.9. An electron that escapes its atom in the front, near the drive bunch, does so in a large defocusing field (from the drive bunch),

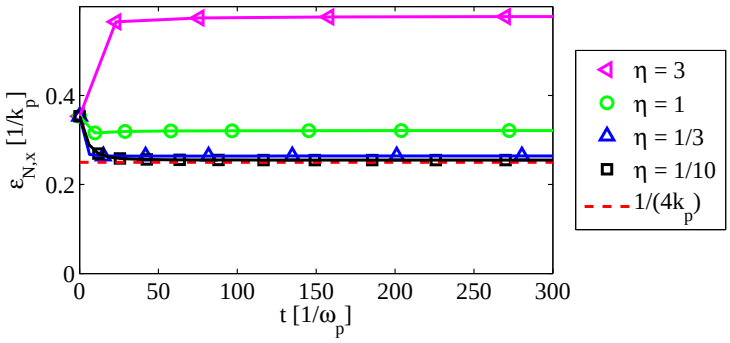

Figure 3.3: The evolution of the transverse emittance for several values of η, where $x_0 = 1/k_p$.

and one that escapes in the back of the ion bubble is initially in a large focusing field. This difference in initial focusing conditions results in the need to calculate the initial size of the electrons from the two regions in a different way.

First, consider the electrons released from their atoms in the front of the bubble. Electron trapping only occurs if R exceeds $2/k_p$ (see Sec. 2.4), so the drive bunch expels the trapped electrons that are released by ionization near it to similar radial distances. After the drive bunch passes, these electrons only experience the focusing force of the ion bubble. Thus, the radial distance to which the electrons are expelled determines their initial size. This sets a minimum scale for the initial size as

$$\langle x_0^2 \rangle \approx 1/k_p^2, \tag{3.18}$$

which yields a scale for the minimum achievable emittance of trapped electrons that escape their atoms near the drive bunch:

$$\epsilon_{N,x} = \frac{1}{4k_p}. \tag{3.19}$$

Analysis of $\langle x_0^2 \rangle$ for the electrons that are released from their atoms in the back of the bubble is more detailed and requires an understanding of the field ionization process. The quantity Ψ_i controls whether a particle becomes trapped and its final τ location in the bubble. Therefore, any longitudinal location in a trapped electron bunch consists of electrons that were ionized along a Ψ contour. Recall Fig. 2.2,

electrons released along the $\Psi_f + mc^2/e$ contour eventual gather at the Ψ_f contour on axis, despite being from different initial τ locations. Thus, the initial size of electrons released in back of the bubble results from the transverse size of the ionization rate along a Ψ contour.

The transverse size along a Ψ contour also has a minimum scale. To find this scale, first consider the mathematical condition for a Ψ contour, where Ψ is only a function of τ and r.

$$d\Psi = \frac{\partial \Psi}{\partial \tau} d\tau + \frac{\partial \Psi}{\partial r} dr = 0. \tag{3.20}$$

This condition yields a differential equation for $\tau(r)$ along the contour:

$$\frac{d\tau}{dr} = -\frac{\partial \Psi}{\partial r} / (\frac{\partial \Psi}{\partial \tau}). \tag{3.21}$$

Recall the relationships for the partial derivates of Ψ (Eqs. 2.10 and 2.11). Equation 1.20 shows that $E_r - cB_\phi = n_p e r/(2\epsilon_0)$, and the following equation is an appropriate representation for E_z in the back of the ion bubble (see Eq. 1.12).

$$E_z = \frac{n_p e(\tau - \tau_0)}{2\epsilon_0}, \tag{3.22}$$

where τ_0 denotes the point where $E_z = 0$. Thus,

$$\frac{d\tau}{dr} = \frac{r}{\tau_0 - \tau}. \tag{3.23}$$

Let $\tau(0) = \tau_a$, which yields the following solution for $\tau(r)$ along a Ψ contour in the back of the ion bubble.

$$\tau(r) = \tau_0 - \sqrt{(\tau_0 - \tau_a)^2 - r^2}. \tag{3.24}$$

This Ψ contour reaches its maximum radius of $\tau_0 - \tau_a$ in the middle of the bubble, where $\tau = \tau_0$. A substitution of the solution for $\tau(r)$ into the Eq. 3.22 yields $E_z(r)$ along a Ψ contour. A combination of this with Eq. 3.2 yields the magnitude of the

electric field as a function of r along a Ψ contour:

$$\begin{aligned} |E| &= \sqrt{E_z^2 + E_r^2}, \\ &= \frac{n_p e}{2\epsilon_0}\sqrt{(\tau - \tau_0)^2 + \frac{r^2}{4}}, \\ &= \frac{n_p e}{2\epsilon_0}\sqrt{(\tau_0 - \tau_a)^2 - \frac{3r^2}{4}}. \end{aligned} \tag{3.25}$$

This equation indicates that the scale for the falloff of $|E|$ in r is set by $\tau_0 - \tau_a$.

The scale for $\tau_0 - \tau_a$ can not be arbitrarily small. For an electron to be released from its atoms in the back of the bubble, it must be true that it was not released in the front, where electric fields are of order $mc\omega_p/e$. An atom that is ionized with electric fields significantly below $mc\omega_p/e$ would become ionized in the front of the bubble. Therefore, to ionize atoms in the back of the bubble, the accelerating field in the back must at least be on the scale of $mc\omega_p/e$. From Eq. 3.22, $\tau_0 - \tau_a$ must be $2/k_p$ to have $E_z = mc\omega_p/e$. Inserting $\tau_0 - \tau_a = 2/k_p$ into Eq. 3.25 yields

$$|E| = \frac{mc\omega_p}{e}\sqrt{1 - \frac{3r^2k_p^2}{16}}. \tag{3.26}$$

Figure 3.4 displays $|E|$ from this equation as a function of r (denoted by E_0). The Ψ contour corresponding to E_0 has a maximum radial extent of $2/k_p$. At positions farther back in the bubble this radial extent increases.

In addition to the requirements on $|E|$ to induce trapping of the electrons released in the back of the bubble, there are also requirements from the ionization rate. The time scale for the ion bubble is $1/\omega_p$, so the ionization rate must be on the order of ω_p to cause ionization inside the bubble. Consider the parameters relevant to the experiment. At a plasma density of $2.7{\cdot}10^{23}$ m^{-3} the ionization rate of helium created by E_0 is too small for electrons to be released along its corresponding Ψ contour ($\Gamma(E_0) < \omega_p/470$). At this density the ionization rate equals ω_p on axis for the Ψ contour with $\tau_0 - \tau_a = 3.244/k_p$. Along this contour, the magnitude of the electric field as a function of r is

$$|E| = \frac{mc\omega_p}{e}\sqrt{\frac{3.244^2}{4} - \frac{3r^2k_p^2}{16}}. \tag{3.27}$$

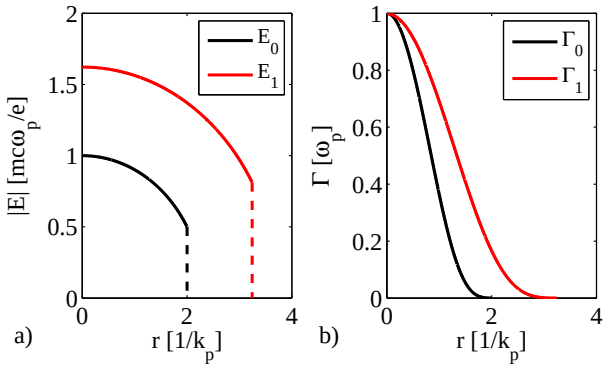

Figure 3.4: a) The magnitude of the electric field along a Ψ contour for $\tau_0 - \tau_a = 2/k_p$, E_0, and $\tau_0 - \tau_a = 3.244/k_p$, E_1. b) The ionization rate of helium along a Ψ contour at $\tau_0 - \tau_a = 2/k_p$ for $n_p = 8.0{\cdot}10^{23}$ m^{-3} , Γ_0, and at $\tau_0 - \tau_a = 3.244/k_p$ for $n_p = 2.7{\cdot}10^{23}$ m^{-3}, Γ_1. Reprinted with permission from [39]. Copyright 2009, American Physical Society.

Figure 3.4a shows $|E|$ from this equation as a function of r, E_1, and Fig. 3.4b shows the corresponding ionization rate for helium, Γ_1, as a function of r. The radial extent of this rate corresponds to $\langle x_0^2 \rangle = 0.92/k_p^2$. Similarly, the ionization rate from E_0 for helium equals ω_p at a density of $8.0{\cdot}10^{23}$ m^{-3} . Figure 3.4b shows the ionization rate corresponding to E_0 at this plasma density, Γ_0, as a function of r. The radial extent of this rate corresponds to $\langle x_0^2 \rangle = 0.36/k_p^2$.

Both ionization locations, front and back, therefore have a minimum initial size of order $1/k_p$. It is then appropriate to characterize the minimum achievable emittance with $\langle x_0^2 \rangle \approx 1/k_p^2$. This yields a minimum value of $\epsilon_{N,x} = 1/(4k_p)$, which is proportional to $n_p^{-1/2}$. The previous paragraph indicates that an initial transverse size can occur slightly below $1/k_p$, so $1/(4k_p)$ only sets the scale for the minimum achievable emittance. Since electrons in a laser wakefield accelerator [43] are expelled to radial distances significant compared to $1/k_p$ before becoming trapped, similar arguments and scales are applicable for the emittance of these electron bunches.

Three-dimensional OSIRIS [22] simulations provide support to the trapped electron emittance calculations. These simulations are of Gaussian drive bunches with I_d = 34.5, 17.2, 11.5, 8.62, and 6.90 kA driving a wake in a helium-lithium mixed plasma. For more detail refer to Sec. 2.4, where these simulations are introduced. Trapped electrons are not of a single energy, so $\epsilon_{N,x}$ (from Eq. 3.1) is calculated in

energy bins. Figure 3.5 displays the simulated $\epsilon_{N,x}$ for the trapped electrons as a function of energy. The mean values of $\epsilon_{N,x}$ for the trapped electrons in these sim-

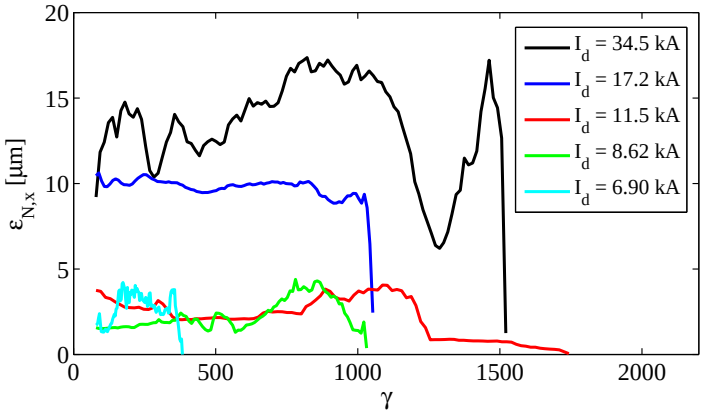

Figure 3.5: The normalized transverse emittance of the trapped electrons versus energy for several different values of I_d.

ulations in descending I_d order are 13.6±2.0, 9.94±0.33 , 2.74±0.61, 1.76±0.43, and 1.95±0.69 μm. These values correspond to the mean and rms of $\epsilon_{N,x}$ from a charge weighting of the energy bins. The relative small size of the rms values shows that $\epsilon_{N,x}$ is weakly dependent on the energy. These simulations indicate that trapped electrons can achieve $\epsilon_{N,x}$ at a fraction of $1/k_p$ (10 μm), as predicted by the model. Figure 3.6 shows the emittance values versus the drive bunch peak current. The large values of peak current create a large initial transverse size for the trapped electrons, leading to a large transverse emittance. For the lower values of peak current, the transverse emittance reduces and dips just below $1/(4k_p)$ before electron trapping turns off.

Two additional simulations test the scaling of the emittance with plasma density. Similar to the $I_d = 17.2$ kA simulation at $n_p = 2.7 \cdot 10^{23}$ m^{-3}, these simulations are of Gaussians with $I_d = 17.2$ kA ($\approx I_A$), matched transverse sizes of $\sigma_{x,y} = 0.17/k_p$, $\sigma_z = 2.0/k_p$, and have a simulation grid size of $0.05/k_p$ in x, y, and z. The simulations are at the plasma densities of $8.7 \cdot 10^{20}$ m^{-3} and $2.7 \cdot 10^{25}$ m^{-3}. Note, the plasma for these simulations does not consist of lithium with a small relative background of helium. At these plasma densities different species and ionization levels become trapped. For example, recall the discussion at the end of Sec. 2.6. This discussion shows that at the lowest of these plasma densities, lithium is no longer ionized very

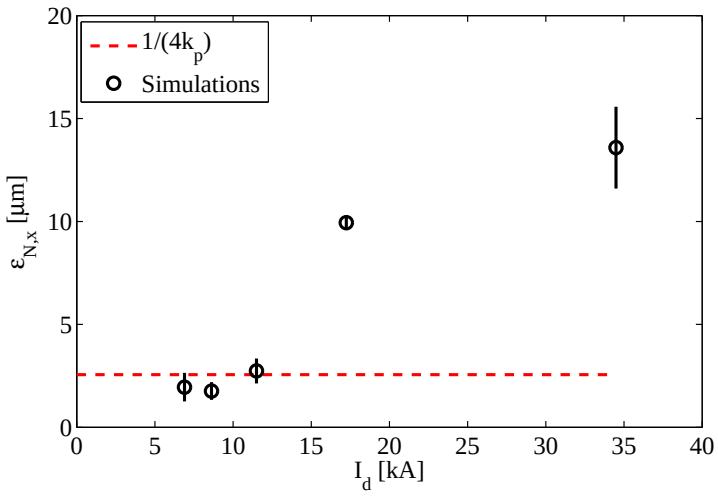

Figure 3.6: The mean normalized transverse emittance of the trapped electrons versus the drive bunch peak current, where error bars represent the rms spread of the emittance from a charge weighting of the energy bins.

quickly so its electrons can become trapped. Conversely, the first level of helium is ionized too quickly for its electrons to become trapped at a plasma density of $2.7 \cdot 10^{25}$ m^{-3}. Thus, to accommodate for the trapping of different ionization species and levels, the relative percent of helium, lithium, and pre-ionized gas was different at the different densities.

At $n_p = 8.7 \cdot 10^{20}$ m^{-3} the plasma is pre-ionized with a 3% background of lithium atoms, where the trapping occurs from the first ionization of lithium; at $n_p = 2.7 \cdot 10^{25}$ m^{-3} the plasma is helium with a 3% background of lithium atoms, where the trapping occurs mainly from the second and third ionization of lithium. The corresponding emittance numbers for the low and high density simulations are 135.5 and 0.747 μm with 5.2 and 0.081 μm rms emittance spreads, respectively. Earlier calculations suggest emittance scales as k_p^{-1}; a fit of the mean emittance numbers, weighted by their rms spreads, for the three simulations with $I_d \approx I_A$ yields that $\epsilon_{N,x}$ scales like k_p to the power of -0.94 $\pm$ 0.02. Figure 3.7 displays the simulated emittance of the trapped electrons versus k_p.

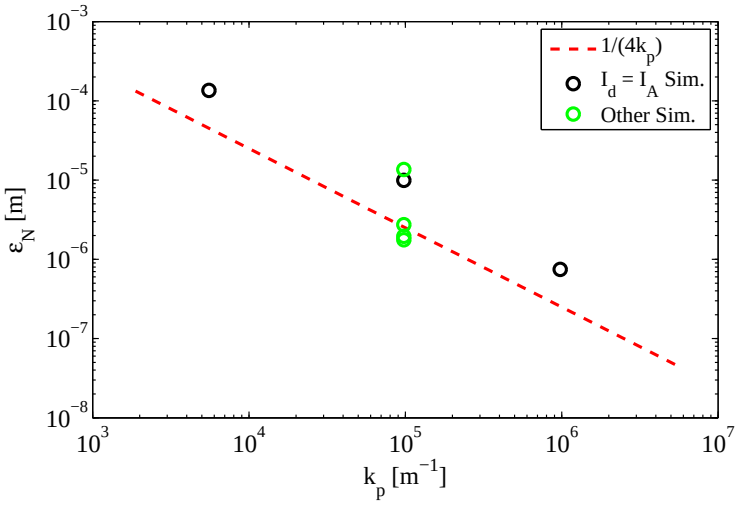

Figure 3.7: The mean normalized transverse emittance of the trapped electrons versus k_p. The black plot points are for the three simulations with $I_d \approx I_A$, and the other simulations appear as green plot points.

3.3 Charge and Peak Current

Plasma electron trapping causes charge to accumulate at the back of the ion bubble. As the amount of trapped charge increases, the transverse electric field of the trapped electron bunch increases, which decreases the radial current of the plasma sheath electrons at the back of the bubble. This loads E_z and changes the shape of Ψ, forcing the position for trapping farther back in the bubble. Eventually the wake loading from the trapped electrons ceases trapping at a given longitudinal position, which limits the total charge and peak current of the trapped electron bunch.

Section 2.4 discusses the requirements for inducing trapping. The drive bunch must have a peak current greater than $I_A/2$ and a total number of electrons greater than $1/(k_p r_e)$. This drive bunch transfers an outward radial momentum to the plasma sheath electrons at the front of the bubble. Then, the ion bubble turns this outward radial momentum into an inward one at the back of the bubble. To load the radial current associated with the inward moving plasma sheath electrons, the trapped bunch must have properties that are similar to the drive bunch. Thus, the maximum peak current and number of trapped electrons have scales that are characterized by those of the drive bunch.

Figures 2.5 and 2.6 provide support to the scale for the total number of trapped electrons. In addition, the corresponding OSIRIS simulations of the experiment, introduced in Sec. 2.4, run until the trapped electrons load the wake and turn off further trapping. This yields a maximum achievable trapped electron peak current, $I_{t,m}$. For $I_d = 34.5$, 17.2, 11.5, 8.62, and 6.90 kA, $I_{t,m} = 125$, 80.3, 42.2, 17.3, and 2.60 kA, respectively (see Fig. 3.8). Figure 3.9 displays the saturation of I_t as a function of propagation distance in the plasma for the simulation with $I_d = 17.2$ kA.

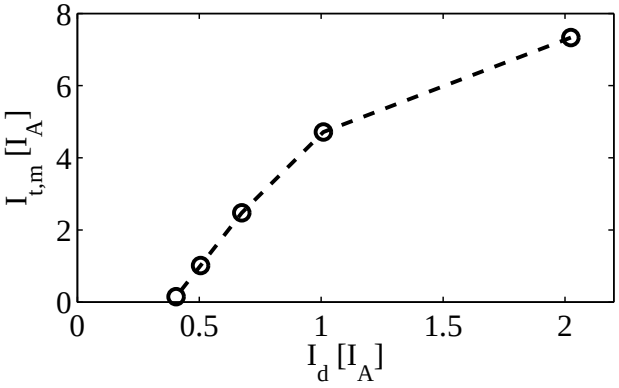

Figure 3.8: The maximum achievable trapped electron peak current versus the drive bunch peak current.

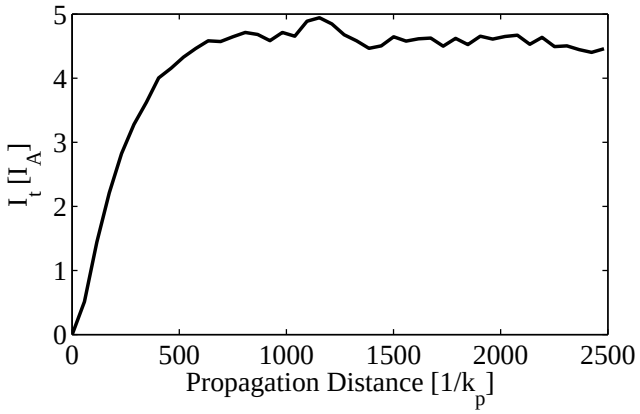

Figure 3.9: The peak current of the trapped electron bunch versus the drive bunch propagation distance.

3.4 Longitudinal Bunch Length

The scale for the longitudinal bunch length of the trapped electrons is found from an investigation of the time scale for ionization. If the ionization rate (Γ) of an atom is much less than ω_p, the atom will not be ionized. Conversely, if $\Gamma \gg \omega_p$, the atom will become ionized too quickly for its electron to be trapped. Thus, the time scale in the wake over which the trapped electrons are released is $1/\omega_p$, which corresponds to a longitudinal distance of $1/k_p$. This spread in the longitudinal position of ionization, dz_i, creates a spread in the initial Ψ: $d\Psi_i = |\partial_z \Psi| dz_i = |E_{z,i}| dz_i$, where $E_{z,i}$ is E_z at the location of ionization.

The constant of motion for an electron ($\gamma mc^2 - cp_z - e\Psi$) relates $d\Psi_i$ to the longitudinal bunch length at the back of the bubble, dz_b. As an electron accelerates in the plasma wake, cp_z converges to γmc^2. Therefore, the electron's constant of motion becomes $-e\Psi$ and is equal to $mc^2 - e\Psi_i$. If all of the electrons that are released by ionization become trapped, the spread of Ψ for the electrons at the back of the bubble, $d\Psi_b$, would equal $d\Psi_i$. However, only the electrons with $\Psi_i > \Psi_f + mc^2/e$ are trapped, so $d\Psi_b < d\Psi_i$. The quantity $d\Psi_b$ is connected to dz_b: $d\Psi_b = |E_{z,b}| dz_b$, where $E_{z,b}$ is E_z at the back of the bubble. This means that $|E_{z,i}| dz_i > |E_{z,b}| dz_b$. Thus, the bunch length for the trapped electrons is given by $dz_b < dz_i |E_{z,i}|/|E_{z,b}| \approx k_p^{-1} |E_{z,i}|/|E_{z,b}|$. Recall from Fig. 1.2 that $|E_{z,b}|$ can exceed $|E_{z,i}|$, so the trapped electron longitudinal bunch length, dz_b, can be a small fraction of $1/k_p$.

The three-dimensional OSIRIS simulations from Sec. 2.4 are now compared to this scale for the trapped electron longitudinal bunch length. At $n_p = 2.7{\cdot}10^{23}$ m^{-3}, where $1/k_p = 10$ μm, the trapped electrons have the rms longitudinal bunch lengths of 1.7, 2.2, 2.1, 1.4, and 2.2 μm for $I_d = 34.5$, 17.2, 11.5, 8.62, and 6.90 kA, respectively. In addition, at $n_p = 8.7{\cdot}10^{20}$ m^{-3} and $2.7{\cdot}10^{25}$ m^{-3} ($1/k_p = 180$ and 1 μm) the trapped electrons have the rms longitudinal bunch lengths of 36 and 0.15 μm, respectively, for $I_d = 17.2$ kA. These simulations indicate that the trapped electron bunches achieve longitudinal bunch lengths that are a fraction of $1/k_p$, as displayed in Fig. 3.10.

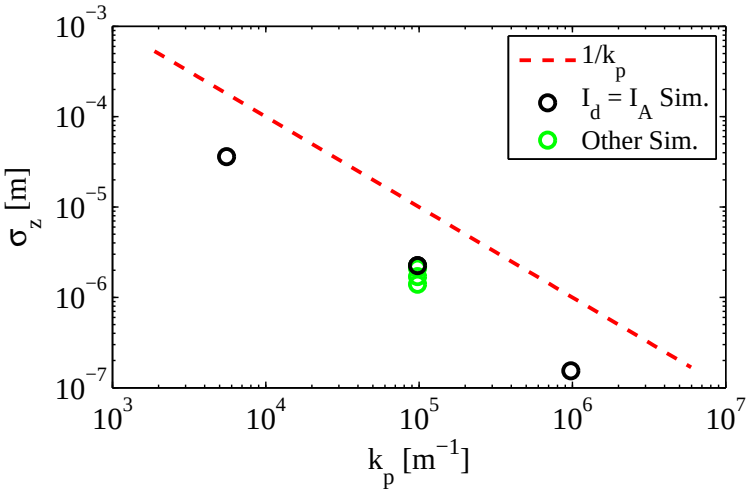

Figure 3.10: The rms bunch length of the trapped electron bunches, σ_z, versus k_p. The black plot points represent the three simulations with $I_d \approx I_A$, and the other simulations appear as green plot points.

3.5 Energy Distribution

Figure 3.11 displays the trapped electron energy profile for the simulations of the experiment at a propagation distance of $10^3/k_p$. For more detail refer to Sec. 2.4, where these simulations are introduced. The trapped electrons have large energy spreads, which are caused by two different aspects of the trapping process. First, the trapped electrons reside at the very back of the bubble, near the position where the electric field rapidly flips from accelerating to decelerating. Thus, the trapped electrons experience an accelerating field ranging from near zero to a scale of $mc\omega_p/e$. In addition, the energy spread is broadened by the wake collecting trapped electrons at different times. Two electrons at the same τ position in the wake experience the same E_z; however, if they are trapped at a different time, then their energy can be drastically different. For example, consider the wake loading displayed in Fig. 3.9. The trapped electron peak current saturates near a propagation distance of $800/k_p$. With $E_z = mc\omega_p/e$, the energy difference between an electron trapped at the beginning of this propagation compared to one near the saturation position is 800 mc^2.

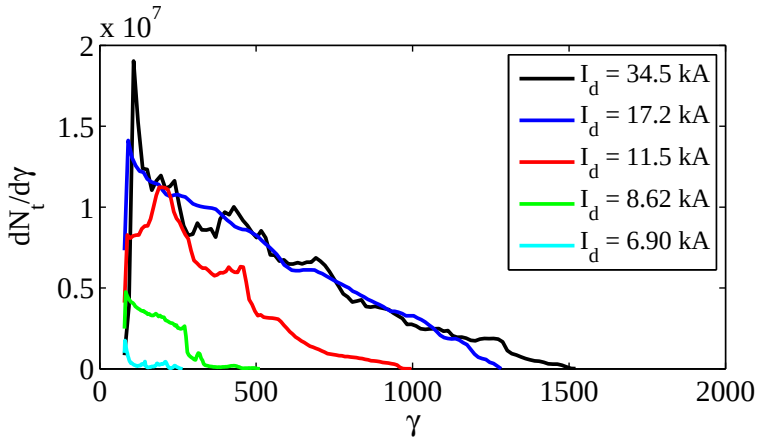

Figure 3.11: The trapped electron energy profile for a few different values of I_d at the propagation distance of $10^3/k_p$.

3.6 Multiple Trapped Bunches

The theory presented here focuses mainly on the trapped electron bunch in the first bubble. However, as discussed in Sec. 2.3, additional electron bunches become trapped in the multiple bubbles of the wake. A set of two-dimensional OSIRIS simulations of the experiment compares the properties of the trapped electron bunches in the first three bubbles of the wake. The drive bunches in these simulations are Gaussian with $1.8 \cdot 10^{10}$ electrons, matched transverse sizes of $\sigma_{x,y} = 1.74$ μm, and I_d = 34.5, 17.2, and 11.5 kA. These drive bunches create a wake in a lithium vapor of density $2.7 \cdot 10^{23}$ m^{-3} with a relative helium density of 10%. In r and z the simulation grid size is 0.5 μm, with 9 particles per cell. These simulations run until the trapped electrons load the wake and turn off further trapping. Table 3.1 displays a comparison of the mean transverse emittance, total number, and peak current for the first three bunches at the point in the propagation where the bunch charge saturates.

The trapped electron bunch in the first bubble has better properties than those trapped in the subsequent bubbles. As trapped electrons collect at the back of the bubbles, they load the wake. This loading decreases the energy of the plasma sheath electrons, which makes the wake easier to load in the subsequent bubbles. For this reason, the first trapped bunch contains the highest total charge and peak current. Note, the smallest transverse emittance occurs in the third bubble for the simulation

I_d [kA]	Bunch #	$\langle\epsilon_{N,x}\rangle$ [μm]	N_t	I_t [kA]
34.5	1	8.7	$1.2{\cdot}10^{10}$	85
34.5	2	13	$6.6{\cdot}10^{9}$	33
34.5	3	9.6	$5.6{\cdot}10^{9}$	29
17.2	1	5.7	$7.9{\cdot}10^{9}$	70
17.2	2	7.5	$4.6{\cdot}10^{9}$	38
17.2	3	6.4	$3.5{\cdot}10^{9}$	18
11.5	1	1.9	$3.2{\cdot}10^{9}$	34
11.5	2	1.9	$1.7{\cdot}10^{9}$	16
11.5	3	0.94	$2.3{\cdot}10^{8}$	2.7

Table 3.1: A comparison of properties for the electron bunches trapped in the first three plasma bubbles. The bunch # corresponds the bubble that the bunch is trapped in (1 for the first bubble).

with $I_d = 11.5$ kA. The bunch in this bubble achieves a transverse emittance that is roughly half of that for the bunch in the first bubble; however, the third bunch's total charge is only about 7% of that for the first bunch. Thus, the actual density of the electrons in phase space is higher for the first bunch.

3.7 Design of a Particle Source

The preceding sections cover the basic properties of the trapped electron bunches. This information is now used to explore the possibility of their use as a particle source. The primary issue for the trapped electron bunches is their longitudinal normalized emittance, expressed in Eq. 3.28.

$$\epsilon_{N,z} = \sqrt{\langle\delta z^2\rangle\langle\delta p^2\rangle - \langle\delta z\delta p\rangle^2}, \tag{3.28}$$

where $\delta p = p_z - \langle p_z\rangle$ and $\delta z = z - \langle z\rangle$. The trapped electron bunches have small longitudinal bunch lengths. However, due to their considerable size in δp, they acquire a large longitudinal emittance. Thus, it is important to discuss methods to minimize this momentum spread.

Conventional RF sources can generate electron bunches with longitudinal emittance of order MeV·ps [16] (300 MeV·μm/c). To be useful as a particle source, the trapped electron bunches must have significantly smaller longitudinal emittance than

this value. Section 3.4 shows that at the experimental plasma density, $2.7 \cdot 10^{23}$ m^{-3}, longitudinal bunch lengths of a few μm are achieved. To produce $\epsilon_{N,z}$ that is an order of magnitude better than conventional sources, these trapped bunches must have a longitudinal momentum spread of 10 MeV/c.

Section 3.5 discusses the two fundamental reasons for the large longitudinal momentum spread of the trapped electron bunches: the extended region over which electrons are trapped and the rapid variation of E_z at the back of the bubble. The first of these issues could be resolved by limiting the presence of the trapping species to only a small region in the plasma. Since E_z is of order $mc\omega_p/e$, this region must be $20/k_p$ in length or less to keep the momentum spread below 10 MeV/c. The second of the issues could be resolved by rapidly shifting to a lower plasma density after the trapping region. This shift in plasma density would increase the length of the ion bubble and push the location of the rapid variation in E_z to behind the trapped bunch.

At a plasma density of $2.7 \cdot 10^{23}$ m^{-3}, $20/k_p \approx 200$ μm. The production of a variation in the vapor density or gas species over this short of a distance would be difficult. Instead, pre-ionization of a single gas species at a uniform density can mimic the variation in the density of both the plasma and the trapping species. Consider a uniform vapor of a trapping species, such as helium in the experiment, with a density of n and the pre-ionization profile displayed in Fig. 3.12. The electrons from pre-ionization can not satisfy the trapping condition so they would support the plasma wake, while the leftover neutral atoms would seed the trapped electrons. At the region denoted by Δz, the plasma density is nP_1 and the neutral atom density is $n(1-P_1)$. The plasma density then drops to nP_2 after the Δz region. As the plasma density decreases (from nP_1 to nP_2), the location for the back of the ion bubble extends beyond the electrons trapped in Δz. The trapping of electrons could then still continue at the new location of the back of the bubble, but these electrons would not affect the bunch trapped in the Δz region.

Note, the drive bunch could further ionize the atoms in its vicinity, which would alter the plasma density from nP_1 and nP_2 in the two different regions. Outside of the drive bunch's ionization radius the plasma density would equal the pre-ionized values, but inside the plasma density would be higher. Thus, it is important for the

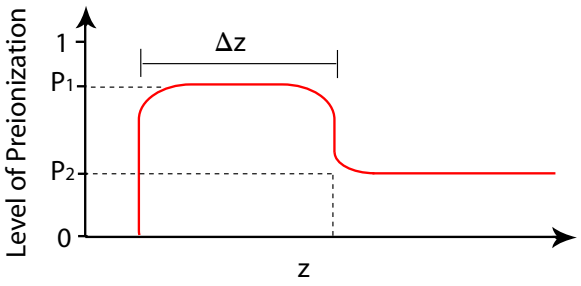

Figure 3.12: The level of pre-ionization versus z for a method to control the momentum spread of the trapped electron bunch.

drive bunch's ionization radius to be significantly smaller than the maximum radius of the ion bubble. This allows the density of the pre-ionized electrons to dominate the ion bubble length.

Figure 3.13 shows one idea for the production of such a pre-ionization profile. As usual, z denotes the drive bunch propagation direction. In the figure, a laser beam propagates perpendicular to the drive bunch, in the x direction, and collides with two obstructions. A full obstruction blocks the photons for z below the Δz region, while a partial obstruction transmits a fraction of the laser intensity for z above the Δz region; the light within the Δz region is not obstructed. The pre-ionization profile would be controlled by the laser intensity, the obstruction separation, and the transparency of the partial obstruction.

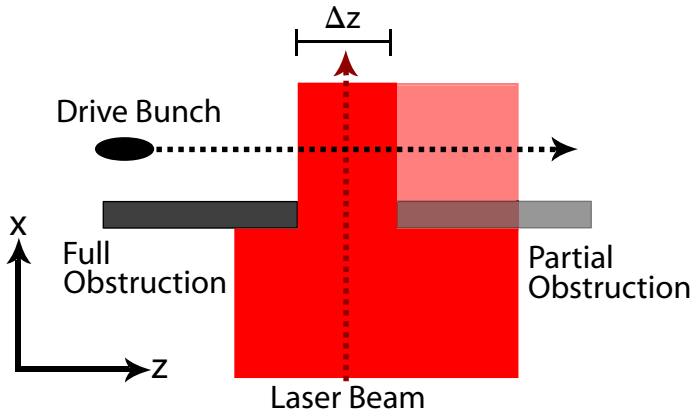

Figure 3.13: A method to control the trapped electron momentum spread. An obstruction placed in the path of a laser beam allows for the control of laser intensity, and therefore also the level of pre-ionization, along the drive bunch path.

A set of two-dimensional OSIRIS simulations test the trapped electron bunch properties created with these methods. The simulations use drive bunch parameters and a plasma density similar to those in the experiment. As displayed in Fig. 3.6, the decrease in drive bunch peak current from 17.2 to 11.5 kA yields a reduction in $\epsilon_{N,x}$ from 9.94 to 2.74 μm. This significant reduction in emittance only came at the cost of a factor of two reduction in the trapped electron bunch peak current. For this reason, the simulations use a drive bunch with $I_d = 11.5$ kA. Also, as in the experiment, the drive bunch has $1.8{\cdot}10^{10}$ electrons and matched transverse sizes of $\sigma_{x,y} = 1.74$ μm. The gas vapor is pure helium with a density of $2.7{\cdot}10^{23}$ m^{-3}. In r and z the simulation grid size is 0.5 μm with 9 particles per cell.

The remaining parameters for these simulations are P_1, P_2, and Δ_z. To reduce this three-dimensional simulation space to two, P_2 is set as constant times P_1: $P_2 = 0.6{\cdot}P_1$. This way the relative growth of the ion bubble remains fixed. To insure that the electrons from pre-ionization dominate the time scale of the ion bubble, P_1 is set to be greater than or equal to 0.5. Also, to allow for sufficient helium atoms from which to trap, P_1 does not exceed 0.9. These simulations use P_1 varied from 0.5 to 0.9 in steps of 0.1. The quantity Δ_z is varied from $5/k_p$ to $30/k_p$ in steps of $5/k_p$, and the final propagation distance is $z = 200/k_p$.

Figure 3.14 shows p_z versus $z - ct$ and the corresponding p_z distribution for the simulation with $P_1 = 0.9$ and $\Delta_z = 25/k_p$. As discussed, electron trapping continues behind the mono-energetic bunch, so there is a large spread in the low momentum electrons. To examine the properties of the mono-energetic part of the distribution, cutoffs are made in $z - ct$ and p_z (red lines in Fig. 3.14a). Figures 3.15, 3.16, and 3.17 display the characteristics of the trapped bunches from the simulations. These simulations show that the trapped bunches can simultaneously achieve small transverse and longitudinal emittances, large peak currents, and low longitudinal momentum spreads. The longitudinal emittances, displayed in Fig. 3.16a, are all an order of magnitude better than conventional sources. However, these simulations have a relatively short propagation distance of $200/k_p$ (2 mm). As is shown later, the longitudinal emittances increases for longer propagation distances.

The two-dimensional OSIRIS simulations are noisy, so a three-dimensional OSIRIS simulation is run to further test this method of producing mono-energetic trapped

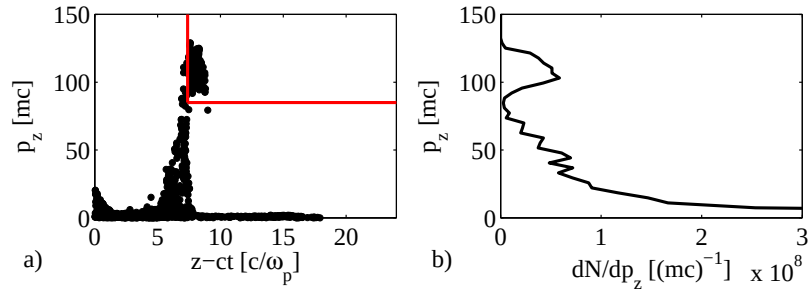

Figure 3.14: a) The quantity p_z versus $z-ct$ and b) the projected momentum spectrum for a mono-energetic trapped bunch, from the simulation with $P_1 = 0.9$ and $\Delta_z = 25/k_p$.

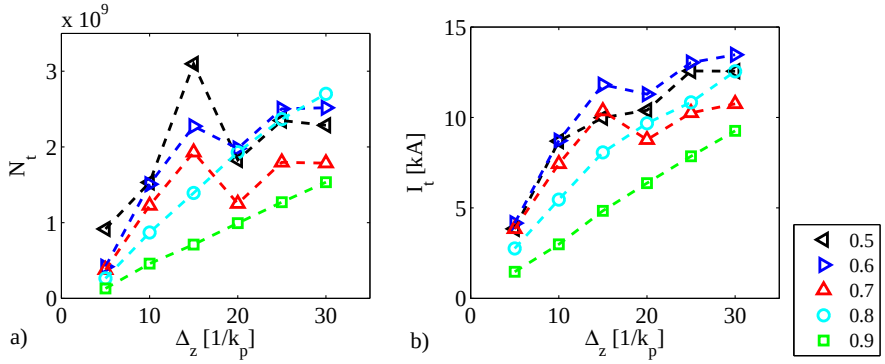

Figure 3.15: a) The total number, N_t, and b) peak current, I_t, for the simulated mono-energetic trapped electron bunches versus Δ_z. The markers in the plot denote the corresponding values of P_1.

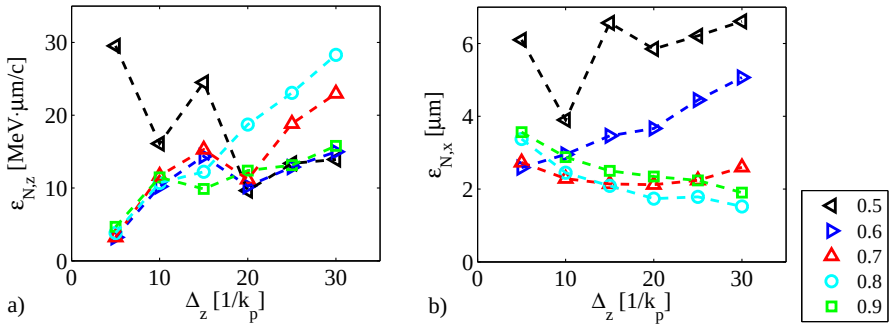

Figure 3.16: a) The longitudinal and b) transverse normalized emittances, $\epsilon_{N,z}$ and $\epsilon_{N,x}$, for the simulated mono-energetic trapped electron bunches versus Δ_z. The markers in the plot denote the corresponding values of P_1.

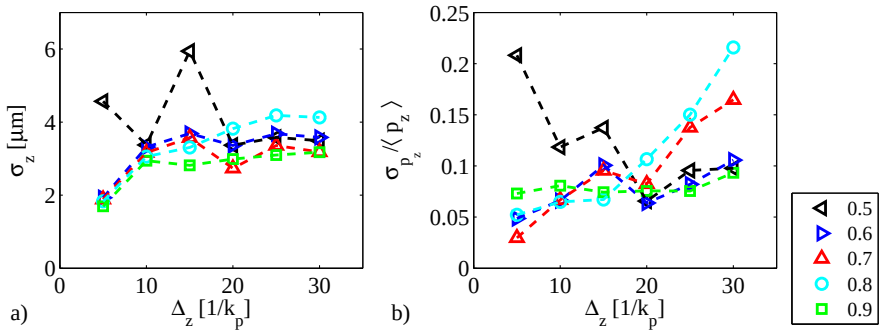

Figure 3.17: a) The rms longitudinal bunch length, σ_z, and b) the relative rms longitudinal momentum spread, $\sigma_{p_z}/\langle p_z \rangle$, for the simulated mono-energetic trapped electron bunches versus Δ_z. The markers in the plot denote the corresponding values of P_1.

electron bunches. Also, the three-dimensional simulation has a longer propagation distance than the two-dimensional ones, which enables an investigation into the effect of propagation on the trapped electron bunch. This simulation has $P_1 = 0.9$, $\Delta_z = 25/k_p$, and a 2 cm propagation distance. The drive bunch in this simulation is a Gaussian with $1.8 \cdot 10^{10}$ electrons, matched transverse sizes of $\sigma_{x,y} = 1.74$ μm, and $I_d = 11.5$ kA ($\sigma_z = 30$ μm). In addition, the simulation grid size in x, y, and z is 0.5 μm with 2 or 4 particles per cell. Figure 3.18 shows p_z versus $z - ct$ at the propagation distance of 2 cm.

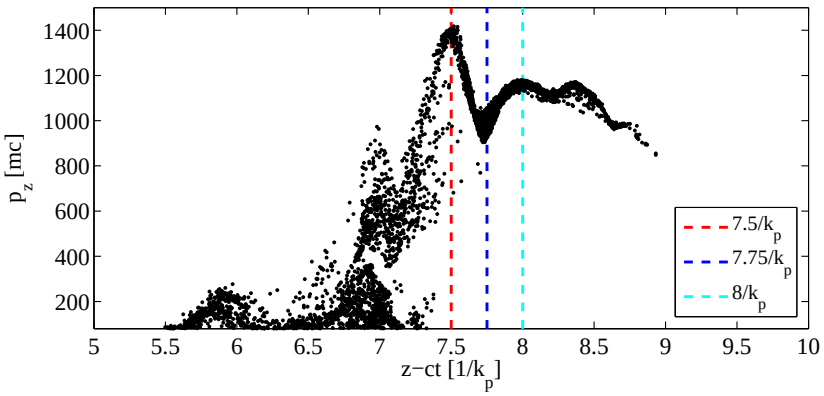

Figure 3.18: The quantity p_z versus $z - ct$ for a mono-energetic trapped bunch at a propagation distance of 2 cm, where $P_1 = 0.9$ and $\Delta_z = 25/k_p$. The dotted lines show several $(z - ct)$ cutoffs for analyzing the bunch properties, where only electrons with $z - ct$ above the cutoff are included in the property calculations.

The properties of the bunch change depending on the location chosen for the $(z - ct)$ cutoff. Figure 3.19 displays the transverse and longitudinal emittance of the trapped bunch for the different $(z - ct)$ cutoffs as a function of propagation distance. Similarly, Fig. 3.20 shows the total charge and relative longitudinal momentum spread of the trapped bunch for the cutoffs as a function of propagation distance.

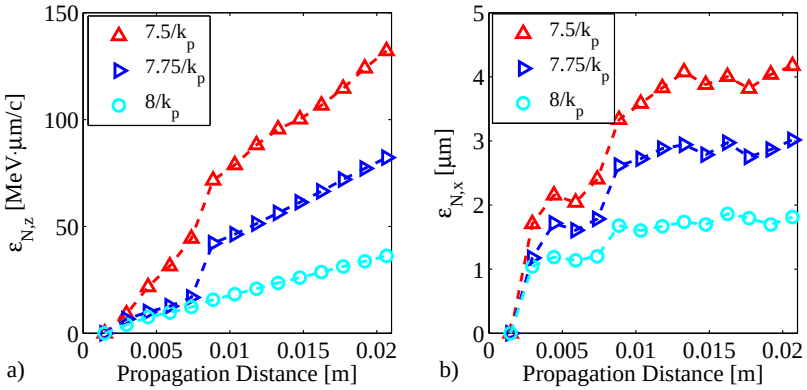

Figure 3.19: a) The quantities $\epsilon_{N,z}$ and b) $\epsilon_{N,x}$ versus propagation distance for a mono-energetic trapped bunch, where $P_1 = 0.9$ and $\Delta_z = 25/k_p$. The markers denote the $(z - ct)$ cutoffs used to analyze the bunch properties.

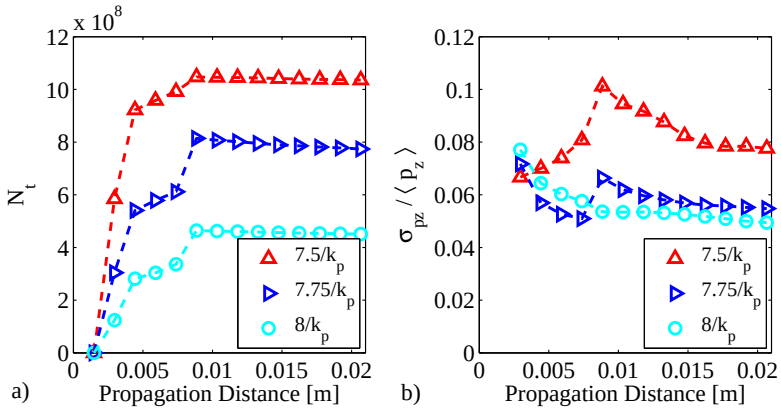

Figure 3.20: a) The total number of electrons, N_t, and b) the relative longitudinal momentum spread, $\sigma_{p_z}/\langle p_z \rangle$, versus propagation distance for a mono-energetic trapped bunch, where $P_1 = 0.9$ and $\Delta_z = 25/k_p$. The markers denote the $(z - ct)$ cutoffs used to analyze the bunch properties.

The three-dimensional simulation confirms that the trapped electron bunches can obtain small longitudinal emittance. Note, however, the longitudinal emittance grows

as a function of propagation distance (see Fig. 3.19a). This is due to the nonlinearity of the accelerating field at the back of the bubble. Thus, minimizing the longitudinal emittance requires minimizing the propagation distance, but this comes at the cost of the mean energy for the trapped electron bunch. For all three $(z - ct)$ cutoffs, the mean energy of the bunch rises linearly to roughly 560 MeV (559, 565, and 569 MeV) at the end of the 2 cm propagation distance. If these bunches were only able to propagate to half of this distance, they would only have half of this energy. Also, the choice for the cutoff affects the determined longitudinal emittance. The bunch corresponding to the highest $(z - ct)$ cutoff has the smallest longitudinal emittance, which is an order of magnitude better than conventional electron sources even at the full propagation length. However, this cutoff naturally yields the lowest bunch charge. Due to the trade-offs that occur between the different bunch properties, the best-case properties for this bunch depend on the specifics of the application.

Chapter 4

Experimental Overview

4.1 Introduction

Chapter 2 shows that electron trapping in a PWFA requires drive bunches of high charge ($> 1/(k_p r_e)$) and high peak current ($> I_A/2 = 8.5$ kA). Many accelerators utilize electron bunches that satisfy the charge requirement; however, the same is not true for the peak current requirement. The SLAC linac uses several stages of longitudinal compression to produce high peak current electron drive bunches. A detailed discussion of the compression process appears in Sec. 4.2.

In addition, Ch. 2 discusses the requirements on the plasma density and atomic species to create electron trapping. These requirements are satisfied by a lithium heat-pipe oven with a helium buffer gas [53]. The drive bunches easily ionize the relatively low first ionization level of lithium (5.4 eV), producing plasma electrons. These electrons support the plasma wake, while the higher ionization energy of helium (24.6 eV) permits some of its electrons to satisfy the trapping criterion [58]. Thus, the heat-pipe oven is a crucial component in the trapping process. Section 4.3 covers the physics of this oven.

Experimental diagnostics yield measurements of the onset in plasma electron trapping and the trapped electron bunch properties. An energy spectrum of the drive bunch, before it enters the heat-pipe oven, yields the bunch's longitudinal current profile. In addition, a pyroelectric detector collects coherent transition radiation (CTR),

emitted from the drive bunch as it passes through a titanium foil, for use as a complementary bunch length measurement. Charge measuring toroids, placed up- and downstream of the heat-pipe oven, measure the number of trapped electrons. Also, a combination of several energy spectrometers provides a total momentum spectrum of the drive bunch and trapped electron bunch following the heat-pipe oven. Section 4.4 gives an overview of these diagnostics.

4.2 Production of High Peak Current Bunches

The SLAC injector accelerates and bunches electrons emitted from a dispenser type cathode thermionic gun [66]. These electron bunches then enter a damping ring, which reduces their transverse and longitudinal emittances. Upon exiting the damping ring, the bunches have $1.8{\cdot}10^{10}$ electrons, a longitudinal length of 6 mm, a mean energy of 1.19 GeV, and a relative rms energy spread of 0.074%. This corresponds to a peak current of only 57 A.

Several stages of longitudinal compression on the drive bunch create a peak current large enough to induce plasma electron trapping. The compression process consists of two different types of longitudinal phase space (z and p_z) manipulations: shearing of the bunch in the z and p_z coordinates. Let $\delta p = p_z - \langle p_z \rangle$ and $\delta z = z - \langle z \rangle$. An acceleration of the bunch with a δz-dependent E_z changes a particle's p_z based on its z, shearing the bunch distribution in δp (see Fig. 4.1a). Similarly, a momentum dependent path length changes a particle's z based on its p_z, shearing the bunch distribution in δz (see Fig. 4.1b). The following sections describe the compression of the electron bunches from the damping ring. Note, the electrons are ultrarelativistic and propagating in the z direction, so $p_z c$ and the energy of an electron are interchangeable.

Nonlinear effects are important for the compression of the SLAC electron bunch; however, linear shears demonstrate the basic compression process. Thus, a matrix, $M_{z,p}$, multiplication represents compression:

$$\begin{pmatrix} \delta z_f \\ \delta p_f \end{pmatrix} = M_{z,p} \begin{pmatrix} \delta z_i \\ \delta p_i \end{pmatrix} = \begin{pmatrix} R_{55} & R_{56} \\ R_{65} & R_{66} \end{pmatrix} \begin{pmatrix} \delta z_i \\ \delta p_i \end{pmatrix}, \tag{4.1}$$

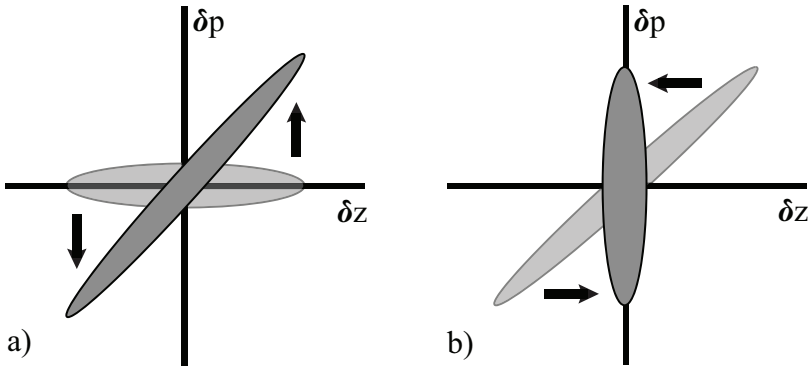

Figure 4.1: Longitudinal phase space manipulations. a) The shearing of a bunch in p_z and b) in z.

where the subscripts i and f denote initial and final, respectively. A shear in δp is given by

$$M_{z,p} = \begin{pmatrix} 1 & 0 \\ R_{65} & 1 \end{pmatrix}, \tag{4.2}$$

and a shear in δz is given by

$$M_{z,p} = \begin{pmatrix} 1 & R_{56} \\ 0 & 1 \end{pmatrix}. \tag{4.3}$$

Thus, matrices with a determinant of 1 represent the linear shears. The determinant for a product of matrices is equal to the product of the determinants for the matrices, so a matrix describing any arbitrary combination of these linear shears also has a determinant of 1. A bunch's longitudinal normalized emittance, $\epsilon_{N,z}$, is given by

$$\epsilon_{N,z}^2 = \langle \delta z^2 \rangle \langle \delta p^2 \rangle - \langle \delta z \delta p \rangle^2. \tag{4.4}$$

The propagation of the longitudinal phase space coordinates with $M_{z,p}$ yields

$$\epsilon_{N,z,f} = det(M_{z,p}) \epsilon_{N,z,i}, \tag{4.5}$$

making the longitudinal normalized emittance a conserved quantity for linear shears. Thus, the electron bunches can only compress in δz if they decompress in δp. A bunch with $1.8 \cdot 10^{10}$ electrons requires a bunch length of $\sigma_z = 20$ μm to obtain a peak current

equal to I_A . The initial phase space from the damping ring has no correlation term. Therefore, the reduction of σ_z from 6 mm to 20 μm requires at least an increase in the energy spread from 0.88 MeV to 0.26 GeV. In addition, the propagation of electron bunches with relative energy spreads greater than 10^{-2} is difficult; a multiplication of the final required energy spread with 100 yields the final mean energy needed to create these high peak current bunches: 26 GeV.

4.2.1 Radio Frequency Cavities

The p_z shearing of the bunch distribution occurred in S-band radio frequency (RF) accelerating cavities, which have a frequency of 2.856 GHz and a wavelength, λ_{RF}, of 10.5 cm. In these cavities, accelerating modes have a phase velocity equal to the speed of light, so the phase of the ultrarelativistic electrons relative to the mode, ϕ_{RF}, remains fixed. The integral of E_z over the length of the cavity results in a change to an electron's energy based on its phase:

$$\Delta U = U_0 \sin(\phi_{RF}), \tag{4.6}$$

where ΔU is the change in energy, and U_0 is the change in energy for an electron at the crest of the accelerating mode (see Fig. 4.2).

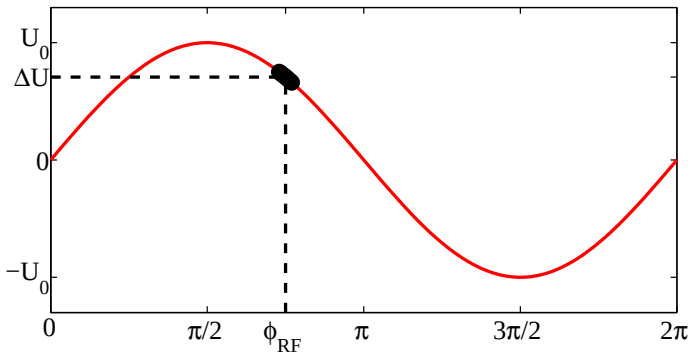

Figure 4.2: The phase-dependant acceleration of a particle bunch in a radio frequency cavity.

In addition to the change in the energy from the accelerating mode, the electron bunches experience longitudinal wakefields as they pass through the irises of the

accelerating cavities. The length between cavity irises is 3.449 cm, and the radius of the irises is 1.163 cm. Figure 4.3 displays the resulting wakefield, W_f, [4] for a single particle. The resulting accelerating field at a given longitudinal position, $\tau(z - ct)$, is

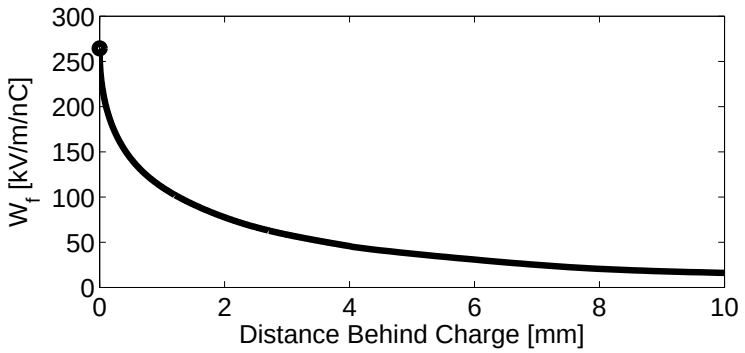

Figure 4.3: The longitudinal wakefield in the RF cavities.

the convolution of this wakefield with the charge per unit length, Q:

$$E_z(\tau) = -\int_{\tau}^{\infty} W_f(\tau' - \tau) Q(\tau') d\tau'. \tag{4.7}$$

4.2.2 Longitudinal Compression

Magnetic elements create momentum dependent path lengths, which result in a shear to the electron bunch in δz. FODO-cell arcs, magnetic chicanes, and doglegs are examples of the elements used for compression. Nonlinear path length dependencies require a modification to the formalism for linear shears. The change in δz for an electron is given as

$$\delta z_f = \delta z_i + R_{56}\delta p_i + T_{566}\delta p_i^2. \tag{4.8}$$

4.2.3 LiTrack

The code LiTrack [4] is used to simulate the longitudinal phase space evolution from the damping ring to the experiment. This code includes the p_z shearing of the bunch, as expressed in Eqs. 4.6 and 4.7, and the z shearing of the bunch, shown in Eq. 4.8. Figure 4.4 displays the compression elements in the SLAC linac leading up to the experimental hall.

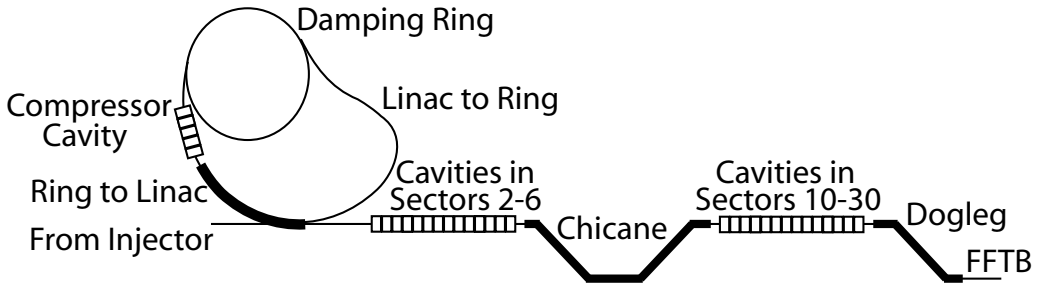

Figure 4.4: The longitudinal compression elements in the SLAC linac. The ring to linac, chicane, and dogleg shear the bunch in z, while the cavities shear the bunch in p_z.

4.2.4 Damping Ring to the Linac

During the first step of compression, the compressor cavity shears the bunch distribution in δp. In reference to Eq. 4.6, the phase of an electron is $\phi = \phi_{RF} + 2\pi\delta z/\lambda_{RF}$, and $U_0 = 42$ MeV. Inside the compressor cavity $\phi_{RF} = 0$. The mean energy of the bunch does not change; however, the electrons at the front of the bunch receive more energy than those in the back, shearing the distribution in δp. Next, the electrons travel through a FODO-cell arc. The dispersion of the arc creates longer path lengths for larger momentum particles. In this arc, R_{56} = -0.495 m·c/GeV and T_{566} = -0.744 m·$(c/\text{GeV})^2$. Electrons with energies more than 2 to 3 % off of the nominal energy get clipped and do not make it to the linac. Figure 4.5 displays the results for a LiTrack simulation of the propagation from the damping ring to the linac.

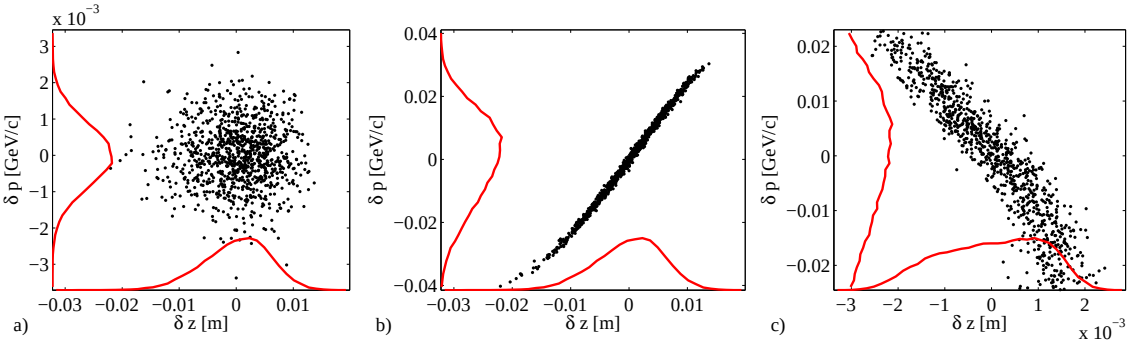

Figure 4.5: The first stage of bunch compression. The $\delta z - \delta p$ phase space a) at the end of the damping ring, b) after the compressor cavity, and c) after propagation through the FODO-cell arc in the ring to linac.

4.2.5 Acceleration in Sectors 2 through 6 of the Linac

During the next stage of compression, the accelerating cavities in Sectors 2 through 6 of the main linac shear the bunch distribution in δp and raise the mean bunch energy from 1.19 GeV to roughly 9 GeV. In these sectors, $\phi_{RF} = 1.911 + \phi_{ramp}$ and $U_0 = 8.444$ GeV, where ϕ_{ramp} is a quantity that is varied during the experiment.

4.2.6 Magnetic Chicane at Sector 10

Next, the electron bunches pass through a magnetic chicane. The dispersion of this chicane creates longer path lengths for lower momentum particles. In the chicane, $R_{56} = 8.44$ mm·c/GeV and $T_{566} =$ -1.41 mm·$(c/\text{GeV})^2$. Figure 4.6 displays the results for a LiTrack simulation of the propagation from the start of the main linac through the magnetic chicane.

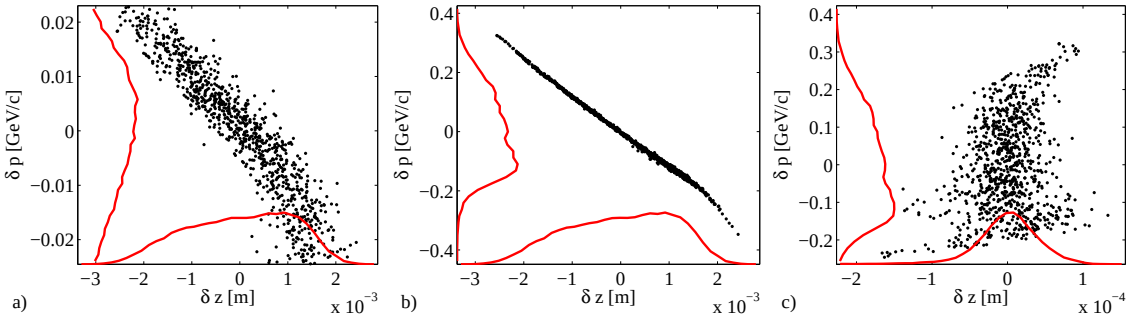

Figure 4.6: The second stage of bunch compression. The $\delta z - \delta p$ phase space a) after the ring to linac arc, b) following the accelerating cavities in Sectors 2 through 6, and c) after the magnetic chicane.

4.2.7 Acceleration in Sectors 10 through 30 of the Linac

The accelerating cavities in Sectors 10 through 30 of the main linac take the mean energy of the electron bunches from roughly 9 GeV to 42.2 GeV. In these sectors, $\phi_{RF} = \pi/2 + \phi_{ramp}$. The electron bunch lengths are significantly smaller in these sectors than they are in Sectors 2 through 6, which lessens the shearing effects of the RF and increases the shearing effects of the wakefields.

4.2.8 Transport into the FFTB

Finally, the electron bunches pass through a dogleg into the FFTB. The dispersion of this dogleg creates longer path lengths for higher momentum particles. Note, the properties of the dogleg are not constant during the experiment, but typical compression values are R_{56} = -35.5 μm·c/GeV and T_{566} = -1.68 μm·$(c/\text{GeV})^2$. Figure 4.6 displays the results for a LiTrack simulation of the propagation from Sector 10 to the experimental chamber. This final stage completes the compression of the longitudinal bunch size from 6 mm to tens of μm.

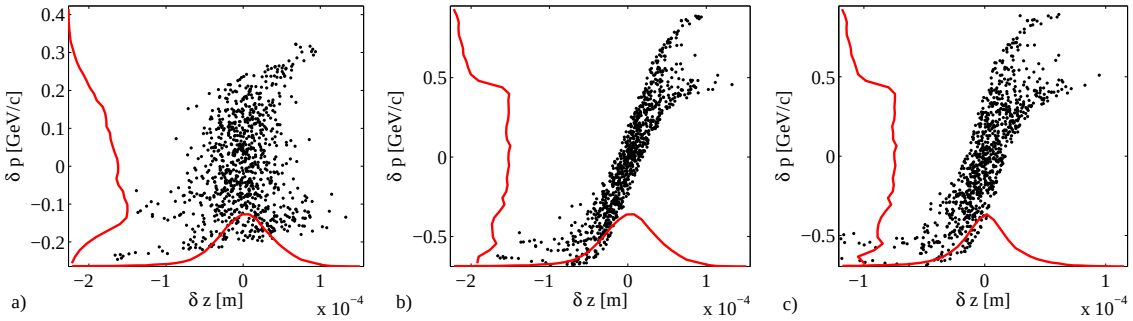

Figure 4.7: The third stage of bunch compression. The $\delta z - \delta p$ phase space a) after the magnetic chicane, b) following the accelerating cavities in Sectors 10 through 30, and c) after the FFTB dogleg.

4.3 Heat-Pipe Oven

An investigation into the properties of a liquid-gas phase transition yields a basic understanding of the heat-pipe oven. These properties are revealed by the first and second laws of thermodynamics [15]. The first law of thermodynamics states that the change in the energy of a system, dU, is equal to the energy added to the system, dQ, minus the work done the system, which is the pressure, P, times the change in the volume, dV.

$$dU = dQ - PdV. \tag{4.9}$$

The second law of thermodynamics states that the change in entropy of a system, dS, times its temperature, T, is greater than or equal to the energy added to the system,

where they are equal for a reversible process.

$$TdS \geq dQ. \tag{4.10}$$

A liquid-gas phase transition is a reversible process, so the greater than part of Eq. 4.10 is dropped. The combination of the first and second laws of thermodynamics yields

$$dU = TdS - PdV. \tag{4.11}$$

Equation 4.11 represents the internal energy of the system with S and V as its independent variables. The quantity T is the canonical conjugate to S, and $-P$ is the canonical conjugate to V. Three other thermodynamic potentials result from a change of the independent variable: the Gibbs function, the enthalpy, and the Helmholtz function. The Gibbs function, G, has P and T as independent variables.

$$G = U + PV - TS. \tag{4.12}$$

$$dG = dU + VdP + PdV - TdS - SdT = VdP - SdT. \tag{4.13}$$

For a liquid-gas phase transition, the pressure and temperature of the liquid is equal to that of the gas. Suppose that a system containing liquid and gas in equilibrium is kept at a constant temperate and pressure while expanding the volume. This would result in molecules changing from the liquid to the gas phase. There is no change in temperature or pressure, so the Gibbs function of the system remains constant. Since there is a net change of molecules from the liquid to the gas phase, the Gibbs function per molecule in the liquid phase, g_l, must be equal to that in the gas phase, g_g. This is true for all the points along the vapor pressure curve, so the changes in the Gibbs function along this curve are also equal.

$$g_g = g_l \rightarrow dg_g = dg_l. \tag{4.14}$$

Let $v = V/N$, and $s = S/N$, where N is the number of molecules. A substitution of

$P[N/m^2]$	1	10	100	1,000	10,000	100,000
$T[K]$	797.45	885.45	995.25	1,144.35	1,337.45	1,610.25

Table 4.1: The vapor pressure of lithium versus temperature.

Eq. 4.13, divided by N, into Eq. 4.14 yields

$$v_g dP - s_g dT = v_l dP - s_l dT \rightarrow dP(v_g - v_l) = dT(s_g - s_l). \tag{4.15}$$

Equation 4.15 is simplified by the substitution of $v_g - v_l \approx v_g = k_B T/P$ (for an ideal gas), where k_B is Boltzmann's constant. The second law of thermodynamics gives $s_g - s_l = h/T$, where h is the heat of vaporization. These manipulations yield a simplified version of the Clausius-Clapeyron equation:

$$\frac{dP}{dT} = \frac{hP}{k_B T^2}. \tag{4.16}$$

The pressure is given by the integration of the above equation:

$$P = P_i \exp[\frac{1}{k_B}\int_{T_i}^{T} \frac{h(T')}{T'^2} dT']. \tag{4.17}$$

This equation requires one point along the vapor pressure curve as initial conditions, P_i and T_i. The heat of vaporization is technically a function of temperature; however, it can be treated as a constant ($2.442 \cdot 10^{-19}$ J for lithium [19]). This yields the following equation for the vapor pressure as a function of temperature.

$$P = P_i \exp[\frac{h}{k_B}(\frac{1}{T_i} - \frac{1}{T})]. \tag{4.18}$$

Table 4.1 displays six points on the vapor pressure curve of lithium [46].

The six points in Tbl. 4.1 allow for a check of how well Eq. 4.18 models the vapor pressure curve. Of the six points, the one at a temperature of 1337.45 K is closest to the temperature in the experiment so it is used as the initial condition. Figure 4.8 displays the vapor pressure curve generated by Eq. 4.18 and the data points from Tbl. 4.1. The ideal gas law yields the lithium vapor density from the pressure and temperature of the gas: $n = P/(k_B T)$. Equation 4.18 divided by $k_B T$ generates the

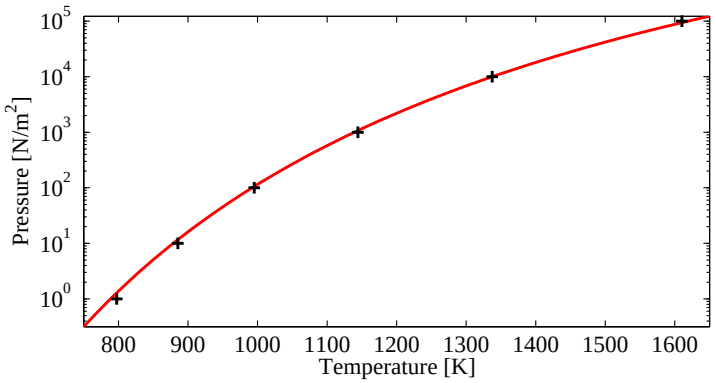

Figure 4.8: The vapor pressure of lithium versus temperature. The plus signs represent known points on the curve [46], and the red line denotes the vapor pressure curve generated from the Clausius-Clapeyron equation.

dependence of the vapor density on the temperature, shown in Fig. 4.9. A parametric

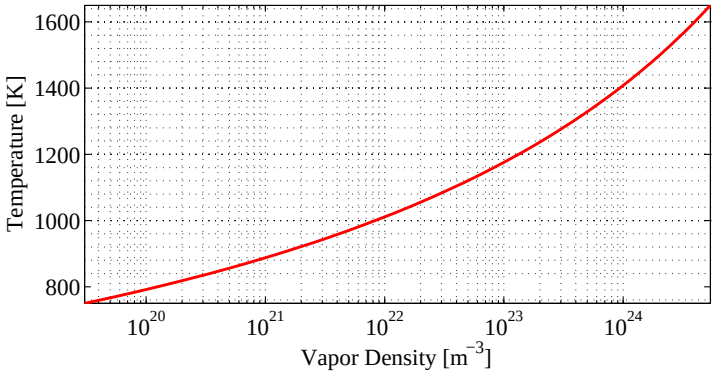

Figure 4.9: The temperature versus density of lithium, from the Clausius-Clapeyron equation.

plot displays the relationship between the pressure and the density (see Fig. 4.10).

Figure 4.11 is an illustration of the heat-pipe oven. This oven is built from a stainless steel tube, heaters, cooling jackets, and a wire mesh. The heaters create a hot region at the middle of the tube, which is bounded by cooling jackets. Inside the tube, the mesh acts as a wick for the molten lithium.

A summary for the initialization of the heat-pipe oven follows. First, a solid piece of lithium is placed on the wire mesh. Then, the tube is filled with helium gas at the required pressure and the heaters are turned on. As the oven temperature increases,

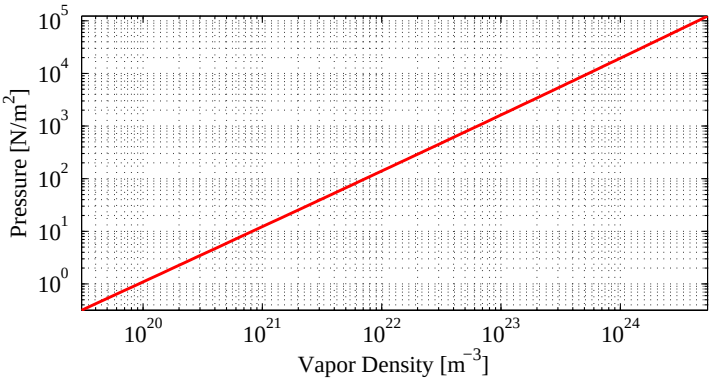

Figure 4.10: The pressure versus density of lithium, from the Clausius-Clapeyron equation.

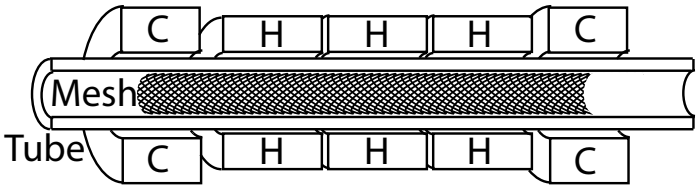

Figure 4.11: The heat-pipe oven, where the letter H denotes the heaters, and the letter C denotes the cooling jackets.

a hot region forms in the middle of the oven. The lithium begins to melt, vaporize, and flow out of the hot region. When the lithium vapor enters the cool region, it condenses on the mesh, and the capillary action of the wick draws it back to the hot region of the oven. This repeated process of vaporization, condensation, and wicking creates a flow of lithium that pushes the helium buffer gas out from the hot region of the oven.

The heat-pipe oven has two inputs: the pressure of the buffer gas and the power of the oven heaters. The vapor pressure of the lithium moves along the vapor pressure curve shown in Fig. 4.8. To produce a uniform density profile in the oven, the pressure of the buffer gas is set equal to the needed lithium vapor pressure and the oven heater power is increased until the lithium vapor pressure becomes equal to that of the system. The pressure in the oven is equal to the sum of the buffer gas and lithium vapor pressures; thus, in the hot region of the oven the vapor pressure of the buffer gas drops to zero.

The pressure in the system is constant, so the temperature in the oven can not

increase above the critical temperature where the lithium vapor pressure equals the system pressure. Thus, an increase in the heater power does not increase the temperature in the hot region of the oven beyond the critical temperature; it only increases the length of the oven at the critical temperature. The temperature along the heat-pipe controls the lithium density according to Eq. 4.18. Outside of the hot region, the temperature drops below the critical temperature, which allows the buffer gas to mix with the lithium. The cooling jackets sharpen the drop off of the temperature outside of the hot region, which sharpens the density drop off. Figure 4.12 displays the partial pressure of lithium and helium in the heat-pipe oven, determined by temperature measurements along the oven.

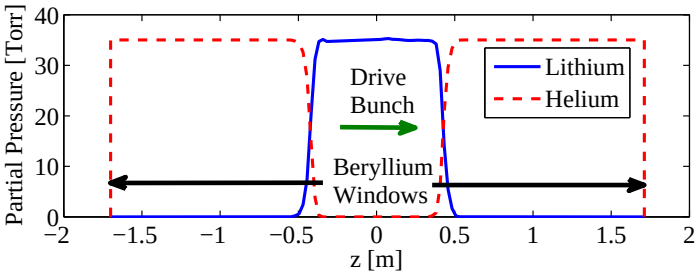

Figure 4.12: The partial pressures of lithium and helium in the heat-pipe oven. Berylliums windows located up- and downstream of the heat-pipe oven created boundaries between the helium buffer gas and the beam-line vacuum. Reprinted with permission from [37]. Copyright 2008, American Institute of Physics.

As discussed in Ch. 2, plasma electron trapping in this experiment is created by the presence of both helium and lithium atoms. Over the central heated region of the heat-pipe oven there is pure lithium vapor with a density of $2.7 \cdot 10^{23}$ m^{-3} and a FWHM length of 85 cm, but in the cool regions on either side of the heated region there is pure helium (see Fig. 4.12). In between, there are transition regions where both species are present. Electron trapping occurs in both the up- and downstream transition regions of the heat-pipe oven.

4.4 Experimental Diagnostics

Figure 4.13 displays a diagram of the experimental diagnostics in the FFTB.

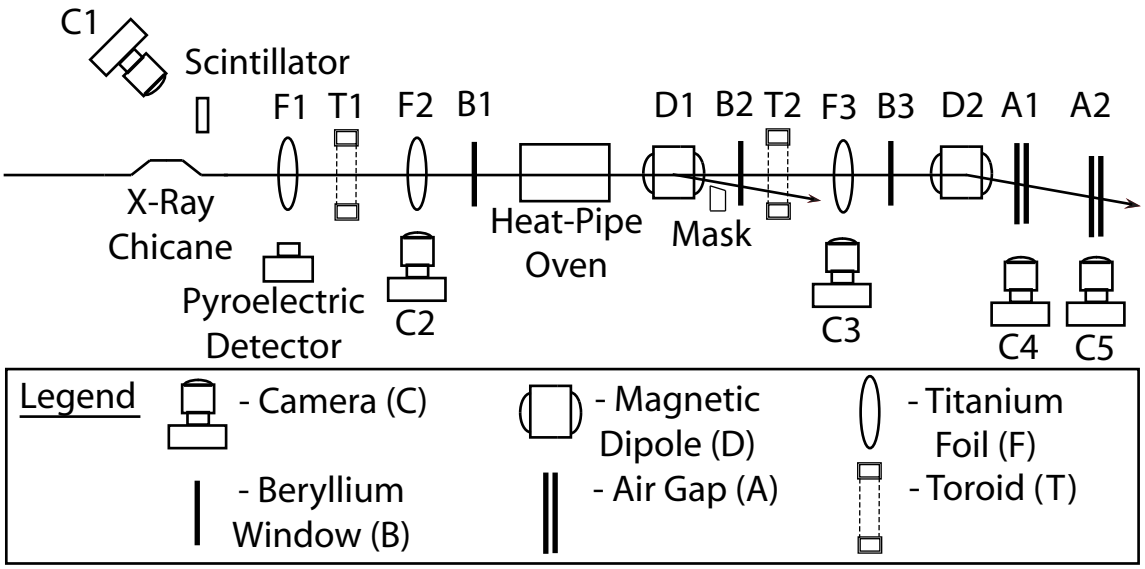

Figure 4.13: The experimental setup.

4.4.1 X-Ray Chicane Energy Spectrometer

A measurement of the drive bunch's energy spectrum as it enters the FFTB provides information of the bunch's longitudinal phase space. This measurement occurs at a region of high dispersion for the electrons in the x direction. In this region, the drive bunch electrons pass through a vertical (y) magnetic chicane, which causes a vertical deflection of the electrons (see Fig. 4.14). This vertical deflection induces the emission of synchrotron radiation directed into the $y - z$ plane. A cerium doped yttrium aluminum garnet scintillator, located above the bunch axis, absorbs this synchrotron radiation and re-emits optical light. Then, a 16-bit charge coupled device (CCD) camera (C1) images the light from the scintillator. The signature of an electron passing through the chicane is optical light emitted from the scintillator at the x position of the electron. Since the x position of an electron is correlated to its energy, images from the CCD camera, summed onto the x axis, yield an energy spectrum of the drive bunch.

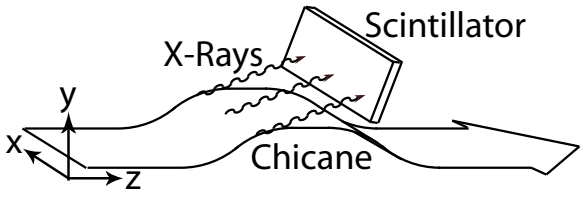

Figure 4.14: The X-ray chicane energy spectrometer.

4.4.2 Charge Measuring Toroids

Integrated current transformers provide a measurement of the total amount of charge that goes into and comes out of the heat-pipe oven. These transformers consist of a ring-shaped toroidal ferrite with wire coiled through its center. After multiple turns through the toroid center, the ends of the wire are connected with a resistor (R). The wire and toroid act as an inductor (L), so the combination of these with the resistor acts as an LR circuit. As an electron bunch traverses the center of the toroid, its azimuthal magnetic field induces a change in the magnetic flux through the toroid windings, which produces an electromotive force in the LR circuit. Then, an analog to digital converter records the voltage difference across the resistor. The time scale for the electron bunch to pass through the toroid is much less than the L/R time constant, so the LR circuit is only sensitive to the integrated current that passes through it. In addition, there is a single calibration winding through the center of the toroid. The toroid is calibrated to the amount of charge that passes through this calibration winding. Figure 4.15 shows an illustration of the charge measuring toroid.

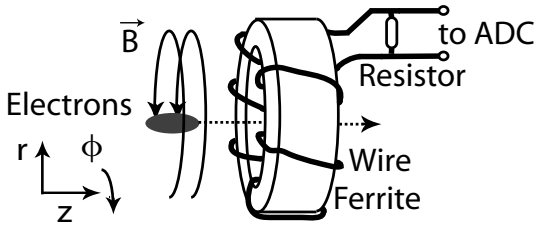

Figure 4.15: An illustration of a charge measuring toroid.

4.4.3 Optical Transition Radiation

The passage of a charged particle through a transition in the index of refraction results in the emission of transition radiation. In the experiment, transition radiation results as the drive bunch electrons pass through 1 μm thick titanium foils, which are placed at a 45 degree angle with respect the drive bunch propagation direction to direct the radiation off of the bunch axis. Cameras C2 and C3 image the incoherent optical transition radiation (OTR) that is emitted from foils F2 and F3. The transverse (x and y) distribution of the drive bunch is determined from these images and is used to triangulate the waist location, which is important for properly focusing the drive bunch into the heat-pipe oven. Note, the spatial resolution of the OTR is a critical issue for this measurement. A detailed analysis of this resolution in given in [2]. The OTR spatial resolution in this experiment is discussed in [5], which concludes that the resolution limit is much smaller than the transverse bunch size on these foils.

4.4.4 Coherent Transition Radiation

Transition radiation is also used as a qualitative longitudinal bunch length measurement. For this measurement, a Molectron P1-45-CC pyroelectric detector collects the transition radiation emitted from F1. This detector is sensitive to wavelengths on the order of the drive bunch longitudinal length (tens of μm). At wavelengths that are much larger than the drive bunch length, the bunch emits coherent transition radiation (CTR). Shorter drive bunches emit CTR over a larger range in wavelength, and therefore also emit more total transition radiation. Thus, the amount of transition radiation collected by the pyroelectric detector is correlated to the drive bunch length.

An investigation of the spectral composition for transition radiation reveals this correlation. The number of photons, N_γ, emitted per unit of angular frequency, ω, is

$$\frac{dN_\gamma}{d\omega} = \frac{2\alpha Z^2}{\pi\omega}(\log(\frac{\gamma\omega_p}{\omega}) - 1), \tag{4.19}$$

where α is the fine structure constant, Z is the unit charge of the particle, and ω_p is the plasma frequency for the transition material [75]. Note, $\gamma\omega_p$ is orders of magnitude

greater than ω for wavelengths of tens of μm, so the logarithm term can be treated as a constant. This allows for the simplification of $dN_\gamma/d\omega$ as

$$\frac{dN_\gamma}{d\omega} \propto \frac{Z^2}{\omega}. \tag{4.20}$$

A multiplication of Eq. 4.20 by a form factor and the substitution of the number of drive bunch electrons, N_d, as Z gives a formula for $\frac{dN_\gamma}{d\omega}$ from the drive bunch:

$$\frac{dN_\gamma}{d\omega} \propto \frac{N_d^2}{\omega} \exp(-\frac{\sigma_z^2\omega^2}{c^2}). \tag{4.21}$$

The pyroelectric detector measures the total energy deposited in it, *pyro*. Assuming perfect absorption yields a pyroelectric detector signal that is inversely proportional to the bunch length:

$$pyro \propto \int_0^\infty \omega \frac{N_d^2}{\omega} \exp(-\frac{\sigma_z^2\omega^2}{c^2}) d\omega \propto \frac{N_d^2}{\sigma_z} \tag{4.22}$$

The pyroelectric detector is not a perfect absorber, but this calculation is still useful for illustrating the inverse relationship between the pyroelectric detector signal and the electron bunch length.

4.4.5 Low Energy Mask Spectrometer

Most of the trapped electron charge occurs at low energies (tens of MeV). A low energy spectrometer measures the distribution for these low energy electrons. This spectrometer consists of a magnetic dipole (D1), a tungsten mask, and a charge measuring toroid (T2). The integrated magnetic field of the dipole, $\int B_x dz$, is variable up to a maximum of 0.033 Tm and creates a transverse momentum kick to the electrons:

$$\Delta p_y = -ec \int B_x dt = -e \int B_x dz. \tag{4.23}$$

This momentum kick yields an angular kick of

$$\Delta \dot{y} = -\frac{e}{p_z} \int B_x dz. \tag{4.24}$$

The front of the tungsten mask is located 6.67 cm downstream of the dipole center. This mask collects electrons that are dispersed from the magnet by more than 3.18 mm. Thus, the mask collects electrons with angular kicks of 0.0477 radians or greater. Equation 4.24 translates this angular cutoff into a momentum cutoff. At the maximum $\int B_x dz$ of the dipole, the mask intercepts electrons with momentum less than 207 MeV/c. The mask is 15 radiation lengths thick (5.1 cm). Electron gamma shower (EGS) simulations of 1 GeV electrons passing through this many radiation lengths of tungsten indicate that only photons make it out from the back of the mask; thus, the toroid only measures the charge not intercepted by the mask. A change of the dipole magnetic field changes the momentum cutoff. The amount of charge through the toroid as a function of dipole magnetic field yields a low energy spectrum. Figure 4.16 illustrates this spectrometer.

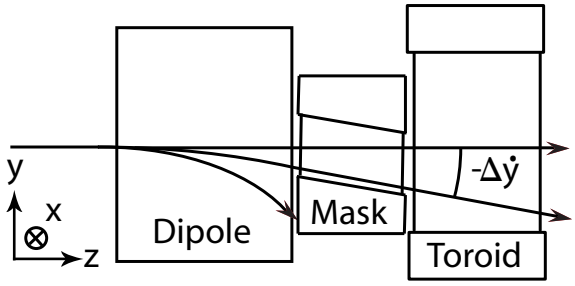

Figure 4.16: The low energy mask spectrometer.

4.4.6 Cherenkov Cell Energy Spectrometer

An additional energy spectrometer also uses the deflections from D1. A gas cell, contained by beryllium windows (B2 and B3), is located downstream of D1. This cell contains helium gas at a pressure of 1 atmosphere and a temperature of 294 K, which corresponds to an index of refraction equal to 1.0000325 (for optical wavelengths). Electrons with energy greater than 63 MeV travel faster than the speed of light in the gas so they emit Cherenkov radiation. A titanium foil inside this cell (F3) reflects the Cherenkov light off of the bunch axis. Then, a 12-bit optical CCD camera (C3) images the far-field of this light. Cherenkov radiation occurs in a narrow angular distribution about $\theta = \arccos(1/(\beta n))$, where θ is the angle off of the z axis, $\beta = v/c$,

and n is the index of refraction. Let $\beta = 1 - \delta$. For small θ, $\cos(\theta) \approx 1 - \theta^2/2$. Thus, $\theta = \sqrt{2/n}\sqrt{n - 1 - \delta}$. While δ is on the same scale as $n - 1$, energy information is contained in the Cherenkov angle. However, for $\delta \ll n - 1$ the Cherenkov angle asymptotically approaches $\theta = \sqrt{2 - 2/n}$. Therefore, Cherenkov radiation produced by electrons with energy much greater than the critical energy of 63 MeV does not have energy information contained in its angle. An image of the far-field for this radiation appears as a ring; the dispersion from the magnet makes different energy electrons appear as rings with different displacements. The maximum measurable energy, 10 GeV, corresponds to the minimum displacement that can be resolved from the Cherenkov ring of the drive bunch. Figure 4.17 illustrates the Cherenkov cell spectrometer.

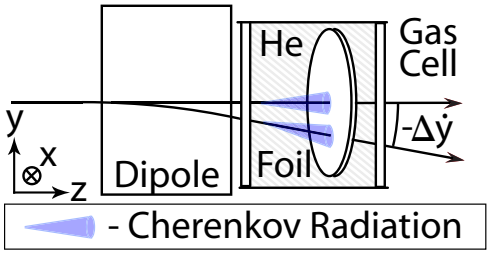

Figure 4.17: The Cherenkov cell energy spectrometer, which had an energy range from 63 MeV to 10 GeV.

4.4.7 Large Dipole Energy Spectrometer

Downstream of the bunch-plasma interaction, the electrons pass through an additional energy spectrometer, which consists of a magnetic dipole (D2), two air gaps (A1 and A2), and two CCD cameras (C4 and C5) [9]. The electrons acquire an angular kick from the magnetic dipole. Then, as the electrons pass through the air gaps they emit Cherenkov radiation, which is imaged by the cameras. The positions of the two air gaps correspond to low and high dispersion. One of the positions has higher energy resolution (A2), and the other has a broader energy range (A1) [29]. The combination of the two air gaps allows for the correction of an error in the experiment. Electrons are found to exit the plasma with a significant transverse angular deflection, θ_0 [9]. This angular deflection is created by a transverse offset of the back of the drive bunch

from the front. At one air gap, the angular deflection could be confused with the deflection of the magnetic dipole, which would cause energy measurement errors. However, since the electrons are measured on two air gaps, both the angular kick from the plasma and from the dipole are simultaneously determined. Figure 4.18 displays an illustration of this spectrometer.

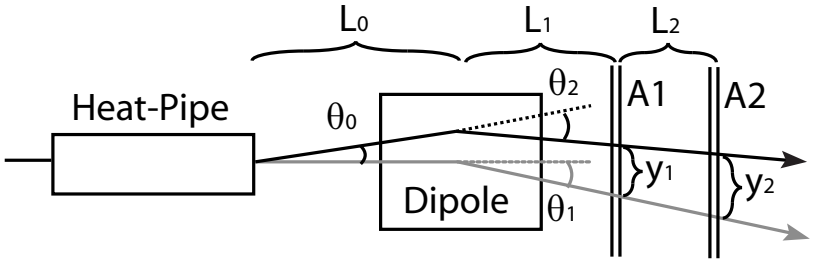

Figure 4.18: The large dipole energy spectrometer, where the gray line represents the trajectory of a 42 GeV electron in the absence of the heat-pipe oven.

Two linear equations follow from the geometry of the setup in Fig. 4.18:

$$y_1 = \theta_0(L_0 + L_1) + \theta_1 L_1 - \theta_2 L_1, \tag{4.25}$$

$$y_2 = \theta_0(L_0 + L_1 + L_2) + \theta_1(L_1 + L_2) - \theta_2(L_1 + L_2). \tag{4.26}$$

The solution of these equations for θ_2 is

$$\theta_2 = \theta_1 + \frac{y_1(L_0 + L_1 + L_2) - y_2(L_0 + L_1)}{L_0 L_2}. \tag{4.27}$$

Equation 4.24 yields θ_1 from the nominal energy of the bunch (42 GeV) and the $\int B_x dz$ setting of the magnet. A measurement of the distances y_1 and y_2 results in the determination of the angular deflection imparted to the electrons from the dipole, which is related to its energy by Eq. 4.24. The highest energy electrons measured in the experiment had an energy of 85 GeV. These electrons received an angular kick equal to 4.2 mrad from the dipole. The angular kicks from the plasma occurred, at times, in excess of 0.5 mrad, making energy measurement corrections from this two screen method necessary for the highest energy electrons.

The trapped electrons appeared with energies up to 30 GeV, which corresponds to an angular kick from the dipole of 12 mrad. This makes the corrections from the

plasma angular kicks less significant for the trapped electrons. For this reason and to make use of the full broad energy range of A1, only this screen is used for the trapped electrons. The dipole disperses electrons in the y direction according to their energy, which allows for the measurement of the x rms size in the air gap, σ, as a function of energy. For most of the experiment the dipole has $\int B_x dz = 1.2$ or 0.27 Tm; however, for several data sets the dipole strength is varied, where it has a minimum value of $\int B_x dz = 0.016$ Tm. The corresponding minimum measurable energies are 11, 2.3, and 0.14 GeV, respectively.

As is shown in Ch. 5, the spatial resolution of A1 is important. Two terms account for the resolution limit of the system: the resolution of the camera and the resolution limit from multiple Coulomb scattering in the various elements traversed by the electrons from the plasma to A1 [36]. Camera resolution is measured by imaging a back illuminated 5 μm pinhole that is located 2.5 m from the camera, just as in the experiment. In addition, a mask is placed over the camera lens to simulate a Cherenkov ring. This mask is translated along the lens to simulate the fact that the Cherenkov rings from different energy electrons hit the camera lens at different positions. Also, the finite thickness of the air gap is simulated by translating the camera towards and away from the pinhole by a length equal to that of the air gap. These measurements give the camera resolution limit as a function of the position on the camera, which is translated to a resolution limit versus energy.

There are several multiple Coulomb scatterers in between the plasma and the spectrometer, so even a bunch that initially has zero transverse emittance inside the plasma would acquire a finite size at A1. The resolution limit of the system due to multiple Coulomb scattering is the calculated size at A1 for a bunch that initially has zero divergence and size. This size is calculated from the angular scatter of each element and its distance to the spectrometer. A summary of the scatterers in the system, along with their distances from the spectrometer and their thicknesses, follows. At 193 cm, is a 75 μm beryllium foil; at 166 cm, is another 75 μm beryllium foil; at 4 cm, is a 50 μm stainless steel foil; at 7.5 mm, is a 420 μm silicon wafer. The total resolution of the system is the addition of the camera and multiple Coulomb scattering resolutions in quadrature. Figure 4.19 displays the total resolution of the system for two different integrated magnetic field settings.

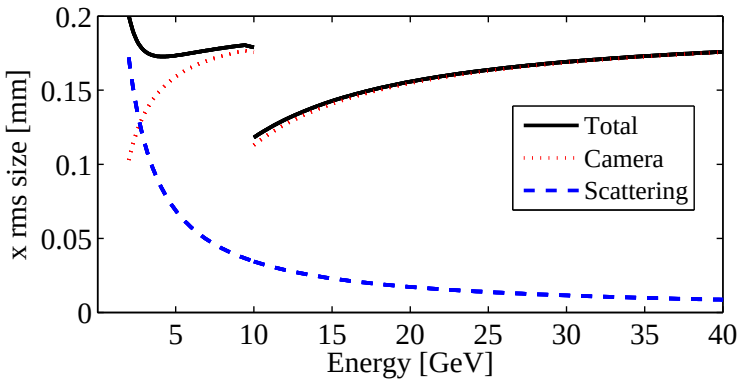

Figure 4.19: The transverse size resolution for the first screen of the large dipole spectrometer, A1, due to multiple Coulomb scattering and the camera resolution. Above 10 GeV the resolution limit for $\int B_x dz = 1.2$ Tm is shown, and below 10 GeV the resolution limit for $\int B_x dz = 0.27$ Tm is shown. Reprinted with permission from [36]. Copyright 2007, Institute of Electrical & Electronics Engineers.

4.5 Longitudinal Phase Space Determination

The energy spectra from the X-ray chicane are used in conjunction with LiTrack simulations to determine the longitudinal phase space for the drive bunches. A discussion of this determination follows. In the experiment, variations in the SLAC linac parameters produce variations in the longitudinal current profile and energy spectrum of the drive bunches. LiTrack simulations are performed over the expected range of variation for these parameters (see Tbl. 4.2). This simulation base yields a longitudinal current profile and energy spectrum for each set of linac parameters. A least-square fit of the LiTrack energy spectra to an experimental energy spectrum yields the parameters of the linac which best represent the experimental event and the corresponding longitudinal phase space. Figure 4.20 displays several examples of LiTrack fits to experimental events.

Figure 4.21 displays the sum of the squared difference between the LiTrack energy spectra and an experimental energy spectrum plotted versus the LiTrack peak current. As the least-square difference decreases, the LiTrack simulations converge to a single value in peak current. Thus, the drive bunch's energy spectrum is uniquely related to its longitudinal peak current.

As discussed in Sec. 4.4.4, the pyroelectric detector is used as a qualitative bunch

Variable	Value and Range	Units
Initial Number of Electrons	1.75 : 0.05 : 2.00	10^{10}
Initial Bunch Length, σ_z,	5.5 : 0.1 : 5.8	mm
Initial Bunch Asymmetry	0.230 : 0.010 : 0.260	dimensionless
Initial Bunch Position	-1.8 : 0.15 : 0	mm
U_0 of the Compressor Cavity	41.5 : 0.1 : 42.8	MeV
Energy Acceptance of the RTL	0.02 : 0.005 : 0.03	$\delta E/\langle E \rangle$
ϕ_{ramp}	-2.55 : 0.15 : 0.6	degrees

Table 4.2: The values and ranges of the SLAC linac parameters.

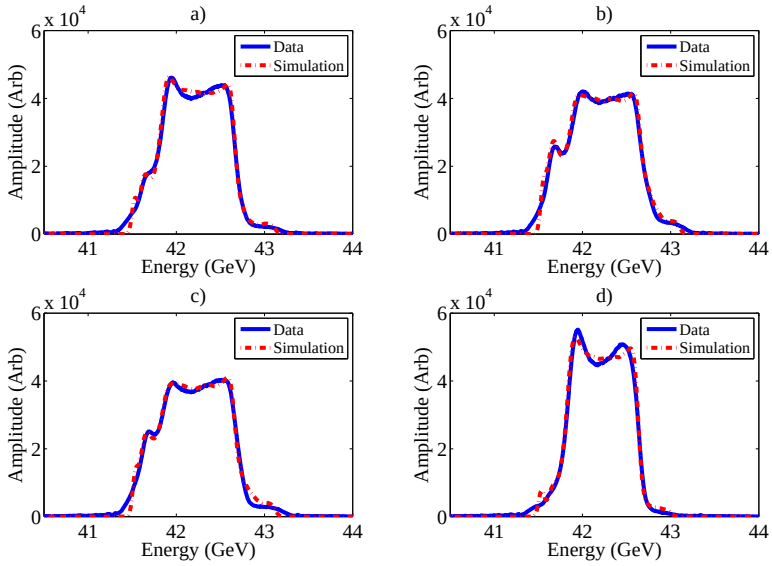

Figure 4.20: A few randomly chosen examples of LiTrack matches to data, courtesy of I. Blumenfeld.

length measurement. In addition, the pyroelectric detector is paired with LiTrack simulations to produce a quantitative bunch length measurement. The LiTrack matching for a single set of data is used to determine an empirical relationship between the pyroelectric detector signal and the drive bunch peak current. Note, the data contained in this dissertation came from experiments in August of 2005 and April of 2006. As the experimental setups were not identical, the exact relationship between the pyroelectric detector signal and the peak current differ. Figures 4.23 and 4.22 display the pyroelectric detector signal dependence on the drive bunch peak current for April 3$^{\text{rd}}$ of 2006 and August 14$^{\text{th}}$ of 2005, respectively, as measured with LiTrack matching.

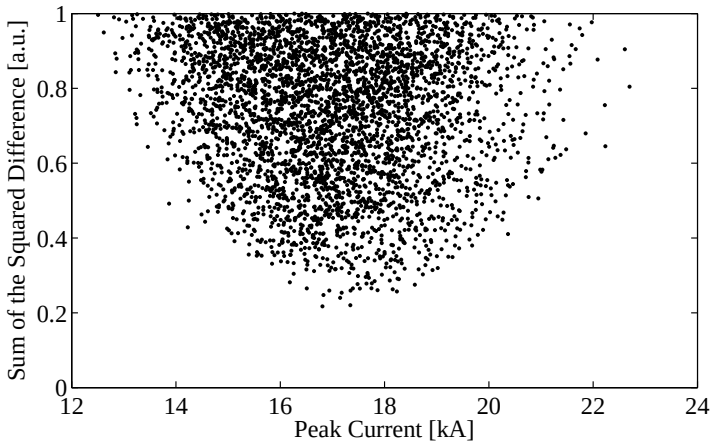

Figure 4.21: The sum of the squared difference between the LiTrack energy spectra and an experimental energy spectrum plotted versus the LiTrack peak current. This demonstrates the uniqueness of LiTrack matching.

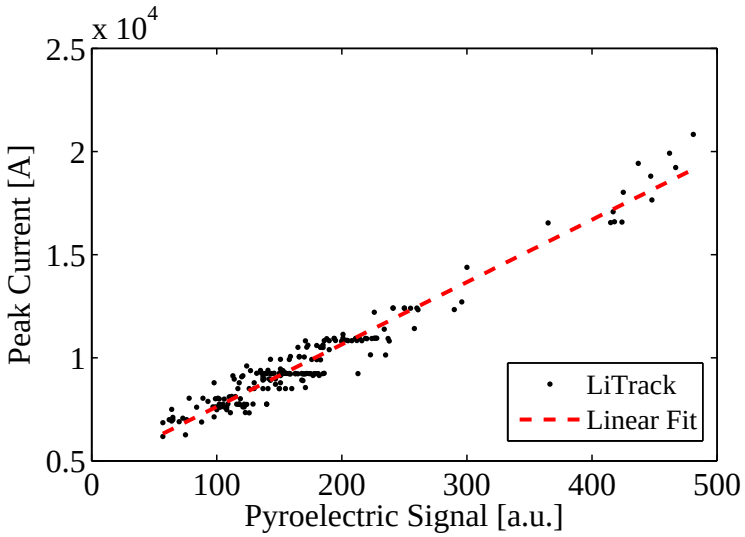

Figure 4.22: The drive bunch peak current versus the pyroelectric signal on August 14$^{\text{th}}$ of 2005, where LiTrack matching determined the peak current.

LiTrack matching is time consuming, so this data is used to determine a drive bunch's peak current, I_d, from the pyroelectric detector signal, *pyro*. The fit for April 3$^{\text{rd}}$ of 2006 yields

$$I_d = 41.3 \cdot pyro + 6330, \tag{4.28}$$

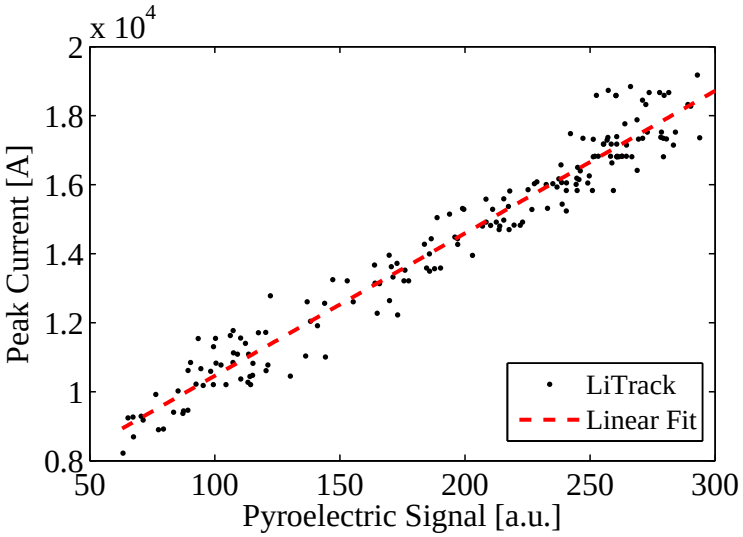

Figure 4.23: The drive bunch peak current versus the pyroelectric signal on April 3rd of 2006, where LiTrack matching determined the peak current.

and the fit for August 14^{th} of 2005 yields

$$I_d = 30.2 \cdot pyro + 4600, \tag{4.29}$$

where I_d is in units of Amps.

Chapter 5

Experimental Results

5.1 Introduction

This chapter presents experimental measurements of the onset in plasma electron trapping and of the trapped electron bunch properties. The onset of trapping is monitored with charge measuring toroids that are up- and downstream of the heat-pipe oven. A measurement of more charge exiting the heat-pipe oven than went into it indicates that plasma electrons were trapped in the drive bunch's wake. Systematic variations of the plasma density and the drive bunch parameters demonstrate the dependence of the onset in electron trapping on these quantities. In addition, a combination of the experimental diagnostics, presented in the previous chapter, yield a general picture of the six-dimensional ($\overrightarrow{x}$ and $\overrightarrow{p}$) distribution of the trapped electrons.

5.2 Overview of PWFA Experimental Results

Plasma electron trapping was auxiliary to the main thrust of the PWFA experiments, which was to examine the basic propagation and acceleration properties of plasma wakes driven by intense electron drive bunches. Before proceeding to the trapped electron measurements it is important to present an overview of the other results achieved within the same set of experiments.

Earlier experiments demonstrated the basic focusing properties of the ion bubble

[56] and the scale of the fields in a PWFA [26]. The most recent set of experiments investigated these properties with a plasma column that was long enough to drive the minimum energy of the drive bunches to near zero (meter scale). Although these experiments did not reach complete energy depletion, they did achieve the significant milestone of energy doubling for some of the electrons in the back of the drive bunch [9] (see Fig. 5.1).

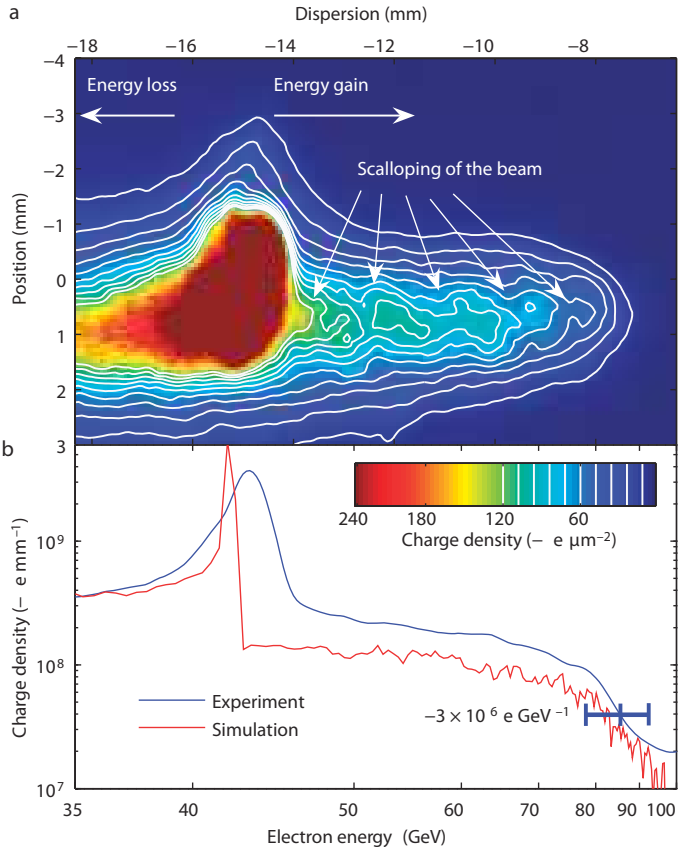

Figure 5.1: Energy doubling of 42 GeV electrons. a) An image from A2 of the large dipole spectrometer. b) The measured energy spectrum of the drive bunch compared to a QuickPIC simulation of the experiment. Reprinted by permission from Macmillan Publishers Ltd: Nature (**445**, 741), copyright (2007).

As a drive bunch propagates through plasma, the ionization front recedes into the bunch and causes the head of the bunch to erode (see Fig. 5.2a and Sec. 1.5.5). Head erosion kept the maximum energy of the drive bunch electrons from extending beyond energy doubling. During the experiment, the erosion was fast enough to cause the

location of the decelerating part of the plasma wake to slip to the former location of the accelerating part of the wake. As displayed in Fig. 5.2b, this caused the maximum observed energy in the experiment to decrease as the plasma oven length increased beyond 85 cm.

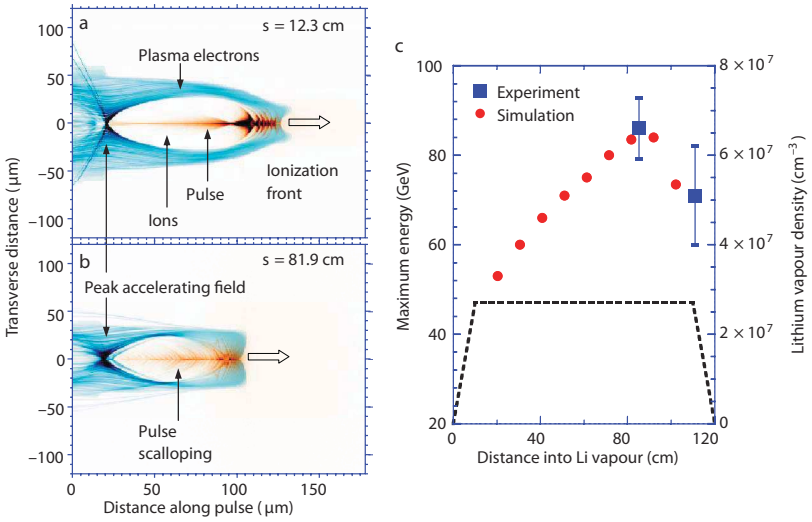

Figure 5.2: Head erosion of a 42 GeV electron bunch. a) The plasma wake at the beginning of the heat-pipe oven and b) after a significant amount of head erosion has occurred (from a QuickPIC simulation). c) The maximum energy of electrons measured in the experiment and from the simulations at the experimental measurement threshold versus propagation length. Reprinted by permission from Macmillan Publishers Ltd: Nature (**445**, 741), copyright (2007).

In addition to the useful propagation properties of the plasma wake, the strong focusing of the ion bubble causes the emission synchrotron radiation from the drive bunch electrons. The energy that a drive bunch electron loses to synchrotron radiation, W_{loss}, per unit length is

$$W_{loss} = \frac{4\pi^2}{3} mc^2 r_e^3 n_p^2 \gamma^2 r_0^2, \tag{5.1}$$

where r_0 is the maximum radius of the electron. A set of experiments found that this radiation consists of photons with tens of MeV in energy, which could be used with a target as a positron source for high energy colliders [30].

5.3 Onset of Plasma Electron Trapping

Earlier experiments first observed plasma electron trapping in a PWFA and identified the underlying trapping mechanism, ionization induced electron trapping [58]. These experiments focused on the longitudinal electric field in the plasma wake required to cause the onset of electron trapping. At a plasma density of $1.6{\cdot}10^{23}$ m^{-3}, they observed a sudden onset in electron trapping for an average drive bunch energy loss above 0.9 GeV. This average energy loss value was linked, using simulations, to a 36 GV/m accelerating field at the back of the wake.

Instead of using simulations to connect the onset of trapping to the maximum accelerating field, the onset can be directly related to the maximum decelerating field sampled by the drive bunch. The maximum energy lost by the drive bunch electrons divided by the length of the plasma is a measurement of this maximum decelerating field. A change in the amount of longitudinal compression on the drive bunch varies the bunch's peak current and the value for the maximum decelerating field. Figure 5.3 displays the number of trapped electrons versus the maximum decelerating field, where the number of trapped electrons results from the subtraction of the amount of charge measured in an upstream toroid from a downstream one. As discussed in Sec.

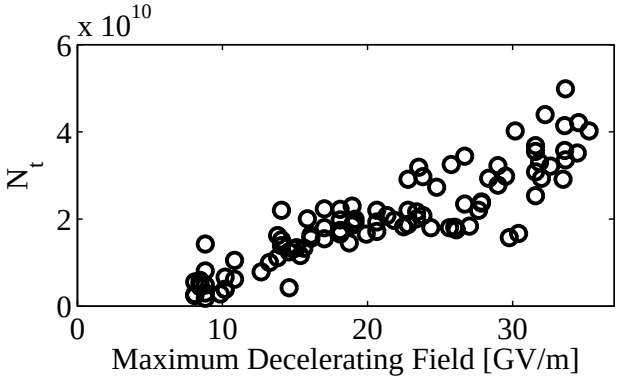

Figure 5.3: The number of trapped electrons, N_t, versus the maximum decelerating field. An onset in electron trapping occurs above a decelerating field of 10 GV/m.

2.4, longitudinal accelerating fields of order $mc\omega_p/e$ are required to initiate electron trapping. The data in Fig. 5.3 corresponds to a plasma density of $2.7 \cdot 10^{23}$ m^{-3}, where $mc\omega_p/e = 50$ GV/m. This data shows that the threshold for trapping occurs below $mc\omega_p/e$ at a value of 10 GV/m ($0.2 \cdot mc\omega_p/e$). Note, the scale calculation in

Sec. 2.4 treats the distance from the center of the ion bubble to the back as $1/k_p$. This distance actually exceeds $1/k_p$, which allows trapping to occur at field strengths below $mc\omega_p/e$. In simulations the onset of electron trapping occurs at a similar decelerating field. Recall Fig. 2.5, which showed an onset of trapping at $I_d = 8.62$ kA ($\approx I_A/2$). The maximum decelerating field experienced by the core of the drive bunch in this simulation is $0.21 \cdot mc\omega_p/e$.

The drive bunch and plasma properties are the controllable experimental parameters, so it is important to focus on the onset of trapping with these parameters. Chapter 2 derives the requirements on the drive bunch to cause the onset of plasma electron trapping: the drive bunch must at least have a critical number of electrons, $N_{crit} = 1/(k_p r_e)$, and a critical peak current, $I_{crit} = ec/(2r_e) \approx 8.5$ kA. At a plasma density of $2.7 \cdot 10^{23}$ m^{-3}, where most of the experiment took place, $N_{crit} = 3.6 \cdot 10^9$. In the experiment, the drive bunches had a fixed number of electrons equal to $1.8 \cdot 10^{10}$ ($5N_{crit}$); however, they had a variable peak current on the order of I_{crit}. A variation in the amount of longitudinal compression on the drive bunch produces peak currents that extend above and below I_{crit}. Figure 5.4 displays the number of trapped electrons versus the drive bunch peak current. This data shows that the onset in electron trapping occurs at the theoretically predicted value of $I_d = I_{crit} \approx 8.5$ kA.

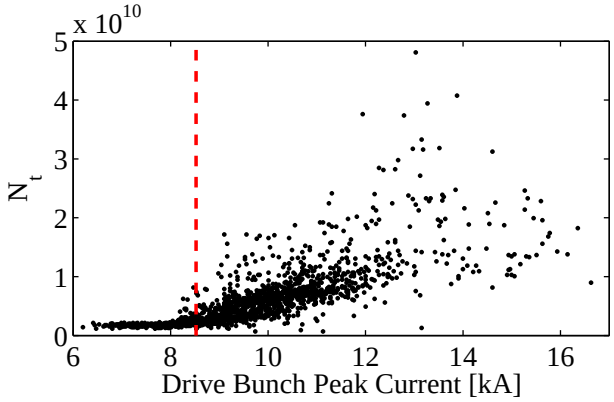

Figure 5.4: The number of trapped electrons, N_t, versus the drive bunch peak current. An onset in electron trapping occurs above a peak current of $I_A/2$ (denoted by the red dotted line).

There was also an onset in electron trapping measured versus plasma density. Figures 5.5 and 5.6 display this onset for drive bunches with peak current from 12

to 14 kA and 15 to 17 kA, respectively. Note, the data contained in these plots was taken in conjunction with the experiment on gamma ray production [30]. Recall from Eq. 5.1 that more radiation results from larger oscillations of the drive bunch electrons (larger r_0). Thus, the signal in the gamma ray production experiment was maximized with drive bunches that have large transverse sizes in the plasma. This is an important fact needed to explain the onset of electron trapping versus plasma density.

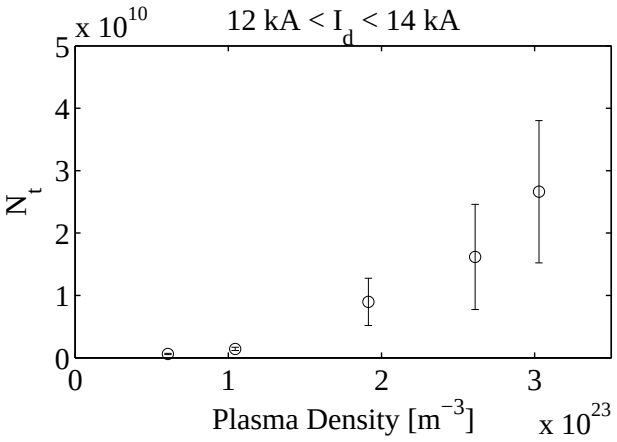

Figure 5.5: The number of trapped electrons, N_t, versus plasma density for drive bunches with I_d in the range of 12 to 14 kA, where error bars denote a standard deviation of the data points.

A properly matched transverse size for the drive bunch's transverse normalized emittance of $\epsilon_{N,x} = 60$ μm is of order $\sigma_x \approx 2$ μm (and is smaller in y). However, more gamma rays result from a larger transverse size, so the drive bunches that correspond to the data (Figs. 5.5 and 5.6) were purposely mismatched. At the entrance to the heat-pipe oven, the drive bunches were focused transversely to a size of 10 μm. While a properly matched bunch would be focused further by the roll-up in plasma density, a purposely mismatched bunch could have a transverse size of 10 μm or larger. Recall Eq. 2.31; the maximum electric field for a drive bunch with $\sigma_x = 10$ μm and $I_d = 12$ kA is 32.5 GV/m, which is of the same order as $mc\omega_p/e$ for these plasma densities (30.4 GV/m for $n_p = 10^{23}$ m^{-3}). Also, recall E_z from Fig. 1.2; this shows E_z reaches $3 \cdot mc\omega_p/e$ at the back of the bubble. Thus, the maximum magnitude of the electric field in this system is some factor of order unity times $mc\omega_p/e$.

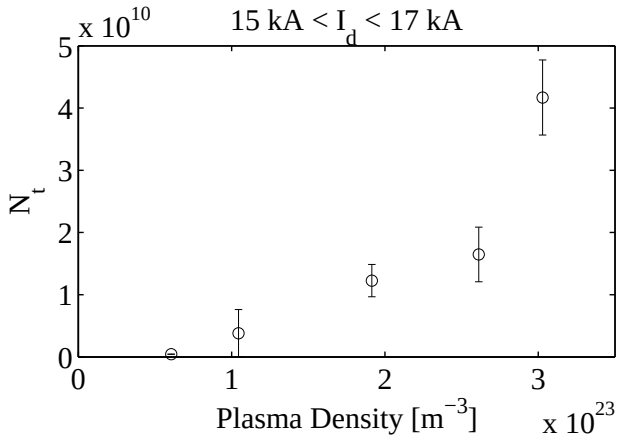

Figure 5.6: The number of trapped electrons, N_t, versus plasma density for drive bunches with I_d in the range of 15 to 17 kA, where error bars denote a standard deviation of the data points.

Near the plasma density range of Figs. 5.5 and 5.6, the ionization rate of helium from an electric field of $mc\omega_p/e$ becomes on the order of ω_p. For densities significantly below this range, $\Gamma(mc\omega_p/e) \ll \omega_p$, so helium atoms would not become ionized in the wake. Thus, trapping would not occur. Figure 5.7 further illustrates this point. This figure shows the probability of helium ionization for several electric fields near $mc\omega_p/e$ over a time of $1/\omega_p$ versus plasma density. At the point of the onset in electron trapping, the fields in the system become large enough to ionize helium. Thus, this is the reason for the onset of electron trapping versus plasma density.

The onset of electron trapping at a plasma density of 10^{23} m^{-3} is not intrinsic to the PWFA, but is due to the large transverse size of the drive bunches in this data set. If the drive bunches had matched transverse sizes, they would have ionized helium without the aid of the plasma fields. For example, compare the locations of the onset in electron trapping for Figs. 5.5 and 5.6. The drive bunches with I_d from 15 to 17 kA (Fig. 5.6) had larger transverse electric fields than those with I_d from 12 to 14 kA (Fig. 5.5), which caused the onset of electron trapping at a lower plasma density.

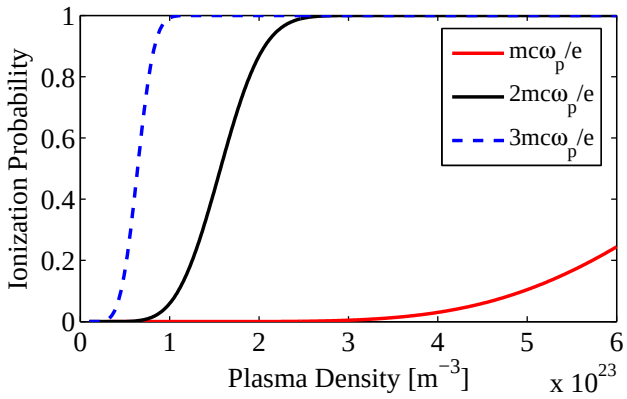

Figure 5.7: The probability of helium ionization from the electric fields of $|E| = mc\omega_p/e$, $2 \cdot mc\omega_p/e$, and $3 \cdot mc\omega_p/e$ over a time of $1/\omega_p$ $(1 - \exp[-\Gamma(|E|)/\omega_p])$ versus plasma density, where the ionization rate is calculated with Eq. 2.19.

5.4 Trapped Electron Bunch Properties

A combination of the spectra from the large dipole and the low energy mask spectrometers creates a total momentum spectrum for the trapped electrons. In addition, the transverse size of a trapped electron bunch on the large dipole spectrometer is a measurement of the bunch's transverse emittance over peak current. This measurement is combined with insights from simulations to yield an upper limit for the transverse emittance of the trapped electron bunch.

5.4.1 Trapped Electron Momentum Spectrum

The dispersion of the small dipole magnet allows the mask to collect electrons below a momentum cutoff and the toroid to measure the total number of electrons with momentum above the cutoff [34]. Figure 5.8 displays the number of electrons measured by the toroid versus the momentum cutoff. This data shows that a large amount of this charge is at or below a momentum of 10 MeV/c. These very low energy electrons originate from the downstream transition region of the heat-pipe oven.

The low energy mask spectrometer had a maximum momentum cutoff at around 200 MeV/c, so the large dipole energy spectrometer was required to measure the electrons of higher energies. Many of the measurements for the trapped electron properties came from this high energy spectrometer. As mentioned in the previous

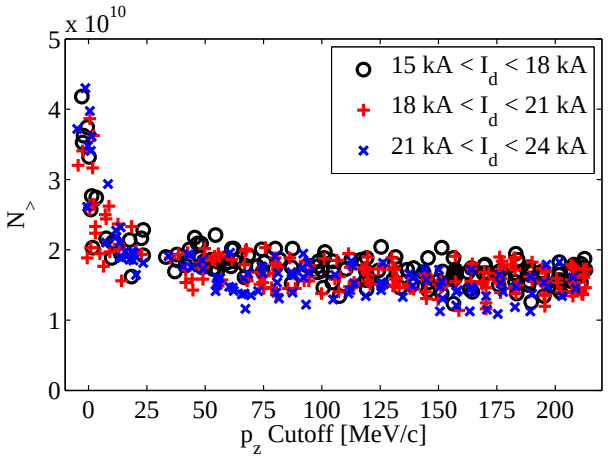

Figure 5.8: The number of trapped electrons with momentum above the cutoff, $N_>$, versus the momentum cutoff, from the low energy mask spectrometer. The various data markers denote different ranges in the drive bunch peak current. This data corresponds to a plasma density of $2.7 \cdot 10^{23}$ m^{-3} and a plasma FWHM length of 85 cm.

chapter, the large dipole spectrometer images the dispersion of the electrons from the Cherenkov radiation that they emit through air gaps. The accelerating and decelerating fields were of order 50 GV/m and the plasma had a FWHM length of 85 cm, so the trapped electrons were accelerated to energies comparable to the decelerated electrons from the drive bunch. This places some of the trapped electrons at the same location in the spectrometer as the drive bunch electrons. Before progressing further into the measurement of the trapped electrons on the large dipole spectrometer, it is important to first present how the trapped electrons are distinguished from the drive bunch electrons.

Figure 5.9 displays a typical large dipole spectrometer image. In addition to the signature for energy loss on the drive bunch, when I_d approaches $I_A/2$, narrow electron streaks appeared in the spectrometer images [34]. Since the streaks had energies lower than the initial drive bunch energy (42 GeV), they were the result of either the wake accelerating plasma electrons from 0 GeV or decelerating drive bunch electrons from 42 GeV. A variation of the drive bunch longitudinal length changed the magnitude of E_z in the wake. Figures 5.10a and 5.10b show that as stronger plasma wakes decreased the minimum energies of the drive bunches, the maximum

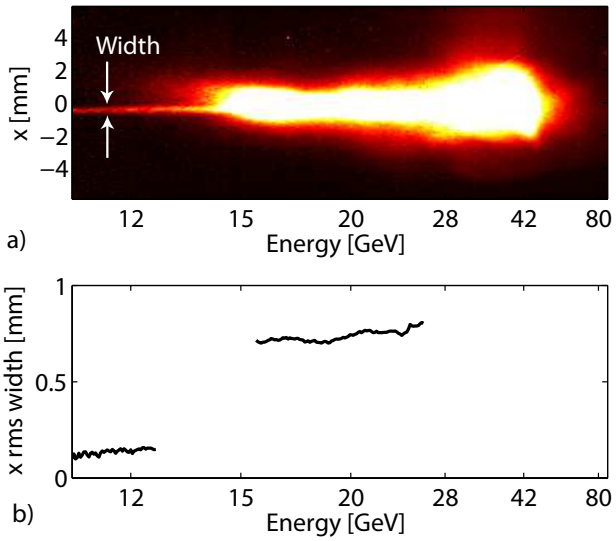

Figure 5.9: a) An image from the large dipole energy spectrometer, viewed with a saturated color map. b) Root mean square x width in the spectrometer image versus energy. The thinnest part of the streak was determined to be trapped plasma electrons, while the wider part consists of drive bunch electrons. Reprinted with permission from [36]. Copyright 2007, Institute of Electrical & Electronics Engineers.

energies of the electron streaks increased, so the streaks were in the accelerating part of the wakes. Thus, the streaks were trapped plasma electrons.

For most of the experiment the large dipole had $\int B \cdot dl = 1.2$ or 0.27 Tm; however, for several data sets the dipole strength was varied, where it had a minimum value of $\int B \cdot dl = 0.016$ Tm. The corresponding minimum measurable energies for these values of $\int B \cdot dl$ are 11, 2.3, and 0.14 GeV, respectively. A combination of the measurements from these three magnet settings results in a momentum spectrum for the trapped electrons from just above 200 MeV/c to 10 GeV/c. Trapped electrons also appeared with momentum above 10 GeV/c; however, their maximum momentum was at times greater than the minimum momentum of the drive bunch. This placed the trapped electron streak on top of the drive bunch electrons in the spectrometer images. To avoid the inclusion of drive bunch electrons in the trapped electron momentum distribution, only data points below a momentum of 10 GeV/c are incorporated in the distribution. Figure 5.11 displays the trapped electron momentum distribution

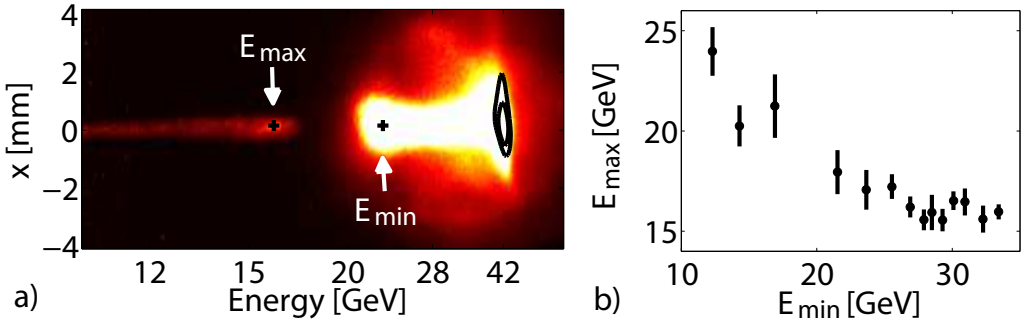

Figure 5.10: a) A saturated image from the energy spectrometer, where the black contour lines show the drive bunch spot size in the absence of plasma acceleration. Trapped electrons appeared as streaks with rms x sizes that were much smaller than that of the drive bunch. The black plus signs denote the maximum energy of the electron streak, E_{max}, and the minimum energy of the drive bunch, E_{min}, after accounting for the natural spot size of the electron bunches [10]. b) The quantity E_{max} versus E_{min}, where the difference between the streak and drive bunch x rms size allows for a measurement of E_{max}, even when it extends above E_{min}. Reprinted with permission from [39]. Copyright 2009, American Physical Society.

from the large dipole spectrometer for several ranges of drive bunch peak current.

A combination of the data from the mask spectrometer and the large dipole spectrometer yields a total momentum spectrum of the trapped electrons. However, the raw data from the mask spectrometer must first be converted to a momentum spectrum. The momentum spectrum for the trapped electrons is given by the derivative in p_z of the raw data from the mask spectrometer. Instead of taking the derivative of raw data, the data is first fit and then differentiated with respect to p_z. The spectra resemble lines in a logarithmic plot, so a power law is a natural assumption for the fit. Equation 5.2 displays the assumed form of this power law.

$$N_{>} = A p_z^{\beta}, \tag{5.2}$$

where $N_{>}$ is the number of electrons above a momentum of p_z. A Hall probe that was inserted into the small magnetic dipole determined the momentum cutoff. This probe was calibrated to known integrated magnetic field settings. The normal error in this measurement was 2.4 MeV/c. Thus, to avoid fitting errors, only data points with momentum greater than 5 MeV/c are included in the fits. These fits of $N_{>}$ are

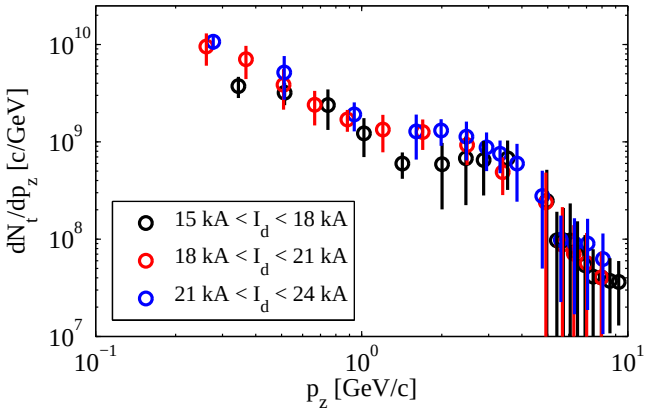

Figure 5.11: The spectral density of the trapped electron, dN_t/dp_z, versus momentum, p_z, for several different ranges of drive bunch peak current, from the large dipole spectrometer. Error bars denote a standard deviation of the spectral density. At times the standard deviation approached or exceeded the mean value, so the total ranges for some of these error bars are not plotted.

converted to a momentum density as follows.

$$dN_t/dp_z = -dN_>/dp_z = -\beta A p_z^{\beta-1}. \tag{5.3}$$

Figure 5.12 displays the total trapped electron momentum spectrum.

Electron trapping occurred at both the up- and downstream transition regions between helium and lithium; the electrons trapped in these different regions had different properties. As the drive bunch traversed the heat-pipe oven, electrons became trapped in small regions at the back of the accelerating portions of the wake. In the upstream boundary, the plasma wavelength shortened as the drive bunch traversed the boundary, but remained fixed inside the pure lithium region. Electrons trapped at densities significantly lower than $2.7 \cdot 10^{23}$ m^{-3} ended up in the decelerating part of the wake as the plasma wavelength shortened, so they did not remain trapped. This resulted in small longitudinal bunch lengths for the trapped electrons from the upstream transition region. In addition, these electrons accelerated throughout the 85 cm of lithium, so they reached high energies (≈30GeV). The same was not true for the trapped electrons from the downstream boundary. There, the plasma wavelength

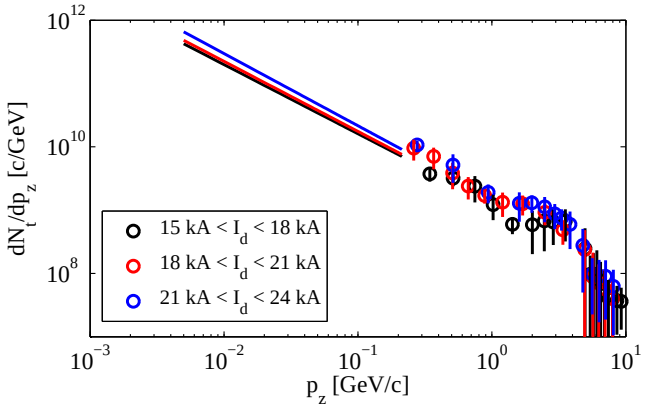

Figure 5.12: The spectral density of the trapped electron, dN_t/dp_z, versus momentum, p_z, for several different ranges of drive bunch peak current, from a combination of the large dipole spectrometer (data points) and the low energy mask spectrometer (solid lines). The linear trends from the mask spectrometer agree with that from the large dipole spectrometer.

increased as the drive bunch traversed the boundary. As this plasma wavelength increased, additional trapping occurred at the new position for the back of the wake, resulting in a relatively large amount of low energy charge with long longitudinal bunch lengths.

The measured maximum energy and total charge of the trapped electrons are evidence that electron trapping occurred in both transition regions. First, the accelerating field was of order 50 GV/m, so the high energy (30 GeV) trapped electrons must have accelerated through the plasma for on the order of a meter. Since the lengths of the transition regions were only a few cm, these high energy trapped electrons must have originated from the upstream region.

Now, consider the total charge of the trapped electrons. Figure 5.6 shows that the number of trapped electrons reached almost $6{\cdot}10^{10}$. As is discussed in Ch. 2 and is shown in Fig. 2.5, only a charge of scale $1/(k_p r_e)$ is required to completely load the wake and turn off further trapping. For $n_p = 2.7{\cdot}10^{23}$ m^{-3}, $1/(k_p r_e) = 3.6{\cdot}10^{9}$, which is much smaller than the measured trapped charge. Even considering the additional trapped charge that appears in multiple buckets (see Tbl. 3.1) does not account for the total amount of charge. Note, however, these simulations and discussions concern the loading of the wake when the plasma density is constant.

Since the trapped electrons from the upstream transition region accelerated through the full length of the plasma at a constant density, the loading arguments properly describe the amount of trapped electrons that originate from this region. However, as the drive bunch traversed the roll-off in plasma density at the downstream transition region, the plasma wavelength increased, which created additional trapping at the new position for the back of the bubble. This allowed the amount of trapped charge to exceed that expected for plasma of constant density. Thus, the total charge measured for the trapped electrons is evidence of trapping in the downstream region.

5.4.2 Cherenkov Cell Energy Spectrometer

Measurements of the trapped electrons were also made with the Cherenkov cell spectrometer. The data from this spectrometer corresponds to lithium vapor FWHM lengths of 13, 22.5, and 30.5 cm, a plasma density of $2.7 \cdot 10^{23}$ m^{-3}, and a drive bunch initial energy of 28.5 GeV. These relatively short plasma oven lengths kept the minimum energy of the drive bunch above the maximum energy for the trapped electrons, which allowed for the distinction between the two. The drive bunch peak current varied throughout the data runs, which changed the amount of trapped electrons. For about 50 % of the shots in the data runs, there appeared two distinct Cherenkov rings. One ring was from the drive bunch, and the other was from the trapped electrons. Figure 5.13 shows an example of the two rings. The lack of azimuthal symmetry in the Cherenkov rings indicates a lack of azimuthal symmetry in the bunches that produced the Cherenkov light.

Figure 5.14 displays the energy of the trapped electron Cherenkov ring versus plasma length. The energy of this ring scaled linearly with the plasma length, which indicates that the trapped electrons stayed at a fixed accelerating field in the plasma wake and that they did not slip relative to the drive bunch. Thus, these electrons were truly trapped.

The Cherenkov ring intensities were at least three orders of magnitude brighter than the rings from incoherent emission, which were measured from the drive bunch in the absence of the plasma oven. This meant that the distribution of both the drive bunch and the trapped electrons had a significant Fourier component at optical wavelengths along the direction of Cherenkov emission. Put in simpler terms, the

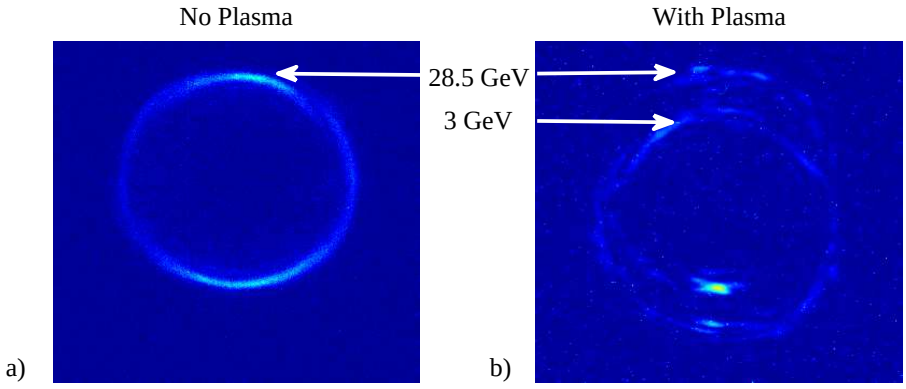

Figure 5.13: Images from the Cherenkov cell spectrometer with and without the plasma. Without the plasma only a drive bunch Cherenkov ring appeared.

drive and trapped electron bunches had sub-micron features. In this system, the characteristic length scales are the drive bunch dimensions and the plasma length scale. The drive bunch was focused to a transverse spot size of 10 μm and compressed longitudinally to about 20 μm at the entrance of the plasma [26]. In addition, the plasma length scale, $1/k_p$, was 10 μm. Thus, the bunch-plasma interaction produced sub-micron features in a system that was initially characterized by tens of μm.

5.4.3 Trapped Electron Divergence

The relationship between the trapped electron streak widths on the large dipole spectrometer and their emittance is found from an examination of the transverse propagation properties from the heat-pipe oven to the energy spectrometer. As will be shown later, ionization of helium in the buffer gas is an important effect to consider in this propagation; however, the first step in the analysis is to consider just the focusing forces from the lithium ions [36]. While exiting the plasma, the electrons traverse a roll-off in lithium density which creates a roll-off in the focusing forces of the plasma. A substitution of a variable plasma density into Eq. 1.27 yields a differential equation that describes the transverse evolution of the electrons through the roll-off:

$$\ddot{x} + \frac{n_p(z)e^2x}{2\epsilon_0\gamma mc^2} = 0, \tag{5.4}$$

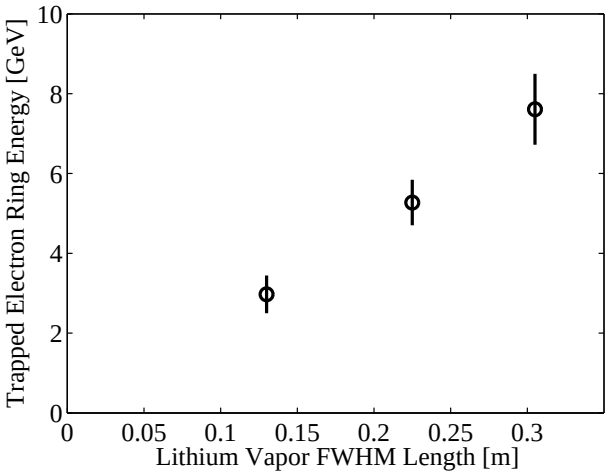

Figure 5.14: The energy of the trapped electron Cherenkov ring versus plasma length. The error bars denote a standard deviation in the ring energy at a given plasma length.

where dots represent derivatives in z, $n_p(z)$ is the ion density as a function of z, and $\dot{\gamma}$ is assumed to be zero. The density roll-off is fit well by a Gaussian with an rms width of $\sigma_p = 3.97$ cm. Thus, the following equation represents the transverse propagation through the roll-off.

$$\ddot{x} + K \exp(\frac{-z^2}{2\sigma_p^2})x = 0, \tag{5.5}$$

$$K = \frac{n_p e^2}{2\epsilon_0 \gamma m c^2}. \tag{5.6}$$

The propagation of the electrons from the beginning of the roll-off, $z = 0$, to the position of the air gap, $z = 3.04$ m, is described by a transfer matrix, R [13]. This transfer matrix determines the final transverse position, x_f, and the final transverse angle, $\dot{x}_f$, from the initial transverse position, x_0, and the initial transverse angle, $\dot{x}_0$:

$$\begin{pmatrix} x_f \\ \dot{x}_f \end{pmatrix} = R \begin{pmatrix} x_0 \\ \dot{x}_0 \end{pmatrix} = \begin{pmatrix} R_{11} & R_{12} \\ R_{21} & R_{22} \end{pmatrix} \begin{pmatrix} x_0 \\ \dot{x}_0 \end{pmatrix}. \tag{5.7}$$

The final transverse width at the spectrometer, $\langle x_f^2 \rangle$, is determined by the initial bunch properties and by the cosine-like term, $R_{11} = C$, and the sine-like term, $R_{12} =$

S, of the transfer matrix:

$$\langle x_f^2 \rangle = \langle x_0^2 \rangle C^2 + \langle x_0 \dot{x}_0 \rangle 2CS + \langle \dot{x}_0^2 \rangle S^2. \tag{5.8}$$

Equation 5.5 was solved numerically for C and S as a function of energy. Figure 5.15 displays C and $SK^{1/2}$ versus electron energy. As is to be expected, the cosine-like and sine-like terms are $\pi/2$ out of phase with each other.

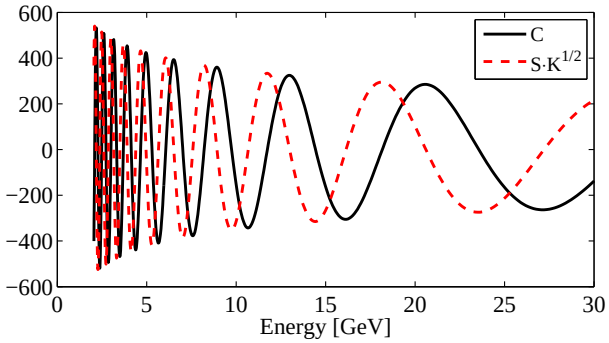

Figure 5.15: The cosine-like, C, and sine-like, S, (plotted as $SK^{1/2}$) terms of the transfer matrix from within the plasma to A1 of the large dipole spectrometer versus electron energy. Reprinted with permission from [36]. Copyright 2007, Institute of Electrical & Electronics Engineers.

From the oscillatory nature of C and S, shown in Fig. 5.15, a modulation in the streak widths as a function of energy might be expected; however, these widths did not exhibit such a modulation. Due to the sinusoidal natures of C and S, the only way for the width not to oscillate in energy is for the C^2 and S^2 terms (of Eq. 5.8) to have the same amplitude and for the amplitude of the CS term to be zero. Figure 5.15 shows that C and $SK^{1/2}$ have the same amplitude. Thus, the initial phase space of the trapped electrons satisfied the following criterion.

$$\langle x_0 \dot{x}_0 \rangle = 0. \tag{5.9}$$

$$\langle x_0^2 \rangle = K \langle \dot{x}_0^2 \rangle. \tag{5.10}$$

Recall from Eq. 1.45 that these are the definitions for a matched bunch. Therefore, the absence of an oscillation in the transverse width of the streaks versus energy is

evidence that the trapped electrons were matched to the plasma.

The conditions in Eqs. 5.9 and 5.10 are substituted into Eq. 5.8 to yield the relationship between the size on the diagnostic and the size in the plasma:

$$\langle x_f^2 \rangle = \langle x_0^2 \rangle (C^2 + KS^2). \tag{5.11}$$

Also, the conditions of Eqs. 5.9 and 5.10 are combined with the definition for transverse emittance to give the relationship between the emittance and the bunch size in the plasma. Then, this is inserted into Eq. 5.11 to yield the relationship between the transverse normalized emittance, $\epsilon_{N,x}$, and the transverse bunch size at the large dipole spectrometer:

$$\epsilon_{N,x} = \frac{\gamma K^{1/2} \langle x_f^2 \rangle}{C^2 + KS^2} \approx 0.0022 \mathrm{m}^{-1} \gamma^{1.06} \langle x_f^2 \rangle. \tag{5.12}$$

As displayed in Eq. 5.12, the factor in front of the bunch transverse size is fit well by a power law in γ. This fit was performed for γ greater than 4,000 and less than 60,000, which was the range over which the trapped electron transverse emittance was determined. Figure 5.16 displays a contour plot of the measurements for the transverse normalized emittance of the trapped electrons versus energy, as determined by Eq. 5.12. Recall that this measurement ignores the effects of helium ionization. The lowest emittances determined by this method extended below 1 μm. Note, the trapped electrons appeared with transverse sizes near the camera resolution [36]. Thus, as γ increases so do the measurements of $\epsilon_{N,x}$; this is a consequence of a fixed camera resolution instead of a property of the trapped electrons.

So far the propagation has only included the focusing forces of the Gaussian density roll-off in lithium ions, ignoring the effects of helium ionization [36]. Under this assumed propagation model, the trapped electrons appear to achieve emittances better than 1 μm with transverse sizes that are matched to the plasma. A comparison between these conclusions and measurements from the energy spectrometer results in self-consistency problems. Trapped electron bunches that have matched transverse sizes for μm level emittances and the amount of charge indicated on the energy spectrometers could ionize helium, which makes the assumed Gaussian quadrupole focusing model invalid.

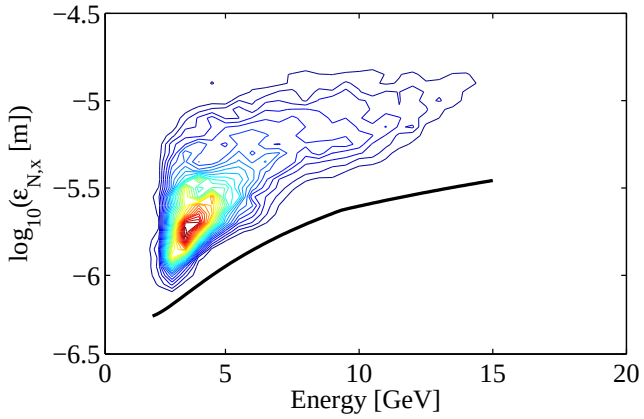

Figure 5.16: The measured transverse normalized emittance of the trapped electrons versus energy, ignoring the effect of helium ionization. The black line represents the system resolution.

The following sections show how the measurement of the trapped electron bunch properties changes in the presence of helium ionization. First, there is an overview of the requirements to ionize helium. Then, simulations and charge measurements from the energy spectrometer combine to show that the trapped electrons satisfied these requirements. Finally, upper bounds on the transverse size and divergence of the trapped electron bunches, at the point they started to diverge freely, yield an upper limit measurement of the transverse emittance over the peak current for these bunches [37, 39].

Ionization depends heavily on the applied electric field: small increases in the electric field lead to large increases in the ionization rate [1, 14]. The probability of ionization depends on the ionization rate and the duration of the applied field. Gaussian bunches with $\sigma_z = 0.5$, 1.9, and 5 μm have a 0.5 probability of helium ionization with peak electric fields of 113, 95.7, and 86.1 GV/m, respectively. Despite an order of magnitude increase in the bunch length, from 0.5 to 5 μm, the electric field required for ionization only decreases by 24%. The peak electric field of an electron bunch with $\sigma_x = \sigma_y$ is proportional to I_t/σ_x, where I_t denotes the bunch's peak current. For a given longitudinal bunch length, the maximum transverse size capable of ionizing helium, σ_m, is proportional to the peak current: $\sigma_m = \alpha I_t$, where α is the proportionality constant when the ionization probability at the peak field position of

a Gaussian bunch is equal to 0.5. Due to the high sensitivity of the ionization rate to the electric field, the quantity α is only weakly dependent on the bunch length: for $\sigma_z = 0.5$,1.9, and 5 μm, $\alpha = 2.39$, 2.83, and $3.14 \cdot 10^{-10}$ m/A, respectively.

Three-dimensional OSIRIS [22] simulations provided the basic length scale of the trapped electrons in the experiment. These simulations were for Gaussian drive bunches with $1.8 \cdot 10^{10}$ electrons, $\sigma_{x,y} = 1.74$ μm, σ_z varied from 10 to 50 μm in 10 μm steps, and represent the experimental drive bunches. The lithium density was $2.7 \cdot 10^{23}$ m^{-3}, with a small background helium density of $8.1 \cdot 10^{21}$ m^{-3}. In x, y, and z, the simulation grid size was 1/2 μm with either 2 or 4 particles per cell. Second order particle shapes were used to reduce numerical noise [20]. The trapped electron bunches had longitudinal FWHM lengths ranging from 2.7 to 6.3 μm, which correspond to Gaussian bunches with $\sigma_z = 1.1$ and 2.7 μm, respectively. Since $\sigma_z = 1.9$ μm is in the middle of the simulation range, the corresponding value of $\alpha = 2.83 \cdot 10^{-10}$ m/A is most appropriate for describing the experiment. Note, the simulations did not include the Gaussian roll-offs of the heat-pipe oven, so the longitudinal characteristics from the simulations are only representative of the trapped electrons from the upstream boundary.

A combination of the emittance measurements (from Fig. 5.16), simulation results, and charge measurements of the upstream trapped electrons shows that the trapped electron bunches could ionize helium [37]. The total momentum spectrum (see Fig. 5.12) includes trapped electrons from both the up- and the downstream transition regions, but the latter could not reach energies as high as the former. Let E_m denote the maximum energy achievable for the downstream trapped electrons. An integral of the accelerating field scale, $mc\omega_p/e$ ($\sqrt{mc^2 n_p(z)/\epsilon_0}$), over the downstream lithium density profile yields E_m as

$$E_m = e\sqrt{mc^2 n_p(z_0)/\epsilon_0} \int_{z_0}^{\infty} \exp(\frac{-(z-z_0)^2}{4\sigma_L^2}) dz = 3.5 \text{ GeV}. \tag{5.13}$$

As the plasma wavelength increases, the position of the maximum accelerating field changes. Equation 5.13 ignores this effect, but is still useful for setting the scale for E_m. The integration of the trapped electron energy profiles above 3.5 GeV yields a lower limit for the total amount of trapped charge from the upstream boundary. For

drive bunch peak currents in the intervals of 8.3 to 11.0, 11.0 to 13.2, 13.2 to 15.1, 15.1 to 16.8, and 16.8 to 18.4 kA, the trapped bunch from the upstream transition region had more than 1.34, 1.67, 1.65, 1.90, and $2.06{\cdot}10^9$ electrons, respectively. The matched transverse size for a 3.5 GeV electron bunch with $\epsilon_{N,x} = 1.0$ μm is 0.42 μm at a plasma density of $2.7 \cdot 10^{23}$ m^{-3}. Recall that a bunch can ionize helium if $I_t > \sigma_x/\alpha$. Therefore, a Gaussian bunch with $1.34{\cdot}10^9$ electrons and $\sigma_x = \sigma_y = 0.42$ μm can ionize helium for $\sigma_z < 17$ μm, which is an order of magnitude larger than the simulations indicate. Thus, an analysis of the trapped electron properties when assuming no helium ionization yields the conclusion that the trapped electrons could ionize helium. This is a proof by contradiction of the helium ionization. In addition, the drive bunches, if properly matched to the plasma, were also capable of ionizing helium. Therefore, the helium buffer gas is an important factor to include in the propagation of the trapped electrons to the energy spectrometer.

In the presence of helium ionization, an upper limit measurement of $\epsilon_{N,x}/I_t$ results from the determination of upper bounds for the trapped electron bunch's transverse size and divergence at the point it started to diverge freely [37]. The trapped electrons diverged freely either before or when they reached the downstream beryllium window. Thus, the transverse size at the spectrometer air gap, σ, divided by the length from the beryllium window to this air gap, $L = 193$ cm, is an upper limit measurement of the angular divergence.

Ionization of helium created an ion bubble that was capable of confining the trapped electrons transversely in the helium buffer gas. Note, the driver of the helium wake was subject to head erosion: the front of the bunch did not experience a focusing field so it expanded, which caused the front of ionization to move further into the bunch [9]. As mentioned earlier, both the drive and trapped bunches were capable of ionizing helium. For the trapped electrons to have diverged before they reached the downstream beryllium window, the ionization front had to move through both the drive and trapped bunch. A bunch that was too large transversely to ionize helium would have diverged freely. Thus, the maximum transverse size for the trapped electron bunches at the point they started to diverge freely was $\sigma_m = \alpha I_t$.

Equation 5.14 expresses the transverse normalized emittance.

$$\epsilon_{N,x} = \gamma\sqrt{\langle x^2\rangle\langle \dot{x}^2\rangle - \langle x\dot{x}\rangle^2}. \tag{5.14}$$

Until the bunches began to diverge freely, the $x\dot{x}$ correlation term was small. An inequality then replaces Eq. 5.14:

$$\epsilon_{N,x} < \gamma\sigma_x\sigma_{\dot{x}}, \tag{5.15}$$

where $\sigma_{\dot{x}}$ represents the rms size of the bunch in $\dot{x}$. The substitution of σ_m and σ/L into this upper limit for emittance yields an upper limit measurement of $\epsilon_{N,x}/I_t$:

$$\frac{\epsilon_{N,x}}{I_t} < \frac{\gamma\alpha\sigma}{L}. \tag{5.16}$$

Figure 5.17 shows the measurement of $\epsilon_{N,x}/I_t$ from this equation, where contours represent the density of data points.

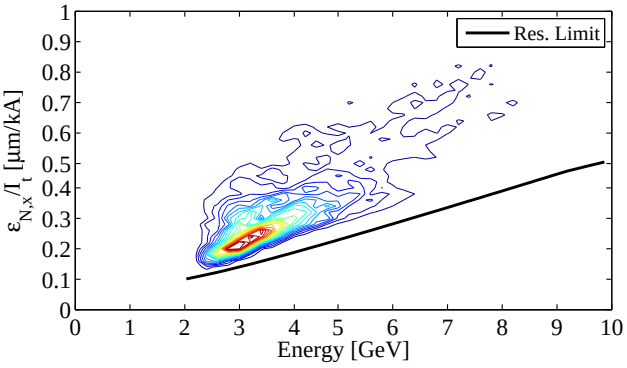

Figure 5.17: A contour plot of the measured upper limit for $\epsilon_{N,x}/I_t$ of the trapped electrons versus energy, obtained from Eq. 5.16, where the black line represents the system resolution. Reprinted with permission from [39]. Copyright 2009, American Physical Society.

5.4.4 Transverse Emittance and Peak Current

Information from simulations can turn the measurements of $\epsilon_{N,x}/I_t$ into upper and lower limits for the trapped electron transverse emittance and peak current, respectively [39]. Once enough electrons become trapped, they load the accelerating field and cease additional trapping. The OSIRIS simulations (presented in the previous section) ran until the trapped electrons loaded the wake and turned off further trapping, resulting in a maximum achievable trapped electron peak current, $I_{t,m}$. For I_d = 34.5, 17.2, 11.5, 8.62, and 6.90 kA, $I_{t,m}$ = 125, 80.3, 42.2, 17.3, and 2.60 kA, respectively. For more detail, consult Sec. 3.3.

From the simulated relationship between I_d and $I_{t,m}$, a likely $I_{t,m}$ was determined for each experimental event; this value combined with the upper limit for $\epsilon_{N,x}/I_t$ yields an upper limit of $\epsilon_{N,x}$ for each event [39]. The trapped electron bunches appeared with rms x sizes near the system resolution [36]. Thus, as γ increases so does the upper limit of $\epsilon_{N,x}/I_t$; this is a consequence of the system resolution instead of a property of the trapped electrons. Both the theoretical model and simulations indicate $\epsilon_{N,x}$ is not very dependent on energy (see Sec. 3.2), so the upper limit of $\epsilon_{N,x}/I_t$ for each event came from an average over a low energy interval of 2.3 to 3.0 GeV, where there is the best resolution. Figure 5.18 shows the determined upper limits of $\epsilon_{N,x}$ from the experiment compared to the simulated values of $\epsilon_{N,x}$ (presented in Ch. 3). As would be expected, the upper limits are larger than the simulated values; however, they are not gross overestimates. The minimum value achieved for the upper limit of $\epsilon_{N,x}$ is 4 μm, which is close to the theoretical prediction of $1/(4k_p)$ (2.5 μm) and smaller than the drive bunch transverse emittance.

Similarly, the theoretical model shows there is a minimum scale for $\epsilon_{N,x}$; a combination of this scale with the measured upper limit for $\epsilon_{N,x}/I_t$ results in a lower limit for I_t. Since simulations achieved emittance below $1/(4k_p)$, the minimum emittance in the simulations, 1.76 μm (see Sec. 3.2), is used for the minimum emittance scale. The experimental shot with a 4 μm upper limit for $\epsilon_{N,x}$ had a measured value of $\epsilon_{N,x}/I_t < 0.19$ μm/kA, which suggests that the I_t was greater than 9.2 kA [39].

Measurement uncertainties are dominated by systematic errors. The definition of α corresponds to a bunch with σ_z = 1.9 μm and an ionization probability at its peak field position equal to 0.5. If the trapped bunch lengths varied over the same range

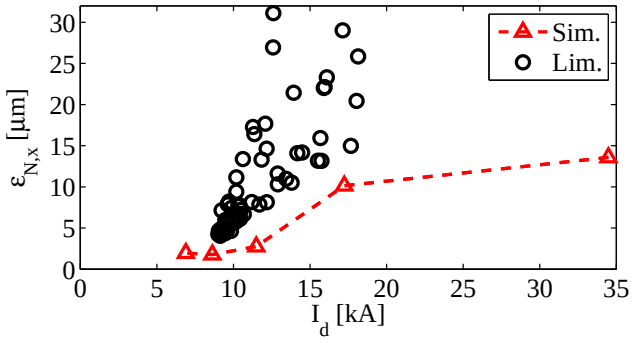

Figure 5.18: The upper limit of $\epsilon_{N,x}$ for 65 experimental events (Lim.) and the simulated values of $\epsilon_{N,x}$ (Sim.) versus the drive bunch peak current, I_d. Reprinted with permission from [39]. Copyright 2009, American Physical Society.

displayed in the simulations, it would lead to as much as a 6% error in α. In addition, the definition of α by a 0.5 ionization probability is somewhat arbitrary. Determining α by an ionization probability of 0.1 yields a 22% growth in α; however, simulations using the code QuickPIC [27] indicate that the 0.5 probability condition is more than sufficient in defining the maximum trapped electron transverse bunch size. Other systematic errors are introduced by the camera resolution and the neglect of the $x\dot{x}$ correlation term; both of these terms result in an overestimate of $\epsilon_{N,x}/I_t$. The net result of the errors is a measurement that is systematically larger than the actual $\epsilon_{N,x}/I_t$. Furthermore, the determination of $\epsilon_{N,x}$ and I_t from $\epsilon_{N,x}/I_t$ is done assuming the maximum possible peak current and the minimum possible emittance, so these determined values will be systematically larger and smaller, respectively, than the actual values.

5.5 Conclusion

This chapter presents measurements addressing both the properties of the trapped electron bunches and methods to terminate them. As discussed in Sec. 2.7, one of the methods to terminate plasma electron trapping for a PWFA-based high energy collider is to use an electron drive bunch with a peak current below $I_A/2$. The measurements here confirm this prediction.

A combination of the data from the energy spectrometers yields a measurement of

the trapped electron momentum distribution over more than 3 orders of magnitude in momentum. In addition, the transverse width of the trapped electron bunches at the large dipole energy spectrometer is related to their transverse emittance over their peak current. This result and simulations indicate that the observed values of $\epsilon_{N,x}/I_t$ result from multi-GeV trapped electron bunches with emittances of a few μm and multi-kA peak currents.

Chapter 6

Future Experiments

6.1 Introduction

As shown in the prior chapters, trapped electrons can play a critical role in the drive bunch-plasma interaction and are also a possible avenue to explore as a particle source. The experiments described in this thesis yield a basic understanding of the properties for these trapped electrons. So far, the trapped electron research has been a side study to the plasma wakefield acceleration experiment. However, moving forward with the trapped electron research requires for the trapped electrons to advance beyond a side project.

The main problem with the use of the trapped electrons as a particle source is their longitudinal emittance. Section 3.7 discusses one idea for improving the longitudinal emittance. This material is not produced again here, but this would be an excellent candidate for a future trapped electron experiment.

Other suggestions for future trapped electron experiments can be placed into two categories: assessing the effect that trapped electrons have on a plasma-based collider and measuring their properties. The first suggestion could still be run alongside the plasma wakefield acceleration experiments. However, the second suggestion requires a completely different plasma source. The remainder of this chapter provides an overview for a few suggestions of experiments in the two categories.

6.2 Effect of Trapped Electrons

Section 2.7 discusses some of the methods available to terminate electron trapping. These methods include using low peak current electron bunches ($< I_A/2$), complete pre-ionization of the vapor, and self ionizing a hydrogen vapor. Measurements in this dissertation have shown that below a drive bunch current of $I_A/2$ plasma electron trapping turns off. The next set of experiments could test whether a self-ionized hydrogen PWFA could cease trapping while retaining a strong accelerating wake. Another remaining issue is to measure how much of a detrimental effect the trapped electrons have on the wake. The remainder of this section is devoted to this issue.

Ideally, the effect of the trapped electrons should be quantified by comparing the energy transferred from a drive bunch to a witness bunch with and without trapping. However, there is still some research that can occur with a single electron bunch. Similar to recent experiments, this single bunch must be long enough to sample the accelerating part of the wake. Then, by measuring the maximum energy achieved by electrons in the back of the drive bunch, the effect that the trapped electrons have on loading the wake can be quantified.

The biggest obstacle to performing such an experiment is turning trapping on and off. One method to turn off trapping is to reduce the peak current of the drive bunch. This is, however, not ideal for measuring the loading effect of the trapped electrons. As the drive bunch peak current decreases it naturally creates a weaker accelerating field, which would make it difficult to differentiate the effect of the trapped electrons from that of the variation in the drive bunch peak current.

Pre-ionization of the vapor is a more direct method of monitoring the effect of the trapped electrons. The trapping in recent experiments occurred from the presence of both helium and lithium, so the termination of trapping only requires a pre-ionization of the helium-lithium boundary region. Also, only the trapping from the upstream boundary affects the acceleration of the electrons through the lithium core of the heat-pipe oven. As the drive bunch traverses the upstream boundary it transitions from low to high lithium density, which causes the length of the plasma bubble to shorten. Since trapped electrons reside at the back of the bubble, only the electrons that are trapped at a plasma density near that of the maximum, $2.7{\cdot}10^{23}$ m^{-3}, remain

in the accelerating part of the bubble. Figure 6.1 shows an illustration of the bubble shortening from a two-dimensional OSIRIS simulation. Thus, only a small region of the upstream boundary would require pre-ionization to terminate the effect of the trapped electrons.

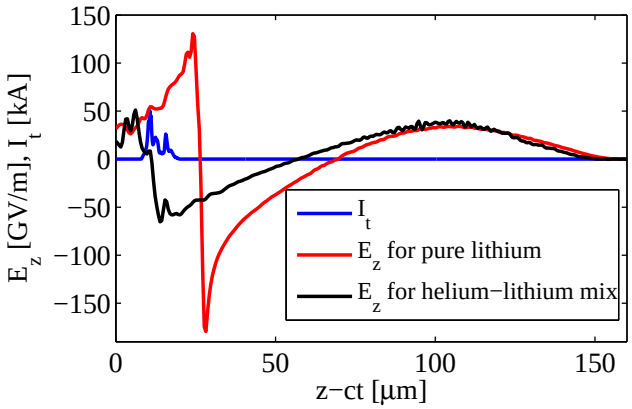

Figure 6.1: The loaded accelerating field (black line) and trapped electron current profile (blue line) from a drive bunch creating a wake in a lithium vapor of density $1.5{\cdot}10^{23}$ m^{-3} with a background helium vapor density of $1.2{\cdot}10^{23}$ m^{-3} compared to an unloaded accelerating field (red line) from a drive bunch creating a wake in a lithium vapor of density $2.7{\cdot}10^{23}$ m^{-3}. These simulations are for a Gaussian drive bunch with $1.8 \cdot 10^{10}$ electrons, matched transverse sizes of $\sigma_{x,y} = 1.74$ μm, and $\sigma_z = 20$ μm. In r and z, the simulation grid size is 0.5 μm with 9 particles per cell.

Since this type of pre-ionization only stops trapping in the upstream boundary, the charge measuring toroid will still measure additional charge from electron trapping in the downstream transition region. Thus, the experimental signature for the termination of electron trapping at the upstream boundary does not come from the charge measuring toroid, but would be the absence of the high energy trapped electrons (shown in Fig. 5.9). The presence of these high energy streaks could then be correlated to the energy spectrum of the drive bunch to determine the loading effect of the trapped electrons.

6.3 Trapped Electron Bunch Properties

Chapter 5 showed that the trapped electrons created a plasma wake in the downstream helium buffer gas, which kept them confined transversely. The effect of this confinement made the determination of the trapped electron transverse emittance difficult: a combination of measurements and simulations was only able to yield an upper limit for the trapped electron emittance. In addition, the buffer gas affected the trapped electron energy distribution. A mono-energetic trapped electron bunch produced in the lithium part of the oven would not appear mono-energetic on downstream diagnostics; the bunch would acquire a large energy spread as it drove a decelerating wake in the buffer gas. Thus, it is important to remove the effect of the buffer gas to measure the properties of the trapped electron bunches. Helium already has the highest ground state ionization energy, so the buffer gas can not simply be switched to another element. Dispensing the buffer gas altogether is the only way to remove the effect of this region, which requires a complete redesign of the plasma source.

6.3.1 Need for a New Plasma Source

Since there can no longer be a buffer region, a heat-pipe oven can not be used as the plasma source. However, the new source must still create a boundary between the beam-line vacuum of the accelerator and the vapor. Physical boundaries, such as beryllium windows, would be ruined by contact with the plasma. A couple of other possibilities are the use of a gas jet or differential pumping. Both of these possibilities require active vacuum pumping, so they would need to use elements that remain in the gas phase throughout the pumping process. Otherwise, the elements would coat the pumping system. Unfortunately, elements like lithium with low ionization potentials could then no longer be used.

Of the elements that are in the gas phase at room temperature and at atmospheric pressure, the lowest first ionization potentials occur for radon (10.7 eV), xenon (12.1 eV), chlorine (13.0 eV), and hydrogen (13.6 eV). Radon is radioactive, and chlorine is toxic. Although xenon has a slightly smaller ionization potential than hydrogen, its second ionization level (21.2 eV) is lower than the first ionization for helium, so

multiple ionization would occur. The relative density of the trapping species to the species that supports the wake would be a desirable experimental variable. However, this would not be possible for xenon; its first ionization would release the electrons that support the wake, while its second ionization would release electrons that become trapped. Thus, the trapping species density would be equal to that of the wake supporting species. For this reason, the use of a mixed hydrogen and helium vapor is suggested.

While the ionization potential of hydrogen is much lower than the 24.6 eV required for helium ionization, it is large enough to produce field ionization problems for the drive bunch at large radii (discussed also in Sec. 2.7). The reduced radial range of ionization from the drive bunch lessens the strength of the resulting plasma wake and decreases the probability of electron trapping. Consider, for example, a standard drive bunch from recent experiments. This bunch has $1.8 \cdot 10^{10}$ electrons with $\sigma_z = 20$ μm ($I_d \approx I_A$). Figure 6.2 shows the radial extend of ionization from this bunch in a lithium and hydrogen vapor. The ionization probability for hydrogen starts to roll off around $r = 30$ μm. At a plasma density of $2.7{\cdot}10^{23}$ m^{-3}, a drive bunch with $I_d = I_A$ has a maximum ion bubble radius, R_m, of ≈ 29 μm (see Eq. 2.18). Ideally, the radial range of ionization should be much greater than R_m. Otherwise, the accelerating phase of the wake is destroyed (see Sec. 2.7.2).

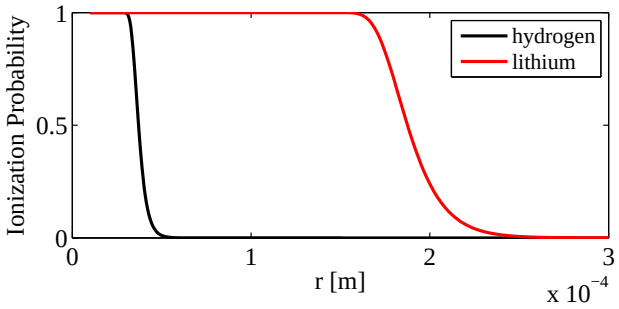

Figure 6.2: The ionization probability of hydrogen and lithium versus radius from a drive bunch with $1.8 \cdot 10^{10}$ electrons and $\sigma_z = 20$ μm.

A set of two-dimensional OSIRIS simulations explored the effect of this limited radial range of ionization on the plasma wake. These simulations were of a Gaussian drive bunch with $1.8 \cdot 10^{10}$ electrons, matched transverse sizes of $\sigma_{x,y} = 1.74$ μm, and $\sigma_z = 20$ μm creating a wake in pre-ionized plasma, a hydrogen vapor, and a lithium

vapor, all with a density of $2.7 \cdot 10^{23}$ m^{-3}. In r and z the simulation grid size is 0.5 μm with 9 particles per cell. Figure 6.3a shows the resulting on-axis E_z for the three different plasma sources. The pre-ionized and lithium plasma wakes are similar; however, the hydrogen wake differs from the others substantially, particularly in the accelerating part of the wake. Figure 6.3b displays the resulting on-axis Ψ for the three different plasma sources. The extent of the radial ionization also substantially affects Ψ in the accelerating part of the wake, making Ψ_f considerably higher. This increase in Ψ_f decreases the probability of electron trapping.

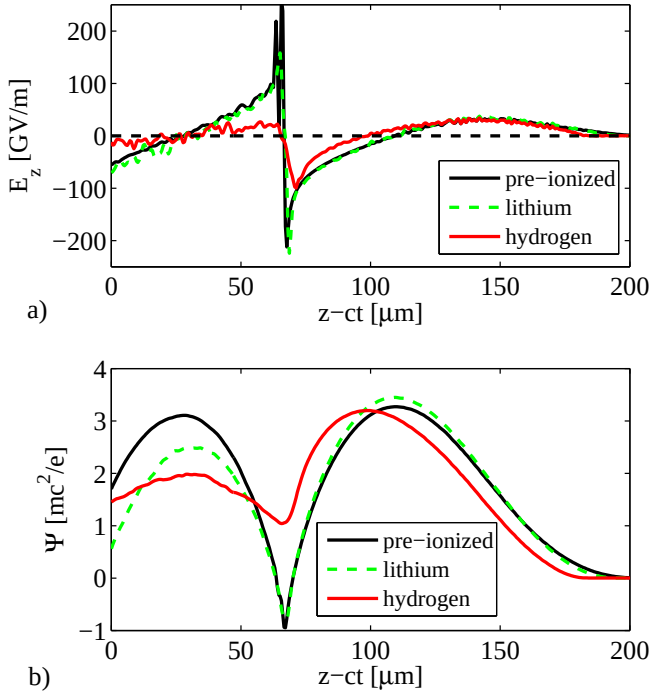

Figure 6.3: a) The on-axis E_z and b) Ψ from a Gaussian drive bunch with $1.8 \cdot 10^{10}$ electrons, matched transverse sizes of $\sigma_{x,y} = 1.74$ μm, and $\sigma_z = 20$ μm creating a wake in pre-ionized plasma, hydrogen vapor, and lithium vapor, all with a density of $2.7 \cdot 10^{23}$ m^{-3} m.

A Gaussian drive bunch with $1.8 \cdot 10^{10}$ electrons and $\sigma_z = 20$ μm in a hydrogen-helium mixed plasma of density $2.7 \cdot 10^{23}$ m^{-3} is not an effective way of producing trapped electrons. There are, however, a few possible modifications to these parameters that make trapping possible. The first possibility is to increase the peak current

of the bunch, which increases the radial range of ionization. Another possibility is to pre-ionize, or at least partially pre-ionize, the hydrogen gas. This also increases the radial range of the drive bunch-plasma interaction. Finally, the density of the plasma could be increased. The radius of ionization would remain roughly the same; however, at higher plasma density R_m decreases. The following sections give an overview of the requirements for inducing trapping, along with supporting simulations, for these approaches.

6.3.2 Short Drive Bunches

In recent experiments, a typical drive bunch had $\sigma_z = 20$ μm and a peak current equal to the Alfvén current; however, shorter bunches were created. A set of two-dimensional OSIRIS simulations tested the peak current that is required to initiate trapping in a helium-hydrogen mixed plasma. As in the experiment, the drive bunches had $1.8 \cdot 10^{10}$ electrons, $\sigma_x = \sigma_y = 1.74$ μm, and had a variable σ_z, which changed the bunch peak current. The plasma was made from a hydrogen vapor of density $2.7 \cdot 10^{23}$ m^{-3} with a 10% relative helium vapor density. In r and z the simulation grid size was 0.5 μm with 9 particles per cell. These simulations ran until the trapped electrons loaded the wake and turned off additional trapping. Figure 6.4 shows how the amount of trapped charge increased with decreasing bunch length. Electron trapping begins to increase at σ_z below 17 μm. This is near the design limit of the Facilities for Accelerator Science and Experimental Test Beams (FACET), so the production of trapped electrons by compressing the drive bunch length alone is marginal at FACET.

6.3.3 Partial Pre-Ionization

Partial pre-ionization of the hydrogen vapor extends the radial range of the bunch-plasma interaction, which increases the probability of electron trapping. A set of two-dimensional OSIRIS simulations tested the level of pre-ionization that is required to initiate trapping in a helium-hydrogen mixed plasma. The drive bunch had $1.8 \cdot 10^{10}$ electrons, $\sigma_x = \sigma_y = 1.74$ μm, and $\sigma_z = 20$ μm. This bunch created a wake in a hydrogen vapor of density $2.7 \cdot 10^{23}$ m^{-3} with a 10% relative helium vapor density.

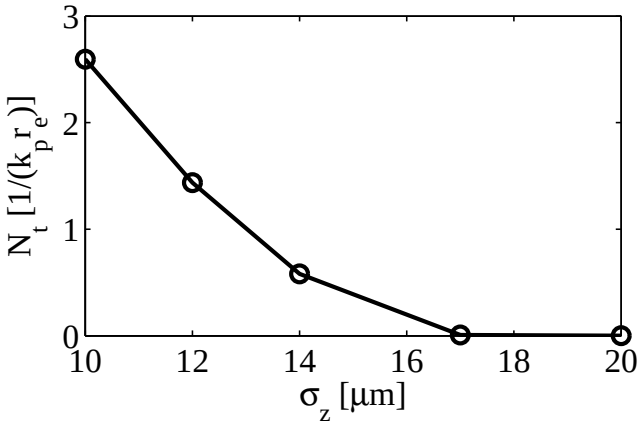

Figure 6.4: The number of trapped electrons, N_t, versus σ_z of the drive bunch, where the drive bunch had fixed total charge of $1.8 \cdot 10^{10}$ electrons.

The level of pre-ionization for the hydrogen was varied from zero to one (100%). In r and z the simulation grid size was 0.5 μm with 9 particles per cell. These simulations ran until the trapped electrons loaded the wake and turned off additional trapping. Figure 6.5 shows how the amount of trapped charge increases with the level of pre-ionization. The number of trapped electrons increases until reaching a pre-ionization level of 0.4 and then decreases before rising again to reach a maximum for full pre-ionization. Note, the pre-ionized and bunch-ionized plasma electrons are expelled from the bunch axis at slightly different times. This causes the wakes produced by these different electrons to be shifted relative to each other. When there is more of one type of ionization than the other, that type dominates the wake. However, when the relative amount of pre-ionized and bunch-ionized plasma electrons are equal, the interference of the wakes causes a dip in the amount of trapped electrons.

6.3.4 High Vapor Density

The recent experiments had a plasma density of $2.7 \cdot 10^{23}$ m^{-3}; however, this could be changed for future experiments. An increase in the plasma density decreases $1/k_p$ and the radial ionization range required to induce electron trapping. Note, the minimum bunch length will not be too much smaller than 20 μm, so the plasma density can not be raised arbitrarily. A set of two-dimensional OSIRIS simulations tested the

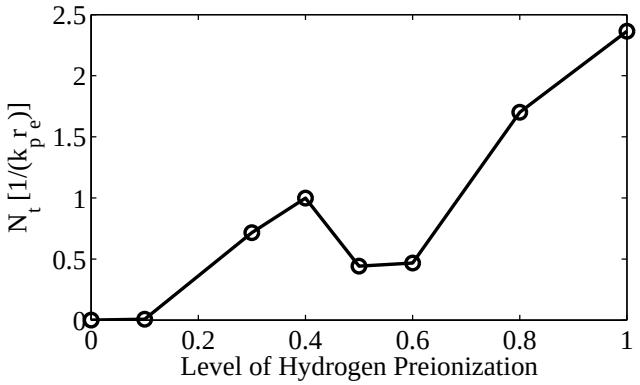

Figure 6.5: The number of trapped electrons, N_t, versus the level of hydrogen pre-ionization in a hydrogen-helium plasma.

plasma density increase required to initiate trapping in a helium-hydrogen mixed plasma. The drive bunches had $1.8 \cdot 10^{10}$ electrons, $\sigma_x = \sigma_y = 1.74$ μm, and $\sigma_z = 20$ μm. These drive bunches created a wake in four different hydrogen vapor densities: $2.7 \cdot 10^{23}$ m^{-3}, $5.4 \cdot 10^{23}$ m^{-3}, $8.1 \cdot 10^{23}$ m^{-3}, and $1.08 \cdot 10^{24}$ m^{-3}, all with a 10% relative helium density. In r and z the simulation grid size was $0.05/k_p$ with 9 particles per cell. These simulations ran until the trapped electrons loaded the wake and turned off additional trapping. Figure 6.6 shows how the amount of trapped charge increases with the increasing plasma density. An increase of the plasma density by a factor of two (to $5.4 \cdot 10^{23}$ m^{-3}) turns trapping on in a hydrogen-helium mixed plasma.

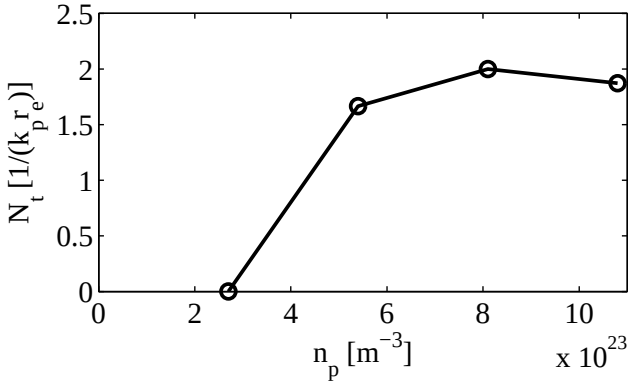

Figure 6.6: The number of trapped electrons, N_t, versus the plasma density in a hydrogen-helium plasma.

In conclusion, partial pre-ionization causes the onset of electron trapping, but

would involve the added overhead of a pre-ionization system. Conversely, a small increase in the plasma density causes the trapping of plasma electrons, without any additional overhead. The production of trapped electrons through a compression of the longitudinal drive bunch length is marginal to work. However, this compression could be paired with the increase in plasma density to yield an added experimental range at lower plasma density.

6.3.5 Trapped Electron Bunch Characterization

The absence of the buffer gas region allows for a more direct measurement of the trapped electron bunch properties. For example, the trapped electron energy profile measured on downstream diagnostics would no longer include the effect of the buffer region. In addition, the absence of the buffer region allows for the determination of the trapped electron bunch emittance from its transverse size. By measuring the roll-off in the plasma density at the edges of either the gas jet or the differentially pumped region, the transverse transportation properties are determined. Then, the methods displayed in Sec. 5.4.3 would connect the transverse size to emittance.

Chapter 7

Conclusion

Electron trapping in a PWFA is an important subject from two different perspectives. From the viewpoint of designing a plasma-based high energy collider, there is a need to understand how to minimize the detrimental effects of electron trapping. In addition, the trapped electrons might work as a low emittance and high current particle source. Both of these topics are covered in this dissertation with a combination of theory, simulations, and experimental measurements.

Chapter 2 presents a study of the drive bunch and plasma properties required to cause the onset of ionization induced electron trapping. This includes a derivation of the critical drive bunch peak current, $I_A/2$, and number of drive bunch electrons, $1/(k_p r_e)$, needed to cause trapping. Section 2.7 uses these results as the foundation for a discussion of ways to terminate electron trapping. A summary of this section follows. Complete pre-ionization of the plasma trivially rids the wake of trapped electrons, but this is a nontrivial engineering feat. Also, the use of a self-ionized hydrogen plasma at high plasma density ($\geq 4 \cdot 10^{23}$ m^{-3}) or high drive bunch peak current ($\geq 4I_A$) would terminate the trapping of electrons. However, a hydrogen plasma would suffer from ion motion issues. Another method to cease trapping is the use of drive bunches with low charge ($< 1/(k_p r_e)$) or low peak current ($< I_A/2$). In addition to the theoretical arguments and simulations supporting this, measurements in Ch. 5 verified that electron trapping terminates below a drive bunch peak current of $I_A/2$.

Chapter 3 uses theory and simulations to explore all aspects of the trapped electron bunch properties. This includes the development of a theoretical model for the trapped electron transverse emittance, which reveals a fundamental scale for the minimum achievable emittance, $1/(4k_p)$. Chapter 5 contains an upper limit measurement of the trapped electron transverse emittance over peak current, $\epsilon_{N,x}/I_t$. The theoretical model and simulations indicate that the observed values of $\epsilon_{N,x}/I_t$ result from multi-GeV trapped electron bunches with emittances of a few μm, which is consistent with the model, and multi-kA peak currents.

One of the fundamental problems for the use of trapped electrons as a particle source is their large energy spread. Chapter 3 discusses the fundamental reasons for these large energy spreads, and Ch. 5 shows supporting measurements of the trapped electron momentum distribution over more than three orders of magnitude. In response to this, Sec. 3.7 includes a discussion of one method to reduce the trapped electron energy spread, along with supporting simulations. These simulations indicate that this method could produce electron bunches with a longitudinal emittance that is better than conventional electron sources.

Another topic of great importance to this thesis is suggestions for future experiments. The theoretical arguments and measurements presented in this dissertation give a glimpse of the trapped electron properties, but more work is needed. For example, the effect that the trapped electrons have on the accelerating wake has not yet been measured; Ch. 6 suggests experimental methods to quantify this. Also, measurements of the trapped electron properties were hindered by the buffer gas in the heat-pipe oven. Chapter 6 details several different methods to create trapping in a helium-hydrogen mixed vapor, without the use of a buffer gas. In addition, Ch. 6 suggests a method to directly measure the trapped electron transverse emittance in such a system.

Appendix A

Gas Jet-Produced Hollow Plasma

A.1 Introduction

The effect of ion motion and the need for practical positron propagation in a plasma wakefield accelerator have incited interest in hollow plasma channels. These channels are typically assumed to be cylindrically symmetric; however, a different geometry might be easier to achieve. The introduction of an obstruction into the outlet of a high Mach number gas jet can produce two parallel slabs of gas separated by a density depression. Here, there is a detailed simulation study of the density depression created in such a system [38]. This investigation reveals that the density depression is insufficient at the desired plasma density. However, insights from the simulations suggest another avenue for the creation of the hollow slab geometry.

Plasma-based particle accelerators have shown immense potential for future high energy colliders [9,45]; however, there are several remaining issues. Two of the biggest obstacles for the PWFA are ion motion [65] and the need for positron propagation [7]. A hollow channel plasma does not have ions on the axis of bunch propagation. The absence of on-axis ions removes the possibility for ion motion and eliminates the intrinsic defocusing they create for positrons. Thus, the creation of a hollow channel plasma would be a tremendous asset for the PWFA.

While a hollow channel plasma offers solutions to PWFA problems, there is not yet a proven method for generating one. A current idea for the production of a hollow channel is to use a cylindrically-symmetric acoustic standing wave to create a density

depression on the axis of bunch propagation; this is similar to methods used for the purpose of laser guiding [21]. Another idea utilizes a high-order Bessel laser beam with an intensity profile that peaks off axis. When applied to a gas of uniform density, this laser could ionize a hollow channel of plasma centered about the axis [31]. These ideas focus on the production of cylindrically-symmetric hollow channels. Consider instead a different geometry, one with an evacuation of gas atoms from a small region in the Cartesian y coordinate. This geometry consists of two parallel slabs of gas, between which a drive bunch could create a plasma wake.

This appendix investigates one idea for a method to produce such a hollow channel plasma. The basic concept is to insert an obstruction into a high Mach number gas jet. In the absence of interatomic collisions, the atoms that contact the obstruction scatter, producing a perfect hollow channel behind the obstruction (illustrated in Fig. A.1). A computational technique is developed here to study the effect of the atom-atom collisions on the density depression.

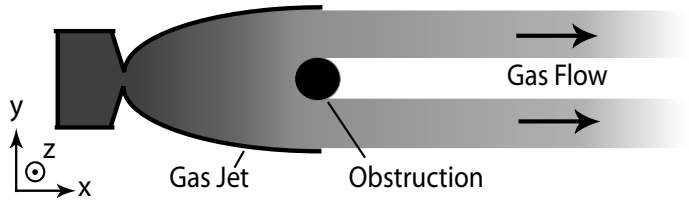

Figure A.1: A gas jet-produced hollow vapor channel. The drive bunch would travel in the z direction, between the two slabs of flowing gas. Reprinted with permission from [38]. Copyright 2009, Institute of Electrical & Electronics Engineers.

A.2 Hollow Slab Accelerator Physics

A plasma wake that is created between two parallel slabs of gas has different accelerating and focusing properties than a typical PWFA. Thus, it is worth discussing the accelerator physics issues associated with this type of a configuration. A cylindrically-symmetric hollow channel has no focusing force and an accelerating field that is independent of r inside the bubble. The same is not true for a Cartesian hollow channel. While the channel is symmetric with translations in x, the drive bunch is not. The

expulsion of the plasma electrons creates two opposing electric dipoles, as shown in Fig. A.2, resulting in quadrupole focusing fields.

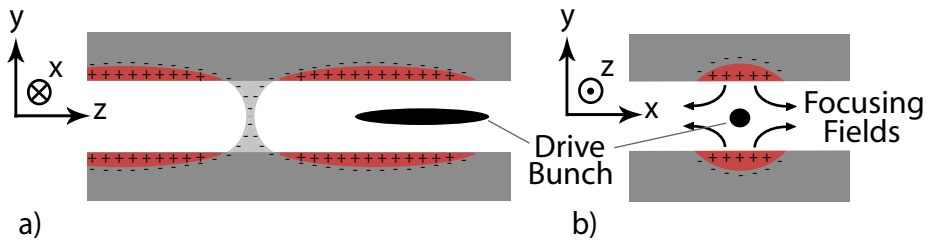

Figure A.2: A plasma wake in a gas jet-produced hollow channel, where + and - denote charge density. a) A $y-z$ slice of the wake at $x=0$, where the drive bunch travels to the right. b) An $x-y$ slice of the wake, where the drive bunch travels out of the paper.

As Fig. A.2b shows, the quadrupole focusing force is focusing in one direction and defocusing in the other. This is also apparent from Maxwell's equations. The following shows the x focusing force, F_x, for an ultrarelativistic particle of charge q traveling in the z direction

$$F_x = q(E_x - cB_y). \tag{A.1}$$

A partial derivative of this with respect to x yields

$$\frac{\partial F_x}{\partial x} = q(\frac{\partial E_x}{\partial x} - c\frac{\partial B_y}{\partial x}). \tag{A.2}$$

Gauss' law gives

$$\frac{\partial E_x}{\partial x} = -\frac{\partial E_y}{\partial y} - \frac{\partial E_z}{\partial z} + \frac{\rho}{\epsilon_0}, \tag{A.3}$$

and the z component of Ampere's law yields (assuming $\partial_t = -c\partial_z$)

$$-c\frac{\partial B_y}{\partial x} = \frac{\partial E_z}{\partial z} - c\frac{\partial B_x}{\partial y} - \mu_0 c J_z. \tag{A.4}$$

The substitution of Eqs. A.3 and A.4 into Eq. A.2 results in

$$\frac{\partial F_x}{\partial x} = -q(\frac{\partial E_y}{\partial y} + c\frac{\partial B_x}{\partial y} + \frac{1}{\epsilon_0}(\frac{J_z}{c} - \rho)). \tag{A.5}$$

In the middle of the hollow channel the only charge and current come from the drive

bunch, so the source terms cancel. This yields

$$\frac{\partial F_x}{\partial x} = -q(\frac{\partial E_y}{\partial y} + c\frac{\partial B_x}{\partial y}) = -\frac{\partial F_y}{\partial y}. \tag{A.6}$$

Let the center of the bunch be situated at $x = 0$ and $y = 0$. As Fig. A.2b shows, the system is symmetric with reflections about the x and y axes at $y = 0$ and $x = 0$, respectively. This means that a reflection about the x axis must change the sign of F_y, but not the sign of F_x. Similarly, a reflection about the y axis must change the sign of F_x, but not the sign of F_y. In other words, the terms of F_x are odd in x and even in y, and the terms of F_y are odd in y and even in x:

$$F_x(x, y, z - ct) = K_x x + O(x^3, xy^2), \tag{A.7}$$

$$F_y(x, y, z - ct) = K_y y + O(y^3, yx^2). \tag{A.8}$$

From Eq. A.6, $K_x = -K_y$. Thus, if the system is focusing in x then it is defocusing in y, and vice versa. The fact that the system is intrinsically defocusing in one direction is a problem. In addition, the strength of the focusing fields is related to the displacement of the electrons in the plasma sheath. This displacement changes along the bunch, as illustrated in Fig. A.2a, which changes the focusing strength along the bunch. Thus, K_x and K_y are both functions of $z - ct$.

The longitudinal accelerating field is no longer a constant inside the plasma sheath. This can be seen from Faraday's law. Consider the x and y components of this law:

$$\frac{\partial E_z}{\partial y} - \frac{\partial E_y}{\partial z} = c\frac{\partial B_x}{\partial z}, \tag{A.9}$$

$$\frac{\partial E_x}{\partial z} - \frac{\partial E_z}{\partial x} = c\frac{\partial B_y}{\partial z}. \tag{A.10}$$

A reorganization of these equations, combined with x and y derivatives, results in

$$\frac{\partial^2 E_z}{\partial y^2} = \frac{\partial}{\partial z}[\frac{\partial}{\partial y}(E_y + cB_x)], \tag{A.11}$$

$$\frac{\partial^2 E_z}{\partial x^2} = \frac{\partial}{\partial z}[\frac{\partial}{\partial x}(E_x - cB_y)]. \tag{A.12}$$

A substitution of the results from Eq. A.6 into these equations yields

$$\frac{\partial^2 E_z}{\partial x^2} = -\frac{\partial^2 E_z}{\partial y^2}. \tag{A.13}$$

An investigation of the system's symmetry yields the non-zero terms in the expansion of E_z. Since the force from E_z is perpendicular to x and y, then it must be even in both x and y. An expansion of E_z then appears as

$$E_z(x, y, z - ct) = E_z(0, 0, z - ct) + Gx^2 - Gy^2 + O(x^4, y^4, x^2y^2), \tag{A.14}$$

where G is also a function of $z - ct$. The opposite signs of the x^2 and y^2 terms are mandated by Eq. A.13.

The intrinsic defocusing in one direction and the transverse variation of E_z are both not ideal. However, a crossing of the hollow plasma channels can correct these problems. Ideally, this crossing would occur at the same z position, but this is not possible. For a gas jet to work properly, the width of the jet in y must be much larger than a mean free path length. Thus, crossing the jets would produce a scatter of atoms that would fill in the density depression of the hollow channel. Instead, the jets can be crossed in a staggered configuration (see Fig. A.3).

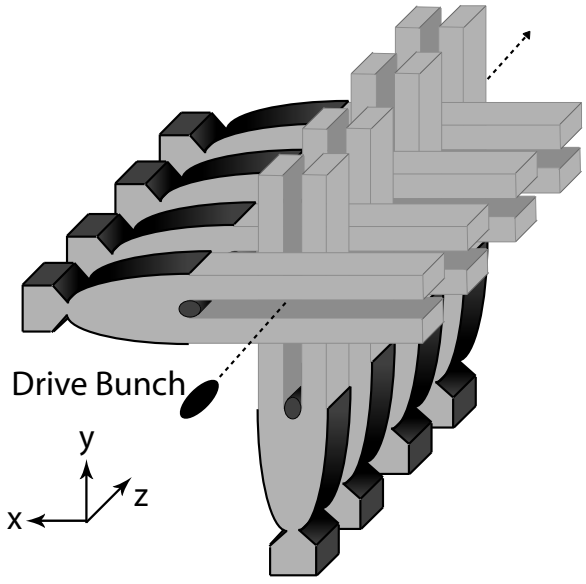

Figure A.3: The staggered crossing of hollow channel cells.

A staggered configuration corrects both the focusing and accelerating problems of a single gas jet. By rotating successive jets by $\pi/2$ from the prior one, the focusing force in any direction flips back and forth from focusing to defocusing. The strong focusing principle then allows for net focusing of the bunch. Additionally, as long as the drive bunch particles do not change their transverse position much before the jet direction is rotated, the second order terms in Eq. A.14 cancel. This is apparent from the fact that under rotation the quantity G in Eq. A.14 goes to $-G$.

A.3 Requirements of a Hollow Channel

Before progressing into the computational techniques used to test the feasibility of the production of such a hollow plasma, it is important to quantify how deep the density depression must be for the PWFA application. This allows for the interpretation of results. Consider this question from the perspective of ion motion. Rosenzweig et al [65] examined the motion of ions induced by the intense transverse electric field of a matched drive bunch. They found that these intense fields could cause ions to move significantly before the bunch passes, which creates nonlinear focusing forces and transverse emittance growth. A summary of this issue is given in Sec. 1.5.3. This section connects ion motion to a dimensionless constant, A_{ion}, which depends on the drive bunch and plasma parameters. A catastrophic amount of ion motion occurs for $A_{ion} = 0.473$, where the ions collapse from their initial radii to a radius of zero. For ion motion smaller than this value, the ions have transverse positions that are proportional to their initial positions. Thus, the ion density would still be uniform at the core of the bunch, but at an increased magnitude. As is shown in Fig. 1.9, a less severe amount of ion motion occurs for $A_{ion} = 10^{-1}$. For simplicity, let $A_{ion} = 10^{-1}$ set the scale for an endurable amount of ion motion.

Current concepts for a plasma-based linear collider utilize a bunch with 10^{10} electrons, energy of 500 GeV ($\gamma = 978{,}475$), longitudinal bunch length equal to 10 μm, and normalized transverse emittances, $\epsilon_{N,x}$ and $\epsilon_{N,y}$, equal to 2 and 0.05 μm, respectively [63]. In this case, a substitution of $\epsilon_N = \sqrt{\epsilon_{N,x}\epsilon_{N,y}}/2$ into Eq. 1.59 is appropriate for A_{ion}. As is discussed later, simulations here are performed for helium. Consider the effect the drive bunch has on a fully-ionized helium atom ($Q = 2$).

For these parameters, the plasma density must be reduced to $1.5 \cdot 10^{19}$ m^{-3} before $A_{ion} = 10^{-1}$ (from Eq. 1.59). This is almost four orders of magnitude below the density used in current concepts for a PWFA-based collider, 10^{23} m^{-3}. Thus, extremely deep density depressions are required for this application of the PWFA.

A.4 Computational Techniques

A particle tracking method is used to simulate the flow of atoms around the obstruction. The number of particles in the physical system is too large for the simulation of individual atoms, so a macro-particle represents the movement of a collection of atoms. To properly represent the interatomic collisions, the mean free path of the macro-particles must be equal to that in the physical system, $\lambda = (4\pi r_v^2 n)^{-1}$, where n is the gas density and r_v is the van der Waals radius. Since the macro-particle density, n_s, is less than n, the macro-particle hard sphere radius, r_s, must increase to maintain λ: $r_s = r_v\sqrt{n/n_s}$.

Proper boundary conditions are also required to accurately simulate the flow of atoms. A discussion of the simulation boundaries, as illustrated in Fig. A.4, follows. Let dt denote the simulation time step. At each time step, macro-particles with a velocity of $v\hat{x}$ are initialized at side 1 with a density of n_s and in a space of size $v \cdot dt$, D_y, and D_z in x, y, and z, respectively. Then, the coordinates for all of the macro-particles are propagated, based on the particle velocities, to the next time step. Upon contacting sides 5 or 6, a particle is re-emitted from the opposing side with its same momentum and x and y position. Contact to sides 1, 2, 3, or 4 results in deletion of the particle. The obstruction surface is coarse compared to r_v, so the scatter from it must be diffuse. A macro-particle is elastically scattered from the obstruction with a randomly distributed direction into the half-space facing away from the obstruction.

Next, the simulation code compares macro-particle positions. The particles with a separation smaller than $2r_s$ are propagated back to the time they first collided and scattered elastically as hard spheres. Let N_s denote the number of simulation particles. The computational time required for the interatomic collisions is proportional to N_s^2. To minimize calculation time, the simulation box is divided into grids in the

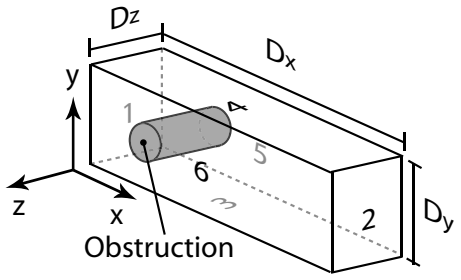

Figure A.4: The gas jet simulation boundaries. Reprinted with permission from [38]. Copyright 2009, Institute of Electrical & Electronics Engineers.

$x - y$ plane, where macro-particle positions are only compared within the same grid. The computational time is still proportional to N_s^2, but is decreased roughly by a factor of the number of grids.

A discussion of the computational techniques is not complete without addressing the resolution issues. These issues involve r_s, dt, v, n_s, the obstruction position, and the grid size. As was just introduced, the simulation space is divided into grids in the $x - y$ plane. The size of these grids in x, y, and z must be significantly larger than r_s. This ensures that the errors introduced at the boundaries of the grids do not affect the results. Another resolution issue is that dt must be considerably smaller than r_s/v. Otherwise, macro-particles could pass through each other without interacting. An additional critical resolution issue is that $2r_s$ must be much smaller than the average interatomic separation, $n_s^{-1/3}$. If not, the particles would function as an incompressible fluid. Also, sides 1, 2, 3, and 4 must be sufficiently separated from the obstruction.

A.5 Results

A discussion of the specific simulation parameters follows. Current PWFA experiments utilize a plasma with a density near 10^{23} m^{-3}, so the gas jet simulations are performed for this density. Although the specifics of the gas jet are ignored here, monatomic gases are easier to scale to high Mach numbers, so the simulations are of a monatomic gas, helium. Helium has a van der Waals radius of $1.4 \cdot 10^{-10}$ m [11]. The van der Waals radius for other monatomic gases is of the same order as helium,

so the results here are also representative of other gas species.

Another parameter of importance is the width of the obstruction. This width governs the separation of the gas slabs and the coupling between the drive bunch and the plasma. For a non-hollow PWFA in the nonlinear bubble regime, the density of the drive bunch exceeds that of the plasma, so the bunch expels all the plasma electrons from the region around it. This produces a bubble containing a region of uniformly charged ions that are surrounded by a sheath of plasma electrons, which is characteristic of the bubble regime. The maximum radius of this bubble, R_m, is representative of the coupling between the bunch and the plasma. This maximum radius can be connected to the drive bunch peak current, I_d, as $R_m\omega_p/(2c) \approx \sqrt{2I_d/I_A}$ [47]. To produce accelerating wakes in a hollow plasma that are comparable to those in a uniform plasma, the separation between the drive bunch and the gas must not greatly exceed R_m. For $I_d = I_A$, $R_m = 2^{3/2}c/\omega_p$, which is 48 μm for a density of 10^{23} m^{-3}. For this reason, the simulations are of cylinder obstructions with a radius at and below 50 μm.

The density depression is deepest directly behind the obstruction, so the closer a drive bunch can pass by the obstruction the better. However, if the bunch comes too close it can cause breakdown of the obstruction surface. Consequently, the separation between the drive bunch and the obstruction is another critical parameter. The results of Thompson et al [69] are useful for choosing an appropriate separation. They showed that drive bunches with $1.8{\cdot}10^{10}$ electrons and a 10 kA peak current, which are similar to drive bunches in recent PWFA experiments, created breakdown when coming within 50 μm of a dielectric fiber. To account for the use of bunches with peak current at or slightly above I_A and to add an additional safety buffer, the simulations presented here are specifically dealing with a separation of 200 μm.

Figures A.5a and A.5b show the resulting density in the $x-y$ plane for cylinders of radius 50 and 10 μm, respectively, in the path of a helium gas jet of density 10^{23} m^{-3}. The density as a function of y at a 200 μm x separation from the obstructions is shown in Figs. A.6a and A.6b. These results fall far short of the density depressions required for the PWFA.

As the cylinder radius decreases in Fig. A.6b, the density depression deepens.

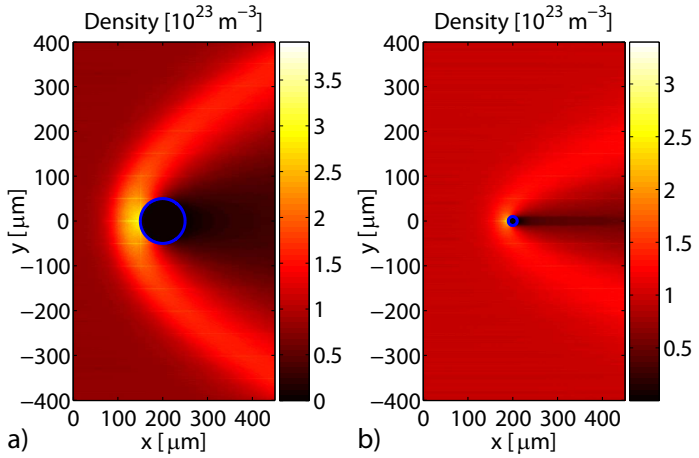

Figure A.5: The density in the $x-y$ plane for a helium gas jet of density 10^{23} m^{-3} flowing around cylinders of radius 50 (a) and 10 μm (b). Reprinted with permission from [38]. Copyright 2009, Institute of Electrical & Electronics Engineers.

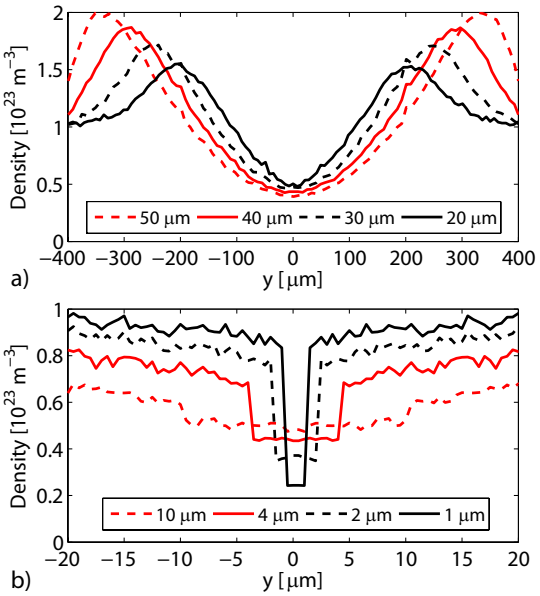

Figure A.6: Density versus y at a 200 μm x separation from cylinders of various radii in a helium gas jet of density 10^{23} m^{-3}, a) for cylinders of radius 50, 40, 30, 20, b) 10, 4, 2, and 1 μm. Reprinted with permission from [38]. Copyright 2009, Institute of Electrical & Electronics Engineers.

The mean free path for helium at a density of 10^{23} m^{-3} is 41 μm, which is significantly larger than the cylinder radii of Fig. A.6b. For these small cylinder radii, the

obstruction acts as a point source of scattered atoms. Some of these atoms are then re-scattered to behind the obstruction. Smaller cylinder radii scatter fewer atoms, so they naturally create deeper density depressions. Note, however, the simulations here do not include the thermal spread of the gas jet atoms. The inclusion of a realistic thermal spread would fill in the density depressions for these smaller radii. For this reason, the cylinder radius can not be reduced to arbitrarily low values to obtain deeper density depressions.

A.6 Conclusion

The gas jet and obstruction parameters, simulated here, fail to produce a sufficient density depression for the PWFA application. However, the basic concept of the gas jet produced hollow channel does become more effective when the mean free path greatly exceeds the cylinder radius. As discussed above, the cylinder radius can not be scaled to arbitrarily small values. Thus, methods to increase λ must be explored. A significant reduction in the gas density would lengthen λ, but this would decrease the accelerating gradient. The collisional cross section for plasma particles can be significantly below that of neutral atoms, which means the plasma particles could have a longer mean free path. Thus, the flow of plasma around an obstruction is an alternative avenue to explore for the production of a hollow channel.

Bibliography

[1] M. V. Ammosov, N. B. Delone, and V. P. Krainov. Tunnel ionization of complex atoms and of atomic ions in an alternating electromagnetic field. *Sov. Phys. JETP*, 64(6):1191, 1986.

[2] X. Artru et al. Experimental investigations on geometrical resolution of electron beam profiles given by OTR in the GeV energy range. Given at the 5th European Particle Accelerator Conference (EPAC 96), Sitges, Spain, 10-14 June 1996.

[3] K. A. Assamagan et al. Electron beam characteristics of a laser-driven plasma wakefield accelerator. *Nuclear Instruments and Methods in Physics Research Section A: Accelerators, Spectrometers, Detectors and Associated Equipment*, 438(2-3):265 – 276, 1999.

[4] K.L.F. Bane and P. Emma. LiTrack: a fast longitudinal phase space tracking code with graphical user interface. In *Proceedings of the Particle Accelerator Conference*, page 4266. IEEE, Knoxville, Tennessee, 2005.

[5] C. D. Barnes. *Longitudinal phase space measurements and application to beam-plasma physics*. PhD thesis, Stanford University, 2005.

[6] D. Bauer and P. Mulser. Exact field ionization rates in the barrier-suppression regime from numerical time-dependent Schrodinger-equation calculations. *Physical Review A*, 59(1):569, 1999.

[7] B. E. Blue et al. Plasma-wakefield acceleration of an intense positron beam. *Physical Review Letters*, 90(21):214801, May 2003.

[8] I. Blumenfeld. *Scaling of the Longitudinal Electric Field and Transformer Ratio in a Nonlinear Plasma Wakefield Accelerator*. PhD thesis, Stanford University, 2009.

[9] I. Blumenfeld et al. Energy doubling of 42 GeV electrons in a metre-scale plasma wakefield accelerator. *Nature*, 445:741–744, 2007.

[10] I. Blumenfeld et al. Measurement of the decelerating wake in a plasma wakefield accelerator. In *Advanced Accelerator Concepts*, page 569. AIP, Santa Cruz, California, 2008.

[11] A. Bondi. van der Waals volumes and radii. *Journal of Physical Chemistry*, 68(3):441, 1964.

[12] R. J. Briggs. Collective accelerator for electrons. *Physical Review Letters*, 54(24):2588, 1985.

[13] K. L. Brown and R. V. Servranckx. First- and second-order charged particle optics. Technical Report SLAC-PUB-3381, Stanford Linear Accelerator Center, 1984.

[14] D. L. Bruhwiler et al. Particle-in-cell simulations of tunneling ionization effects in plasma-based accelerators. *Physics of Plasmas*, 10(5):2022–2030, 2003.

[15] A. H. Carter. *Classical and Statistical Thermodynamics*. Prentice Hall, Inc., 2001.

[16] A. W. Chao et al. Space charge dynamics of bright electron beams. Technical Report SLAC-PUB-9189, Stanford Linear Accelerator Center, 2002.

[17] S.-Y. Chen et al. Detailed dynamics of electron beams self-trapped and accelerated in a self-modulated laser wakefield. *Physics of Plasmas*, 6(12):4739–4749, 1999.

[18] G. P. Collins. Large hadron collider: The discovery machine. *Scientific American*, pages 39–45, February 2008.

[19] J. A. Dean, editor. *Lange's Handbook of Chemistry, 15th Edition*. McGraw-Hill, 1999.

[20] T. Zh. Esirkepov. Exact charge conservation scheme for particle-in-cell simulation with an arbitrary form-factor. *Computer Physics Communications*, 135(2):144 – 153, 2001.

[21] C. M. Fauser et al. Guiding characteristics of an acoustic standing wave in a piezoelectric tube. *Applied Physics Letters*, 73(20):2902–2904, 1998.

[22] R. A. Fonseca et al. Osiris: A three-dimensional, fully relativistic particle in cell code for modeling plasma based accelerators. In *Proceedings of the International Conference on Computational Science-Part III*, page 342. Springer-Verlag, London, 2002.

[23] S. Fritzler et al. Emittance measurements of a laser-wakefield-accelerated electron beam. *Physical Review Letters*, 92(16):165006, April 2004.

[24] F. Gianotti. Physics at the LHC. *Physics Reports*, 403-404:379 – 399, 2004.

[25] C. Hernandez-Garcia et al. Electron sources for accelerators. *Physics Today*, 61(2):44, February 2008.

[26] M. J. Hogan et al. Multi-GeV energy gain in a plasma-wakefield accelerator. *Physical Review Letters*, 95(5):054802, July 2005.

[27] C. Huang et al. Quickpic: a highly efficient particle-in-cell code for modeling wakefield acceleration in plasmas. *Journal of Computational Physics*, 217(2):658, 2006.

[28] C. Huang et al. Hosing instability in the blow-out regime for plasma-wakefield acceleration. *Physical Review Letters*, 99(25):255001, 2007.

[29] R. Ischebeck et al. Energy measurements in a plasma wakefield accelerator. In *Proceedings of the Particle Accelerator Conference*, page 4168. IEEE, Albuquerque, New Mexico, 2007.

[30] D. K. Johnson et al. Positron production by X rays emitted by betatron motion in a plasma wiggler. *Physical Review Letters*, 97(17):175003, 2006.

[31] W. D. Kimura. Private Communications, 2008.

[32] W. D. Kimura et al. Laser acceleration of relativistic electrons using the inverse Cherenkov effect. *Physical Review Letters*, 74(4):546–549, January 1995.

[33] W. D. Kimura et al. First staging of two laser accelerators. *Physical Review Letters*, 86(18):4041–4043, April 2001.

[34] N. Kirby et al. Energy measurements of trapped electrons from a plasma wakefield accelerator. In *Advanced Accelerator Concepts*, page 541. AIP, Lake Geneva, Wisconsin, 2006. Copyright 2006 by the American Institute of Physics.

[35] N. Kirby et al. Emittance growth from multiple coulomb scattering in a plasma wakefield accelerator. In *Proceedings of the Particle Accelerator Conference*, page 3097. IEEE, Albuquerque, New Mexico, 2007. Copyright 2007 by the Institute of Electrical & Electronics Engineers.

[36] N. Kirby et al. Emittance measurements of trapped electrons from a plasma wakefield accelerator. In *Proceedings of the Particle Accelerator Conference*, page 4183. IEEE, Albuquerque, New Mexico, 2007. Copyright 2007 by the Institute of Electrical & Electronics Engineers.

[37] N. Kirby et al. Emittance and current of electrons trapped in a plasma wakefield accelerator. In *Advanced Accelerator Concepts*, page 591. AIP, Santa Cruz, California, 2008. Copyright 2008 by the American Institute of Physics.

[38] N. Kirby et al. Investigation of a gas jet-produced hollow plasma wakefield accelerator. In *Proceedings of the Particle Accelerator Conference*. IEEE, Vancouver, Canada, 2009. Copyright 2009 by the Institute of Electrical & Electronics Engineers.

[39] N. Kirby et al. Transverse emittance and current of multi-GeV trapped electrons in a plasma wakefield accelerator. *Physical Review Special Topics - Accelerators*

and Beams, 12(5):051302, May 2009. Copyright 2009 by the American Physical Society.

[40] R. Kodama et al. Long-scale jet formation with specularly reflected light in ultraintense laser-plasma interactions. *Physical Review Letters*, 84(4):674–677, January 2000.

[41] M. Lampe et al. Electron-hose instability of a relativistic electron beam in an ion-focusing channel. *Physics of Fluids B: Plasma Physics*, 5(6):1888–1901, 1993.

[42] S. Lee et al. Energy doubler for a linear collider. *Physical Review Special Topics - Accelerators and Beams*, 5(1):011001, January 2002.

[43] W. Leemans and E. Esarey. Laser driven plasma-wave electron accelerators. *Physics Today*, 62(3):44, March 2009. Also, references therein.

[44] W. P. Leemans et al. Gamma-neutron activation experiments using laser wakefield accelerators. volume 8, pages 2510–2516. AIP, 2001.

[45] W.P. Leemans et al. GeV electron beams from a centimetre-scale accelerator. *Nature Physics*, 2:696–699, 2006.

[46] D. R. Lide, editor. *CRC Handbook of Chemistry and Physics*. CRC Press, 84$^{\text{th}}$ edition, 2003.

[47] W. Lu et al. A nonlinear theory for multidimensional relativistic plasma wave wakefields. *Physics of Plasmas*, 13(5):056709, 2006.

[48] W. Lu et al. Nonlinear theory for relativistic plasma wakefields in the blowout regime. *Physical Review Letters*, 96(16):165002, 2006.

[49] V. Malka et al. Characterization of electron beams produced by ultrashort (30 fs) laser pulses. *Physics of Plasmas*, 8(6):2605–2608, 2001.

[50] K. A. Marsh et al. Beam matching to a plasma wake field accelerator using a ramped density profile at the plasma boundary. In *Proceedings of the Particle Accelerator Conference*, page 2702. IEEE, Knoxville, Tennessee, 2005.

[51] A. Modena et al. Electron acceleration from the breaking of relativistic plasma waves. *Nature (London)*, 377:606–608, 1995.

[52] B. W. Montague and W. Schnell. Multiple scattering and synchrotron radiation in the plasma beat-wave accelerator. *AIP Conference Proceedings*, 130(1):146–155, 1985.

[53] P. Muggli et al. Photo-ionized lithium source for plasma accelerator applications. *IEEE Transactions on Plasma Science*, 27(3):791, 1999.

[54] P. Muggli et al. Halo formation and emittance growth of positron beams in plasmas. *Physical Review Letters*, 101(5):055001, 2008.

[55] P. Musumeci et al. High energy gain of trapped electrons in a tapered, diffraction-dominated inverse-free-electron laser. *Physical Review Letters*, 94(15):154801, April 2005.

[56] C. L. O'Connell et al. Dynamic focusing of an electron beam through a long plasma. *Physical Review Special Topics - Accelerators and Beams*, 5(12):121301, December 2002.

[57] C. L. O'Connell et al. Plasma production via field ionization. *Physical Review Special Topics - Accelerators and Beams*, 9(10):101301, October 2006.

[58] E. Oz et al. Ionization-induced electron trapping in ultrarelativistic plasma wakes. *Physical Review Letters*, 98(8):084801, 2007.

[59] W. K. H. Panofsky. Evolution of particle accelerators and colliders. *SLAC Beam Line*, 27N1:36–44, 1999.

[60] T. Plettner et al. Visible-laser acceleration of relativistic electrons in a semi-infinite vacuum. *Physical Review Letters*, 95(13):134801, September 2005.

[61] D. P. Pritzkau and R. H. Siemann. Experimental study of RF pulsed heating on oxygen free electronic copper. *Physical Review Special Topics - Accelerators and Beams*, 5(11):112002, November 2002.

[62] T. O. Raubenheimer. An afterburner at the ILC: The collider viewpoint. In *Advanced Accelerator Concepts*, page 86. AIP, Stony Brook, New York, 2004.

[63] T. O. Raubenheimer. Private Communications, 2008.

[64] J. B. Rosenzweig et al. Acceleration and focusing of electrons in two-dimensional nonlinear plasma wake fields. *Physical Review A*, 44(10):R6189, 1991.

[65] J. B. Rosenzweig et al. Effects of ion motion in intense beam-driven plasma wakefield accelerators. *Physical Review Letters*, 95(19):195002, October 2005.

[66] J. C. Sheppard et al. Commissioning of the SLC injector. Technical Report SLAC-PUB-4099, Stanford Linear Accelerator Center, 1986.

[67] C. B. Shroeder et al. Design of an XUV FEL driven by the laser-plasma accelerator at the LBNL LOASIS facility. In *Proceedings of FEL*, page 455. BESSY, Berlin, 2006.

[68] T. Tajima and J. M. Dawson. Laser electron accelerator. *Physical Review Letters*, 43(4):267–270, July 1979.

[69] M. C. Thompson et al. Breakdown limits on gigavolt-per-meter electron-beam-driven wakefields in dielectric structures. *Physical Review Letters*, 100(21):214801, 2008.

[70] M. Tzoufras et al. Beam loading in the nonlinear regime of plasma-based acceleration. *Physical Review Letters*, 101(14):145002, 2008.

[71] M. J. Van Der Weil. Applications of high-brightness electron beams. In *ICFA Workshop on the Physics of High Brightness Beams*, page 3. World Scientific, Los Angeles, CA, 1999.

[72] D. H. Whittum et al. Electron-hose instability in the ion-focused regime. *Physical Review Letters*, 67(8):991–994, August 1991.

[73] H. Wiedemann. *Particle Accelerator Physics I.* Springer, 1999.

[74] I. Wilson. The compact linear collider CLIC. *Physics Reports*, 403-404:365 – 378, 2004.

[75] W-M Yao et al. Review of particle physics. *Journal of Physics G: Nuclear and Particle Physics*, 33(1):1–1232, 2006.